UNIVERSITÉ DE STRASBOURG

ÉCOLE DOCTORALE ED269- Mathématiques, Sciences de l'information et l'ingénieur

ICUBE

THÈSE présentée par:

Wenwu ZHU

soutenue le : **13 AVRIL 2015**

pour obtenir le grade de : **Docteur de l'université de Strasbourg**

Discipline/ Spécialité : Traitement du signal et des images

Segmentation et recalage d'images TDM multi-phases de l'abdomen pour la planification chirurgicale

THÈSE dirigée par :

Mr. REMOND Yves	Professeur, Université de Strasbourg
Mr. SOLER Luc	Professeur, IRCAD - Université de Strasbourg

RAPPORTEURS :

Mr. MALANDAIN Grégoire	Directeur de Recherche, I3S-INRIA
Mr. PASSAT Nicolas	Professeur, Université de Reims Champagne-Ardenne

---

AUTRES MEMBRES DU JURY :

Mr. HEINRICH Christian	Professeur, Université de Strasbourg
Mr. NICOLAU Stéphane	Directeur de Recherche, IRCAD

Acknowledgement

This doctoral research program was supported by China Scholarship Council which provided all fees for my work and life in France. The PhD degree is a very important achievement in one's academic career, though it is full of challenge during the period. I have to highlight that my goal could have never been reached without the contributions of many other people. I hereafter express my appreciation to those persons involved in my PhD study and apologize in advance for those who are not mentioned involuntary.

I firstly would like to thank Prof. Jacques MARESCAUX who is the president of IRCAD and gave me the chance to investigate my research in his computer science team. I give my appreciation to the jury: Prof. Grégoire MALANDAIN, Prof. Nicolas PASSAT and Prof. Christian HEINRICH for arranging themselves to be part of the committee of my defense despite their extremely busy schedule. I also want to thank them for carefully reviewing my long thesis and giving many remarkable comments and suggestions which helped me to understand deeper and broader this research topic.

I need to express my sincere emotion to my thesis supervisors Prof. Yves REMOND and Prof. Luc SOLER who gave me the opportunity to participate in such interesting project and constantly guided me during the past three years with their enthusiasm. They always explained me the details with patience when I had questions about the research or industrial services.

I would like to express my deep gratefulness to my advisor Dr. Stephane Nicolau who is full of wisdom and a brilliant mentor for me. I cannot imagine that I would have completed my PhD thesis without his help. I would like to thank his tremendous help and guidance in the work and life. His scientific training paves the way for me to be a good researcher.

I am very grateful to Dr. Vincent AGNUS who is an expert in computer programming and image processing. He is always full of passion and never hesitated to contribute with all his ideas and solutions to help me solve my problems. I would also like to give many thanks to Dr. Alexandre HOSTETTLER who is a specialist in breathing simulation. His deep experience in breathing motion has contributed to help me better understand the registration problem.

The contribution from Dr. Jordan Bano cannot be neglected either. He always helped me at any time with a high enthusiasm whenever I asked him even if he had huge tasks to do. I would especially thank Sylvain BERNHARDT who spent much time to correct my thesis in the stressful periods and make it more fluent. I would also thank the image segmentation team who provided me clinical CT and MR images. I could have not continued my research work without their collaborations.

I would like to express my appreciation to Miss Pamela LHOTE who plays a very important role in my article writing. I also thank Julien WAECHTER and Pascal MONNIER from R&D department who gave me much help in the configuration of my computer programming environment. I also thank all members of the IT department who maintain all computers in our team and help fix any problems in time.

I am also thankful to many friends in Strasbourg, who shared their lives with me in the past three years. Particularly, my friend Xiao Xuan, who is always positive and gave many encouragements when I had huge pressure during the thesis writing.

Finally, I want to express my deepest love to my parents and families who always support my pursuit in my life and give me the power to pass through any difficulties.

March 2015

Wenwu ZHU

Content

Part I Main Thesis

Chapter 1 Introduction

1.1 Background

Imaging is a vital component for medical research and clinical application. It includes the diagnostic setting, surgical planning and post-operative evaluation. Given the significant advancement of computer techniques and devices, the development of the medical imaging field has been promoted rapidly and thus changed the information acquisition mode. The traditional x-ray imaging technique provided 2D visual information of the interior of patients by printing the images onto radiographic films which were analysed in a light box. The information of 3D shape of the organ of interest and its spatial relationship with surrounding tissues could only be obtained based on the imagination and experience of the clinical surgeons and radiologists.

The emergence of new imaging techniques, such as computed tomography (CT), magnetic resonance imaging (MRI), ultrasound (US), positron emission tomography (PET), functional MRI (fMRI), enabled the generation of a 3D volume image consisting in continuous slices, which can be viewed conveniently in the axial, coronal or sagittal plane with the use of multi-planar reformatted imaging. However, these techniques have different inherent imaging mechanisms and provide different visual information, thus bringing the requirement of integration between these images. A special terminology of this process is image registration which aims at matching different image data of interest into the same spatial coordinate space, thus providing a comprehensive context for the clinical application.

Image registration is a crucial step in many medical fields with different purposes. For instance, one can:

(I) Monitor the brain disease progress of the same patient over time (cf. FIGURE 1.1) with the use of fluid registration of serial 3D MR images (Freeborough & Fox, 1998;Fox & Freeborough, 1997). Such registration is called intro-patient mono-modal registration.

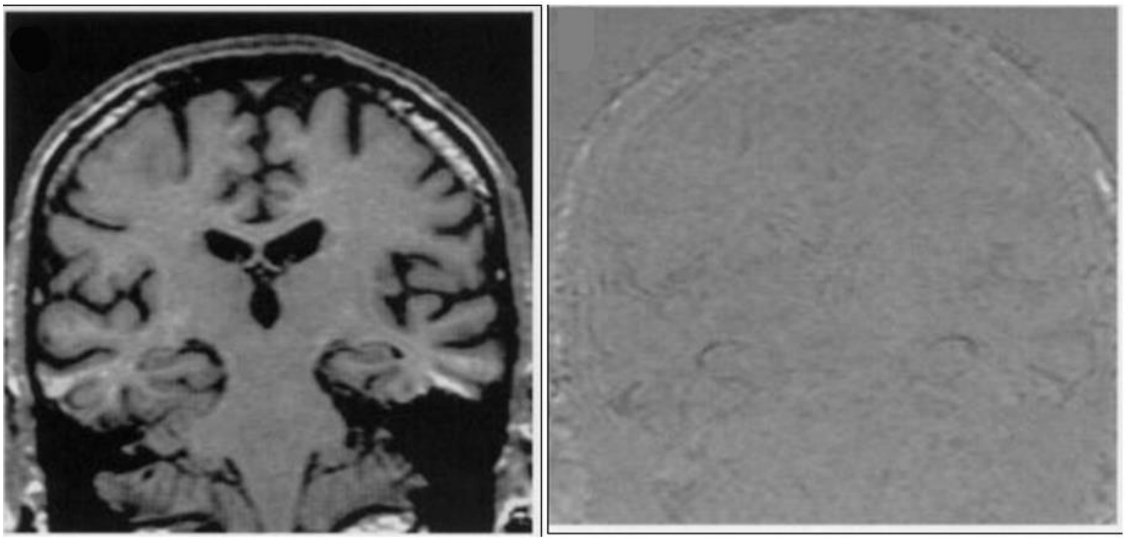

(a) (b)

FIGURE 1.1: The registration of the brain. (a) The baseline MR scan of an Alzheimer disease patient. (b) The difference after the fluidly registration between the new scan after 22 months and the baseline scan (a). These images are from the paper of Freeborough & Fox, 1998.

(II) Build a computerized human lung atlas from CT image with use of consistent landmark- and intensity-based thin-plate spline registration algorithms (B. Li et al., 2003;B. Li et al., 2012). The lung, airway tree and skeleton are segmented automatically (cf. FIGURE 1.2) using the segmentation from (S. Hu et al., 2001; Kiraly et al., 2002), then the airway branch points are extracted as the internal landmarks for establishment of the correspondence during the registration (cf. FIGURE 1.3). In this context, the registration is still mono-modal but inter-patient. A similar work is the construction of a statistical shape model of anatomical variability of brain, in which a deformable registration is adopted to establish the point correspondences between shapes from different patients (Rueckert et al., 2003; Subsol et al., 1998; Wang & Staib, 1998).

FIGURE 1.2: From left to right: Airway tree, center lines, and branch points which are extracted from the pulmonary CT image (B. Li et al., 2003).

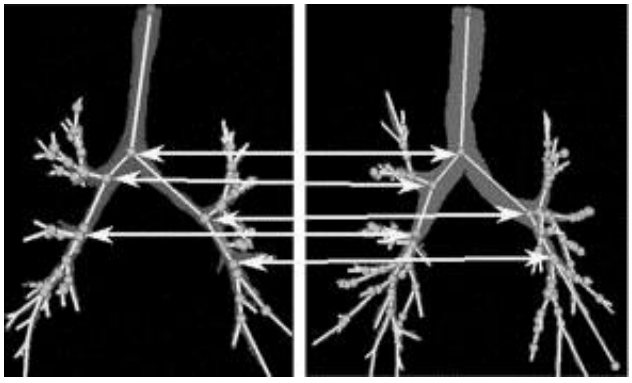

FIGURE 1.3: The matching example of branch points from airway trees of different subjects (B. Li et al., 2003).

(III) The quantification of the perfusion for the heart would be impossible without the use of registration to correct the motion due to the fact that the heart beating cannot be controlled consciously (Bidaut & Vallée, 2001). The registration is performed on the dynamic cardiac MRI after contrast media injection and each image from the dynamic sequence was spatially registered to the reference image.

One can note that most registration work focuses on one organ only. Although mono organ registration is medically relevant, there are many clinical contexts where the environment of organs is important. Particularly for abdominal regions in which there are many potential cancers, almost all registrations focus on one organ only, e.g. liver (Carrillo et al., 2000; Torsten Rohlfing et al., 2004; KM Brock et al., 2003; W.-C. C. Lee et al., 2005; Lange et al., 2005; Cash et al., 2007; Lange et al., 2009; Wein et al., 2008; Peterhans et al., 2011; Vijayan et al., 2014; Sundarakumar et al., 2015; Mauri et al., 2014), kidney (Zöllner et al., 2009; Yang et al., 2014; Nishiyama et al., 2014; Spiegel et al., 2009; Leroy et al., 2004; Kaus et al., 2007), pancreas (M. J. Murphy et al., 2000; Kandel et al., 2009; Donati et al., 2010) , whereas we know

that an accurate registration between the organs and its surrounding vessels is important for the surgical planning , for instance, hepatic and adrenal gland surgery. In the procedure of duodenopancreatectomy, the surgeon needs to assess accurately their relative positions to surrounding organs (spleen, pancreas and transverse colon) to choose the right instrument access. Another common example is the gallbladder surgery, which involves vessels around the liver, the stomach and the pancreas, which are not inside one organ only.

However, the image registration of abdominal viscera is complicated. The abdominal organs are soft tissues and can be deformed due to the gravity and other muscle contractions. The patient position is difficult to keep the same between several image acquisitions which can also lead to the position variation of organs. The position of abdominal organs is also dependent on the point or phase of the breathing motion, particularly the liver and spleen, because they are attached to the diaphragm. In addition, there are no fiducial markers can be used in this region, while such markers are usually employed for the registration of brain. There is also the discontinuous motion between the abdominal viscera region and abdo-thoracic wall which is mainly caused by the breathing motion. FIGURE 1.4 illustrates this phenomenon from multi-phase CT image, the venous phase data being superimposed onto the artery phase in axial, frontal and sagittal view respectively. Venous and artery phase CT images are two CT scans acquired on the same patient while a time gap round one minute. The patient is asked to take an inspired breath motion held to obtain a same magnitude of the organs, which particularly seldomly happened. One can see the big difference of the ribs positions in FIGURE 1.4 (b) due to the sliding motion, and the big deformation of abdominal organs. The sliding motion makes the registration problem more complicated, namely the discontinuous deformation field between the abdominal organs and abdominal-thoracic wall. The feature of deformation field with high discontinuities contradicts the general assumption of usual registration algorithms in which the entire motion field should be smooth.

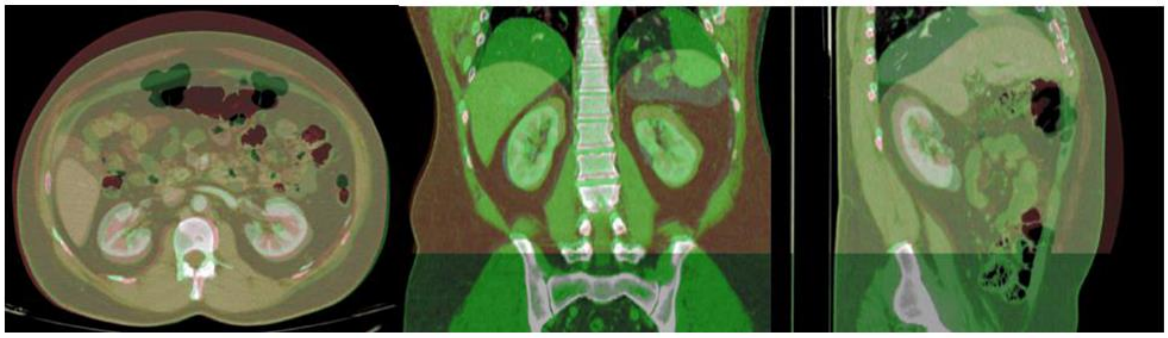

(a) (b) (c)

FIGURE 1.4: Illustration of sliding and deformation by superimposing the venous phase image onto the artery phase in axial (a), frontal (b) and sagittal view (c) respectively.

1.2 Objective

The purpose of this thesis is to propose an approach for registering the abdominal viscera despite the problem we described previously. Our approach should overcome the following constraints:

1) We aim at finding a technique which is able to register the entire abdominal viscera organs and their surrounding vessels.

2) We want to propose a registration approach, which deals with the breathing and its influence on abdominal viscera motion.

3) We currently investigate the multi-phase CT image registration, and will expand our approach to CT-MR in the future.

1.3 Outline of the thesis

This thesis is organized in 7 chapters, including the general introduction in Chapter 1 and general discussion and conclusion in Chapter 7. The content of other chapters is organized as follows:

Chapter 2 provides the clinical background. We firstly introduce the cancer in the abdominal viscera region especially related to the liver. Then the diagnosis and treatment approaches of Hepatocellular Carcinoma (HCC) are reviewed, which highlight the significance of the surgical planning and its role for the theraphetic decision. Practically, understanding the tumor po-

sition and its spatial relationship with surrounding vessels explains why the registration is critical during the surgical planning step to increase the surgical success chance.

Chapter 3 gives an overview of image registration, which is helpful for readers to understand our approach. We realize that the traditional registration method is not sufficient and robust for abdominal viscera region, since the effect of the breathing motion should be processed specifically. We thus analyse the mechanism of the breathing motion, and review the work which aims at handling the sliding motion for the registration. This review shows that no experiment has been focused on abdominal viscera but existing results related to lung registration, thus confirms our feeling: sliding motion as a priori knowledge should be provided to the registration approach. We finally propose to perform a segmentation of the abdo-thoracic wall and further exploit this information to remove the sliding motion effect on the registration of the abdominal viscera.

Chapter 4 describes the contribution of two interactive segmentation tools we developed to quickly delineate abdo-thoracic wall and thoracic viscera. There is a large number of slices in a 3D CT volume image, in general more than 200: an expert needs to spend more than 5 hours to finish the segmentation of abdo-thoracic wall slice by slice. We propose to perform a fast segmentation by delineating several selected slices in axial view (resp. sagittal view for thoracic viscera), the remaining slices being automatically segmented with the used of B-spline based interpolation technique. The segmentation accuracy and the number of selected slices (NSS) that must be interactively delineated are also evaluated and discussed. The segmentation results will be used in the following registration work. The work in this chapter has been published in the MICCAI 2012 workshop on Computational and Clinical Applications in Abdominal Imaging (Zhu et al., 2012) and is currently under review in the Journal of Computer Surgery.

Chapter 5 describes our approach to tackle the multiphase CT abdominal viscera registration. Since the main error is caused by the discontinuity of the deformation field close to boundary between abdo-thoracic wall (AW) and abdo-thoracic viscera, we choose to replace the abdo-thoracic wall from images by an homogenous value using the previous segmentation. To verify the influence of lung in abdominal viscera registration, we also use images without abdo-thoracic wall and thoracic viscera (AW&TV). A state-of-the-art non-rigid registration algorithm was designed and implemented to register the abdominal viscera generated by previous segmentation. Super Baloo (SB) algorithm was also employed to show that our approach is

not fully dependent on a specific registration algorithm. Finally, a complete evaluation of the registration accuracy, not limited to one organ only, is performed qualitatively and quantitatively, which includes the visual analysis of deformation field, the measurement of organ surface distance, and the error calculation of the vessel bifurcations.

Chapter 6 presents our first attempt to provide automatic segmentation of the AW, which was motivated by the excellent registration we obtained in the previous chapter. We firstly analyse the AW shape in axial, sagittal and frontal slices and explain why we believe the AW seems easier to delineate in frontal slices. Then, we propose a segmentation method based on a first step of prior segmentation (lungs, ribs and abdominal muscles), followed by a refinement performed using image gradient along a specific direction. Finally, experiments on patient data are performed and encouraging results are obtained. However, they also indicate that a better prior analysis and understandings of the patient anatomy is necessary to reach the accuracy expected by practitioners.

Chapter 2 Clinical Background

Nowadays, it is well known that brain registration is mandatory for clinical analysis of the brain function (Pietrzyk et al., 1996;Jenkinson et al., 2002;Jay West et al., 1997;Holden et al., 2000;Avants et al., 2011;Chen & Varshney, 2003;Klein et al., 2010), and also suited for image guided neurosurgery (Dogra & Patterh, 2014; Warfield et al., 2002; Gering et al., 2001; Grimson et al., 1996; Ferrant et al., 2002).

In the abdominal area, similar work has been performed essentially for the liver (Torsten Rohlfing et al., 2004; KM Brock et al., 2003; W.-C. C. Lee et al., 2005; Lange et al., 2005; Cash et al., 2007; Lange et al., 2009; Wein et al., 2008; Peterhans et al., 2011; Vijayan et al., 2014; Sundarakumar et al., 2015; Mauri et al., 2014), which manages to provide fusion of several modalities, each giving their specific information related to the liver context, such as tumor, artery position, hepatic vein, biliary tree and portal tree. Obviously, this work is important, but the abdominal area is not limited to the liver. There are many pathologies involving not only one organ, yet its environment as well. In literature, as far as we know, there is no registration method for abdominal viscera.

In this chapter, we propose to explain why information fusion of the entire abdominal viscera is crucial for a better diagnosis and surgical planning. Section 2.1 first presents general cancers in abdominal viscera region. Then, Section 2.2 describes diagnosis and treatment approaches which related to the described cancers in previous section. We also introduce the surgical planning role to choose an optimized therapy, and emphasize why registration of entire abdominal area can directly affect the success of the surgical planning and consequently that of the surgical outcome.

2.1 The cancer in abdominal viscera

There are many critical cancers in the abdominal viscera region which includes the liver cancer, renal tumors and pancreas tumors. We briefly describe these diseases and their corresponding treatment approach.

2.1.1 Hepatocellular Carcinoma

The liver is the largest organ in the abdominal viscera and the most complex one. It is located in the upper right-hand position of abdominal cavity, under the diaphragm and above the stomach and the right kidney (cf. FIGURE 2.1). The liver is made of soft pinkish-brown tissue and linked to the peritoneum of the abdominal cavity. The hepatic portal vein and hepatic artery supply blood to the liver where it is processed, added nutrients and sent back to the whole body by the hepatic vein. The liver also contains many other functions which are vital for almost all organs (Heimann et al., 2009)

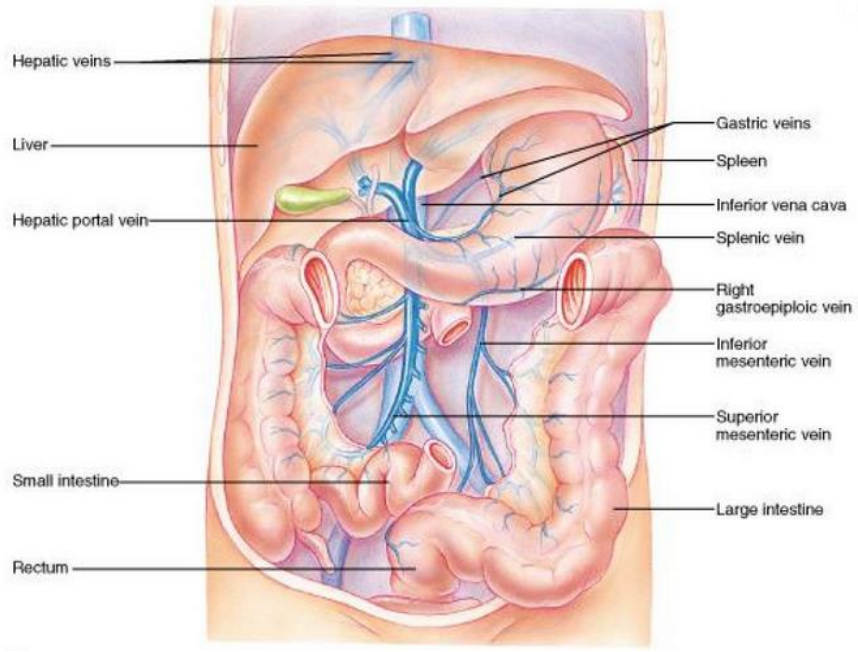

FIGURE 2.1: Illustration of liver anatomy and surrounding vessels, the figure is cited from the website of (Cummings, 2001).

HCC is a tumor of the liver and is also one of the most common malignancies all over the world (J. M. Llovet et al., 2003;M. Sherman, 2005;Bruix et al., 2004). Each year, over a million people's deaths are related to HCC. The incidence rate varies largely with the region of the world, the number is approximately 2-5 cases per 100, 000 people in developed western

countries, but more than 100 per 100, 000 people in the south-east Asia and sub-Saharan Africa regions (El-Serag & Mason, 1999;Park, 2005). A report shows that the mean survival period of the patients with HCC is 6-20 months (Di Bisceglie et al., 1988), and this situation has not improved visibly though the technique of the diagnosis and treatment therapy has obtained significant progress (Bruix et al., 2001).

2.1.2 Kidney cancer

There are two kidneys in the human body (cf. FIGURE 2.2), the left kidney is under the spleen and the right kidney is under the liver, being slightly inferior to the left one due to the big volume of the liver. Kidneys are located deep behind the peritoneum and are well protected by the ribs and muscles of the back to avoid external damages. The function of kidney is to filter water and impurities in the blood. One third of all blood pushed from the heart enters the kidneys and flows to the other organs and tissues via the renal veins system after the filtering process (Marieb & Hoehn, 2007).

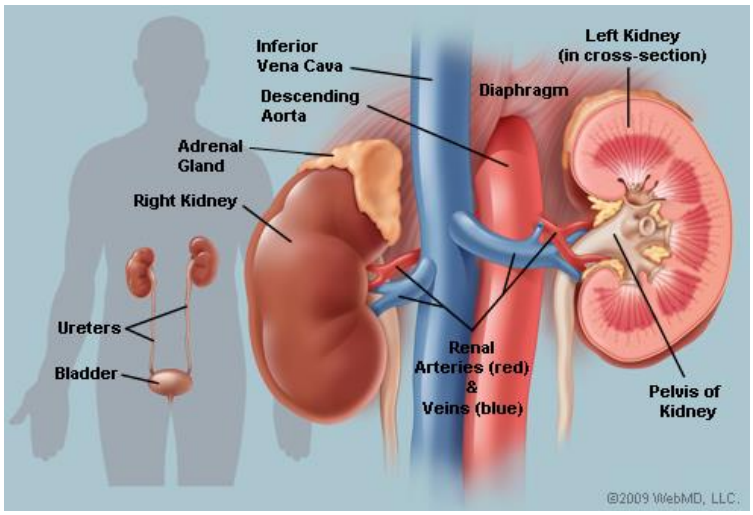

FIGURE 2.2: Illustration of the kidney anatomy cited from ("Picture of the Kidneys," 2014).

2.1.3 Pancreas cancer

The pancreas sits across the back of the abdomen, behind the stomach, and is surrounded by other tissues including the liver, intestine, duodenum, bile duct and spleen (cf. FIGURE 2.3). The two main functions of the pancreas is the exocrine which helps the digestion and the endocrine which regulates blood sugar. There are several blood vessels surrounding the pancreas: the superior mesenteric artery, the superior mesenteric vein and the portal vein. These ves-

sels supply blood to the pancreas and other abdominal organs. The pancreas cancer is not very common and occurs about 1 in 10,000 people in the UK ("REAL HUMAN PANCREAS,").

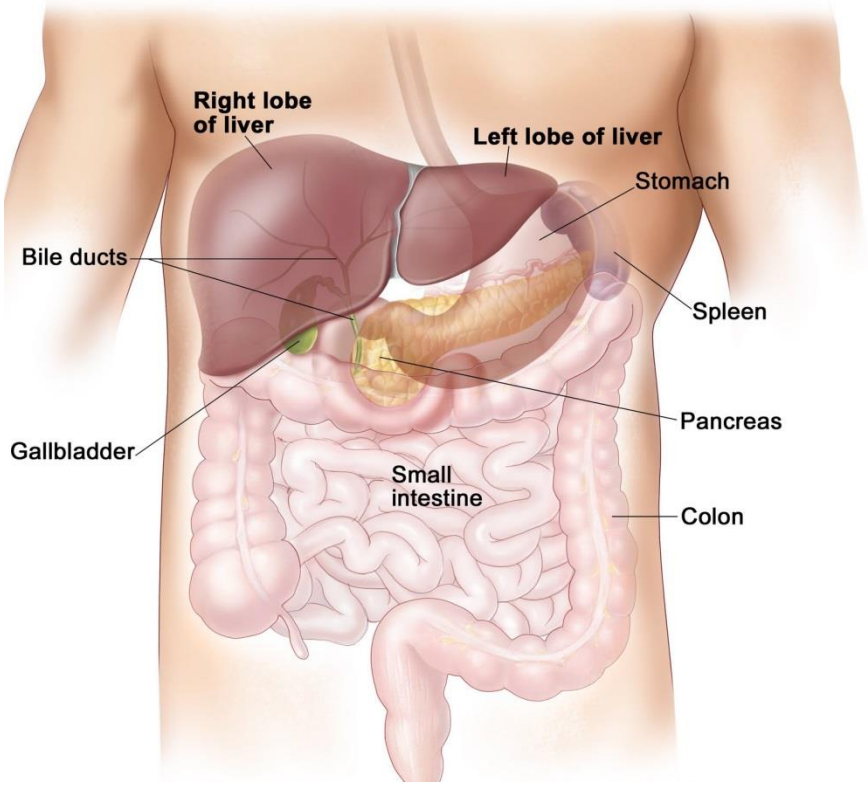

FIGURE 2.3: Illustration of the pancreas position in the abdomen ("REAL HUMAN PANCREAS,")

2.2 Diagnosis and treatment approaches

2.2.1 The diagnosis of HCC

The identification of early HCC is critical for the survival of patients (Tangkijvanich et al., 2000). The alfa-fetoprotein (AFP) and ultrasound (US) imaging are the most commonly used tools to screen HCC (Wong et al., 2000). The AFP was first used as a marker to identify HCC 40 years ago (K.-Q. Hu et al., 2004). The level of AFP for a normal adult is smaller than 10 ng/dL, and the value will be elevated to more than 400-500 ng/mL for the patient with HCC. However, research also indicates that the positive predictive value (PPV) of AFP is low, which varies from 9% to 32% (Befeler & Di Bisceglie, 2002), due to the difference of populations and regions. The accuracy of AFP for predicting HCC still needs to be improved by investigating it at a cell component level (Bialecki & Di Bisceglie, 2005). In addition, US imaging is simultaneously used to detect the small hepatic tumors smaller than 3 cm due to its low

cost and non-invasive nature. With the combination of AFP and US imaging, PPV has improved effectively and its value is up to 94% (Morris Sherman et al., 1995). Some studies also indicate that CT scans have a higher PPV than either AFP or US when either of them is used independently (Chalasani et al., 1999a). A review reports that a CT scan is used by nearly 25% of hepatologists to detect the tumor in the United States on high-risk patients (Chalasani et al., 1999b).

If an abnormal region or lesion is detected during the previous screen stage, it is required to adopt an advanced technique for the diagnosis. Triple phase CT and triple phase dynamic contrast-enhanced MRI are two of the most effective imaging techniques for achieving the diagnosis of suspected HCC lesions (D. Choi et al., 2001). The mechanism of these two techniques is similar, so here we focus on the triple phase CT. One can obtain more information on a comparison between them in the following papers (B. I. Choi, 2004;Sadek et al., 1995). The mechanism is that a specific contrast agent is injected intravenously and the CT scan is performed at various time intervals. Triple phase means the CT image is acquired with respect to the different states of the contrast agent as it flows in the blood, which is usually defined as before contrast, during arterial and venous phases. A contrast agent is used due to the fact that the target HCC derives the blood predominantly from the hepatic arteries, and this results in much more enhancement of the suspected HCC in the arterial phase 2-40 seconds after the contrast agent infusion. The surrounding normal hepatic tissues absorb 75%-80% of the blood from portal vein (Bialecki & Di Bisceglie, 2005), and thus are more visible and highlighted in the following venous phase which is 50-90 seconds after the injection of contrast agent.

James H. Oliver and his colleagues investigated the value of arterial phase CT imaging for the detection of HCC tumors by comparing results with those from unenhanced imaging and the venous phase CT (Oliver 3rd et al., 1996). After the acquisition of triple phase CT images on 81 patients with proven HCC, three blinded persons were invited to evaluate and record the number of unique or common lesions seen at each phase. The statistic result shows that 27% (89-111) of tumors can be seen on the arterial phase image and were not seen at the portal phase. And 17% tumors (45-55) are seen on the unenhanced images and cannot be inspected in the portal phase. Thus, the combination of these three phases imaging can detect much more HCC lesions than any of each imaging used independently, and finally improve the survival rates of patients.

Both CT and MRI are able to detect and identify the HCC tumor whose size is over 2 cm. The detection accuracy of both techniques is around 70% due to the anatomy similarity between HCC tumor and dysplastic nodules, focal fat and peliosis (Brancatelli et al., 2003). For suspected tumors whose size is below 2 cm or if the lesion is uncertain, another diagnosed approach (biopsy) is recommended as it is safe and effective (Borzio et al., 1994). Biopsy has been used for lesion evaluation for more than half a century and is investigated in following papers (Caturelli et al., 2004;Bravo et al., 2001;G.-T. Huang et al., 1996).

2.2.2 Treatment of HCC

Treating the HCC tumor and optimizing the patient survival is a complicated task. The considered factors include bulk, number, severity and associated comorbidities as well as the current medical condition of the patient, from which the therapy type is decided. The clinical terminology is the staging of the tumor which is critical during treatment procedure. Taking different criteria and aspects into account, there are several staging systems: Barcelona-Clinic liver Cancer (BCLC), Cancer of the Liver Italian Program, the Chinese University Prognostic Index and Japanese Integrated staging (El-Serag et al., 2008). However, to date, there is no gold standard for evaluating the stage of HCC tumor. BCLC (Josep M Llovet et al., 1998) is mainly adopted by radiologist (cf. FIGURE 2.4**)**. It defines each stage by combining the tumor feature and the corresponding liver function feature. The status of liver function is declared using a classification system called Child-Pugh classification of liver disease severity, which calculates and grades the amount of the bilirubin, albumin, prothrombon time and encephalopathy. The BCLC system also provides the treatment strategy for each stage of HCC, e.g. the stage A2 of the patient is suitable to be applied radiofrequency ablation or transplant therapy. With the guidance of the precise staging of the HCC tumor, the therapy of treatment can be chosen much more efficiently and the survival of patient can be extended. Due to the complicated clinical context, to date there is no gold standard strategy to process all different type of tumors. We give hereafter an overview of the main treatment approaches for the early stage of HCC.

BCLC STAGING SYSTEM[4]

BCLC Stage	PS	Tumor Features	Liver Function	Treatment Options
A1	0	Single <5 cm	No PH	Surgery, RFA
A2	0	Single <5 cm	PH, normal bili	Surgery, RFA, transplant
A3	0	Single <5 cm	PH, abnormal bili	RFA, transplant
A4	0	3 tumors <3 cm	Not applicable	Transplant, TACE
B	0	Large multinodular	CP A-B	TACE
C	1-2	Vascular invasion or metastases	CP A-B	sorafenib
D	3-4	Any	CP C	Supportive care

bili=total bilirubin; CP=Child-Pugh class;
PH=portal hypertension; RFA=radiofrequency ablation; TACE=transarterial chemoembolization.
Adapted with permission from O'Neil et al (2007).

FIGURE 2.4: The illustration of the BCLC staging system, the figure originated from (NEXAVAR, 2008)

- **Surgical resection**

Surgical resection means the removal of the liver part which contains the tumor. The goal of this operation is to directly remove whole tumors and this strategy usually increases the resection margin to ensure no tumor portion remains. This treatment therapy is mainly chosen for patients without cirrhosis, because the resection operation is based on the physiology feature of liver, namely, the preserved liver is capable of growing again and compensate for the removed portion. Cirrhosis makes HCC patients face two risk factors – a hepatic decompensation and a decreased ability of hepatocyte regeneration. The portion of patients without cirrhosis in western countries is roughly less than 5% in all HCC patients, and nearly 40% in Asian countries (Bolondi et al., 2001). The choice of hepatic resection also considers the tumor size, number and invasion to blood vessels. The detailed effect of these factors has been investigated by one research on the survival of 557 patients group (Vauthey et al., 2002). The statistical results show the different effect of these factors on the 5-year survival rate as follows: for tumor size <5 cm it is 43%±3%, for tumor size >5 cm it is 32%±3%; for single tumor it is 45%±3%, for the multiple tumors it is 45%±3%; without major vascular invasion it is 41%±2%, with vascular invasion it is 15%±5%. Generally, 5-year survival rate with surgical resection is around 30%-50% (Josep M Llovet et al., 2005).

Surgical resection planning requires the surgeons to estimate the liver segment boundaries according to the portal veins tree (Reitinger et al., 2006) and also consider the volume and function of remaining liver after the operation. Anatomical variations can lead surgeons to

make wrong decisions. For instance, the tumor located at segment boundary can result in too much tissue being removed (Glombitza et al., 1999).

This step is extremely difficult when the tumor is visible only on the arterial phase and its margin is totally invisible in the venous phase. Indeed, the liver segments can be delineated from the vein network only. Consequently, if the tumor position is not accurately understood in the venous image, which is the case when arterial and venous phase images are not registered, there is a risk of diagnosing its position in a wrong segment, or of missing that the tumor belongs to several segments instead of one, or of believing it belongs to several segments whereas it is located in one segment only. Such mistakes clearly influence the patient survival outcome.

Another main difficulty, when a surgeon has to plan a segmentectomy due to a tumor, is to check that the artery passing by the considered segment does not supply blood to another segment. If this is the case, removing the cancerous segment will lead to an ischemy of the neighbour segment cells, which will thus destroy the neighbour segment function. A good understanding of the 3D position of hepatic arteries (visible in arterial phase) with respect to each hepatic segment (visible in venous phase) is thus crucial to choose the appropriate surgery. In case of bad spatial interpretation, the patient's survival may be highly reduced. Both previous examples clearly demonstrate why an accurate registration of arterial and venous phase is important.

- Liver transplantation

Liver transplantation is, theoretically, the best approach for treating the HCC. It can remove the HCC and potential related tumors fully and diminish the recurrence rate dramatically. Currently, the 5-year survival rate is 70% and very low recurrence rates smaller than 15% (Josep M Llovet et al., 2005). This excellent outcome is accomplished due to the optimal candidate selection by referring to the Milan criteria (a single lesion smaller than 5 cm or up to three nodules smaller than 3 cm) (El-Serag et al., 2008). As the number of candidates for liver transplantation grows, the big issue is the shortage of donors and the long time waiting further decrease the survival rate.

- Radiofrequency ablation

Percutaneous radiofrequency ablation (RFA) is the most adopted therapy for the early HCC patients due to the fact that there are few patient candidates who are eligible for hepatic resection and liver transplantation (El-Serag & Mason, 1999). RFA is further extended to play a bridge role for patients who are waiting for a liver transplantation and also used to remove the tumors in the lung and kidney (Pavlovich et al., 2002;Gervais et al., 2005;Gillams, 2005).

The mechanism of RFA is that an electrode is placed into the center of the target tumor and a high frequency alternative current moves from the tip of the electrode to the surrounding tissue (cf. FIGURE 2.5). Usually, the needle placement is carried out under CT or US image guidance. The ions of the tissue move along the direction of the alternative current and this results in the generation of frictional heat (cf. FIGURE 2.6). The tissue cells begin to die when the temperature approaches 60 ℃ and generate the necrosis surrounding the electrode. The clinical temperature produced by the RFA often exceeds 100 ℃ and causes the death of the tumor and parenchymal cells. Ultimately, the tissue microvasculature is destroyed due to the thrombosis occurring in the hepatic arterial and portal venous branches. The extent of the tissue destroyed by the RFA depends on the impedance of the tissue and is also in proportion to the square of distance from the electrode. Thus, the generated high temperature rapidly decreases as the distance from the needle probe gradually increases. Clinically, the HCC tumor with a maximum diameter smaller than 2.5 cm can be ablated by the RFA (Curley, 2003). The multiple electrode arrays are designed and placed for tumors with a size larger than 2.5cm (Lencioni & Crocetti, 2008).

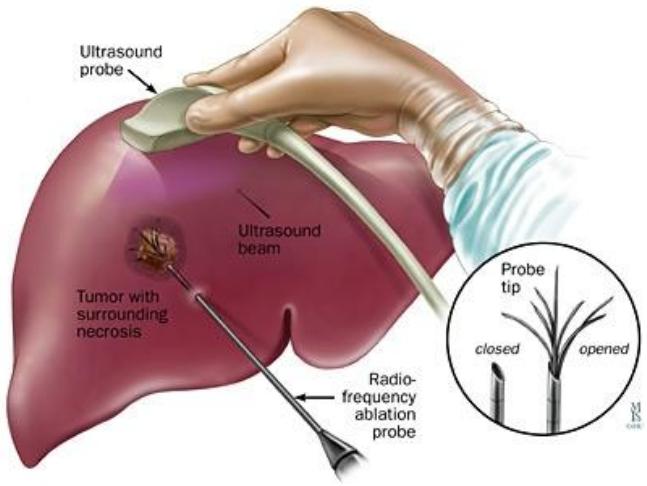

FIGURE 2.5: Illustration of the RFA originated from ("Radiofrequency Ablation (RFA)," 2010)

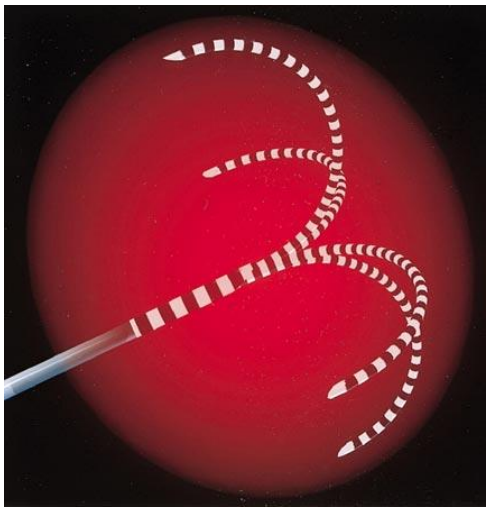

FIGURE 2.6: Illustration of the heat generation of the needle originated from ("Interventional Radiology Services,")

One of the main difficulties in RFA is the planning of the needle trajectory, which must avoid critical vessels. The poor visibility of the needle and tumor in US and CT images can lead to improper needle placement, resulting in the inadequate ablation beyond the tumor margins or thermal injury to adjacent structures (Livraghi et al., 2003). In addition, if the tumor is visible in the arterial phase only and hardly visible in the venous phase, the selection of a trajectory from arterial image using a mental registration with the venous phase image is hazardous, since it may result in a trajectory crossing a vein.

2.2.3 Treatment for other cancers

Renal cell cancer is the most common type of kidney cancer and can be treated by biological therapy, radiotherapy, cryotherapy, radio-frequency ablation and arterial embolization.The treatment options for the pancreas cancer contain surgery, chemotherapy and radiotherapy. The selection of the specific treatment option depends on many factors such as the stage of the cancer, the tumor position and the patient's health condition.

2.3 Conclusion

As we described in the previous section, there are many treatment options for different cancers in the abdomen. The key factors influencing the decision are tumor location, size, spatial relation with adjacent vessels as well as the post-operative liver function. Successful operations depend on accurate preoperative planning that gives the physicians and surgeons a de-

tailed understanding of the complex structure of abdominal organs, allowing to choose the best therapeutic option.

Multiphase CT imaging technique is used to obtain the necessary anatomy information and help diagnosis. However, the surgical planning can still be challenging because the abdominal organ shape, position and relation to adjacent structures and vessels may differ significantly between several image acquisitions. Therefore, surgeons must currently perform a mental registration between the multiphase CT data, which can be hazardous and lead to inappropriate treatment**.** Providing a software allowing to accurately register such data is thus critical to improve the surgical planning step and increase the patient survival rate.

Chapter 3 Image registration problem of the abdominal viscera

In the previous chapter, we have seen how registration can play an important role during surgical planning of abdominal viscera. However, the literature reports little work about viscera registration. The purpose of this chapter is to understand why this registration is a complex task, give an insight analysis of the existing problems and propose an approach to overcome such issues.

In this chapter, we firstly give an overview of the registration theory. We describe the feature and classification of each component and the corresponding application context. Then the section 3.2 summarizes the image registration work related to the abdominal region and highlight why breathing motion cannot be ignored to get an accurate registration on the entire viscera area. The section 3.3 deeply analyzes the causes of the inaccurate registration and concludes that the pre-segmentation of AW is a good approach to remove the sliding motion influence on the registration result. The section 3.4 gives an overview of related registration work handling the sliding motion issue.

3.1 Medical image registration framework

Image registration is a process to find a spatial coordinate mapping of the pixels (voxels in a 3D volume) from a source image to a target image (cf. FIGURE 3.1), so that the information in the source image can be aligned and fused into the target image for analysis. This matching process is usually required due to the fact that medical images are acquired at different times, views, positions and statuses on the same or different subjects. Because the registration in our research is in 3D space, we use the voxel to represent a point in the 3D CT volume image in the following chapter. Our research focuses on the CT image acquisitions at different time from the same patient.

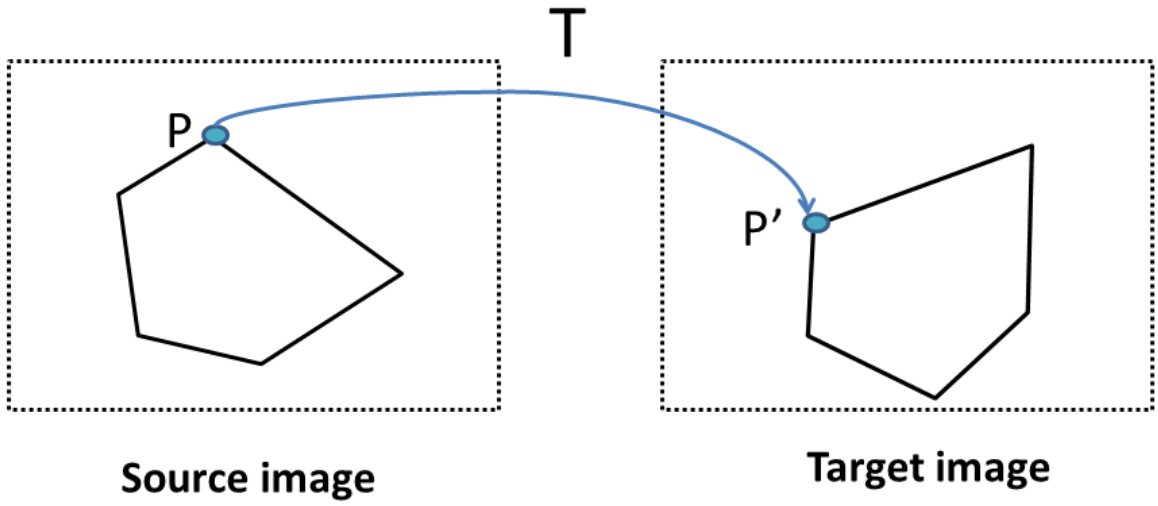

FIGURE 3.1: The image registration definition is to match the corresponding points between source and target image by using a transformation T.

The image registration framework is usually as follows and depicted in FIGURE 3.2, target and source images are input as data source, the source image will be modified and aligned to the target image (template) at the level of the voxel. The spatial relationship between the voxel in the source image and corresponding point of the target image is described as a transformation model. A similarity value of these two images is calculated, the optimization module continues to look for better parameters of the transformation model if the similarity value has not reached the expected accuracy, this procedure is iterated until the similarity value is satisfied or the maximum number of the iterations is reached. Since it is difficult to obtain the "best" transformation model immediately and complete the registration procedure, the real

implementation approach is usually an optimization process by maximizing a similarity metric. Sometimes, it can be reformatted as minimizing a cost function by adding a minus symbol before some similarity metric function which is positive, so that the best transformation matrix searching process is converted to optimize a global minimum value in the mathematical format, which is convenient for the algorithm implementation.

Briefly, the registration framework can be decomposed into mainly three components (Crum et al., 2014):

-**Similarity measure**: it defines the degree of the similarity between the target and transformed source image based on the specific image information used in the registration;

-**Transformation model**: it specifies the mapping path of how to displace the voxel in the source image to its corresponding point in the target image;

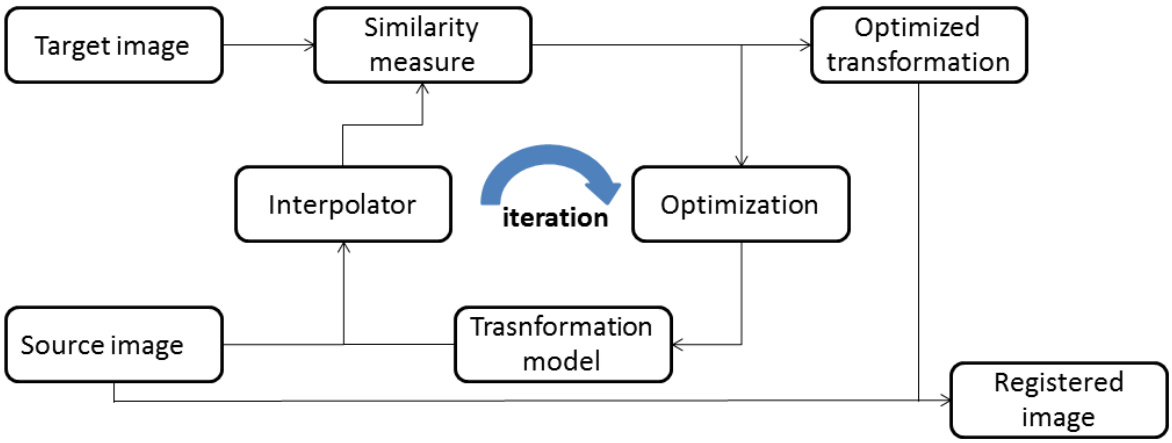

FIGURE 3.2: The framework of image registration.

-**Optimization process**: it searches the transformation parameters corresponding to the global maximum value of the similarity metric according to a specified search scheme.

We give hereafter a basic introduction of these three components, one can refer to corresponding references for deeper and broader details.

3.1.1 Similarity measure

The similarity measure is the most important factor for the success of registration, because it defines the criterion during the iterative optimization process. Its choice usually depends on

the image information used in the registration. The latter can be divided into two main categories, geometric-based and intensity-based. A geometric-based registration builds the correspondence model between target and source image with the use of geometric feature elements, the most widely used ones being landmarks and surfaces.

Geometric-based registration

The landmarks can be clustered into two categories: internal and external landmarks, which can be defined and marked based on image information of the anatomy structure of interest (Maurer Jr et al., 1997; Schad et al., 1987; Strother et al., 1994). Internal landmarks are usually identified interactively by medical experts with the use of image processing software (Yu, 2005). They are chosen and marked in both target and source images, the spatial correspondence between them being established from the consideration of surrounding anatomy features. If the image lacks sufficient information for identifying feature points, external landmarks are used. They are usually close to the patient skin and should be visible by all image modalities (Hutton & Braun, 2003; Nicolau et al., 2005; Nicolau et al., 2009; Yu, 2005). After the establishment of the landmark correspondences, the registration process is converted into searching a transformation T in order to obtain a minimal distance between landmark pairs, which can be mathematically defined as following:

$$\text{SumOfDistance} = \left(\sum_{i=1}^{N}(T(p_i) - q_i)^2\right)^{\frac{1}{2}} \qquad (3.1)$$

where (p_i, q_i) is one pair of landmark from source and target images respectively. The transformation T is a rigid or affine model due to the limitation of landmark number.

Surface-based registration is usually divided into three classical steps: the extraction of surfaces or boundaries of structures of the interest, the registration of the target and source surfaces, the extension of the surface deformation field to the whole volume (Declerck et al., 1996; Grimson et al., 1996; Herring et al., 1998; Maurer Jr et al., 1998;Crum et al., 2014). In medical images, boundaries and surfaces are usually more distinctive than landmarks and can be extracted with the use of segmentation algorithms due to the high contrast of surface, e.g. the skin. A famous surface-based registration method is called the head-and-hat algorithm proposed by Pelizzari et al. (1989). In this method, two surfaces are identified and the source surface is represented by point sets and refers to as the hat. The target mesh is represented as a list of dics and referred to as the head. The rigid transformation is searched and iterated by

minimizing the distance between points from the hat surface and the corresponding closest vertex points in the head surface. However, the distance measurement is prone to generate error due to the fact that the closest point in the target surface is not always in the direction of the head centroid.

Recently, the most popular and widely used approach proposed to perform the registration between two surfaces is called the Iterative Closest Points (ICP) algorithm and other derived methods (Arun et al., 1987; Besl & McKay, 1992). Given two point sets extracted from the target and source surfaces, the purpose of ICP is to find a rotation and translation transformation which generates the least-squared distance between the two point sets until it meets the desirable accuracy or value.

Firstly, given the initial estimation of the rigid transformation parameters, the source point sets are transformed and the closest point in the target points sets is searched by calculating the least-squared distance. Then, a new translation and rotation matrices are calculated based on the previous matched points. The new source point sets will be calculated using this new transformation and the least-squared distance is recalculated. This iterative process will continue until the local minimum value meets the convergence conditions. The limitation of this method is the large computation time and number of iteration as well as the risk of converging into a local minimum. Several improved version of this algorithm can be found in these papers (Rusinkiewicz & Levoy, 2001; Z. Zhang, 1994;Pomerleau et al., 2013; Low, 2004).

Intensity-based similarity measurement

Another branch of the similarity measurement is based on the intensity information (the voxel grey value) of the target and source images and request statistical computations. The intensity-based similarity measurements mainly include the Sum of Squared differences (SSD), Correlation Coefficient (CC) and Mutual Information (MI).

The simplest voxel similarity measurement is SSD, which assumes that the intensity value of each point should be the same after registration up to a Gaussian noise (Hajnal et al., 1995;Zhao et al., 1993;Viola & Wells III, 1997). Given the number of voxels N in the overlap domain $\Omega_{A,B}$, the SSD can be described using the following mathematical equation:

$$SSD = \frac{1}{N}\sum_{x\epsilon\Omega_{A,B}}|A(x) - B(T(x))|^2 \qquad (3.2)$$

where $A(x)$ and $B(T(x))$ are the intensity value of voxel x in the images A and B respectively, and T is the transformation.

The registration process aims at reducing the SSD value iteratively by optimizing the transformation parameters. The SSD has been widely used in the MR image registration of brain, since the brain registration is usually rigid or affine, and the MR images have similar intensities which allows comparing grey level intensity scale from one MR-scanner brand to another one (Hajnal et al., 1995; Ashburner, 2007; Holden et al., 2000). It is obvious that the SSD cannot be used for measuring the intensity value difference of inter-modality registration. We can also highlight the SSD is sensitive to a small number of voxels which have a big value difference between target and source image. For instance, if images A and B of a same patient are acquired using contrast material injected into the patient at a different time window (Hill et al., 2001).

As already mentioned, the SSD measurement has a strict assumption about the intensity information between the two input images. Another less strict metric is the Correlation Coefficient (CC) which assumes the intensity value between target and source images following linear relationship. It can be described as following:

$$CC = \frac{\sum_{x\epsilon\Omega_{A,B}}\left((A(x)-\bar{A})(B(T(x))-\bar{B})\right)}{\left\{\sum_{x\epsilon\Omega_{A,B}}(A(x)-\bar{A})^2 \sum_{x\epsilon\Omega_{A,B}}(B(T(x))-\bar{B})^2\right\}^{1/2}} \qquad (3.3)$$

where $\bar{A}$ and $\bar{B}$ are the mean intensity value in image $A|_{\Omega_{A,B}}$ and $B(T(x))|_{\Omega_{A,B}}$, respectively. CC has been used in the registration of MR and functional MR images (Lemieux & Barker, 1998; J. Kim & Fessler, 2004; Andronache et al., 2008).

Mutual information

Both of SSD and CC similarity measurements are used for the same or similar modality images which have similar grey value, but they are not suitable for multi-modality image registration, such as CT and MRI, PET&MRI, arterial and venous phases CT. In this context, the intensity characteristic of both input images is totally different and there is no obvious relationship between them. Thus, new similarity measurements have been developed, which can reflect this fact and measure the similarity in the registration. The most widely used and ro-

bust approach is MI and its derived algorithms (Mattes et al., 2001; Maes et al., 1997; Mattes et al., 2003; Holden et al., 2000).

MI is a concept from the information theory, it means how much information one variable contains about another random variable. It has been introduced into the medical image registration field by Collignon et al. (1995) and Viola and Wells III (1997) independently. Thus MI can be seen as an approach to measure how well two input images are registered and maximized when images are aligned correctly. Given the image A and B, the MI can be calculated as following:

$$I(A,B) = H(A) + H(B) - H(A,B) \qquad (3.4)$$

where H(A), H(B) represent the marginal entropy of the grey value in image A and B respectively, and H(A,B) denotes the joint entropy of A and B. The equation shows that the mutual information is not contributed by the entropy information of individual images only, but also by the joint information between them. The classical calculation method of general marginal entropy H is proposed by Shannon (2001) as:

$$H = -\sum_i p_i log(p_i) \qquad (3.5)$$

where p_i is the marginal probability distribution of the symbol i.

Entropy H will have a minimal value 0 if the occurring probability of one symbol is 1 and the probability of all other symbols is zero, and have a maximum value if all have an equal occurring probability.

In the field of image, the entropy can be calculated from the intensity value histogram in which the probabilities are the histogram entries. If an image has only one single intensity value 200, then its histogram has only one peak value at 200 and thus the probability of the voxel value 200 is 1. For all other intensity value it is 0 and the entropy of this image is $-\sum_{200} 1\log 1 = 0$. If there is some noise in this image, it means the occurring probability of other intensity values is increased, which spreads the histogram and finally increases the entropy value. In other words, the probability distribution of intensity value with a single value is related to a low entropy, whereas a broad distribution corresponds to a high entropy value.

The joint entropy H (A, B) measures the amount of information combined from two images, and can be calculated by the joint probability distribution of the two images. The mathematical description is as following:

$$H(A,B) = -\sum_{i,j} p_{i,j} log\ p_{i,j} \qquad (3.6)$$

The joint probability distribution of intensity values can be calculated from the joint histogram by dividing each entry by the total number of entries (Pluim et al., 2003). If the images A and B are acquired from different subjects with different imaging modality, thus three is no relationship between them and the joint entropy H(A, B) is approximately the sum of the entropy of images A and B. Therefore, the better the registration between the images, the smaller the joint entropy value and it is smaller than the sum of the independent marginal entropy:

$$H(A,B) \leq H(A) + H(B) \qquad (3.7)$$

In the equation of MI definition (1), we can find that MI is maximized when the joint entropy is minimized. Actually, the joint entropy is also an approach to measure the common information between two images. The problem of using joint entropy only as a similarity measurement is that when the entropy value is very low (theoretically corresponding to a good alignment of the input images), the result can be totally misregistered. For example, if an optimized transformation matches the background region of the source and target images only, thus the joint histogram of this overlapped image is sharp (the intensity value of background) and results in a low entropy value.

MI can better avoid this issue by incorporating the marginal entropy. If the registration result is only matched to the background region, the mutual information is low and when the remaining anatomy structures are also aligned it is high. This is due to the marginal entropy, which can penalize the transformation when it decreases the amount of information in the source image.

It has to be noticed that the entropy of the source image H(B) is changing during the image registration. The transformation matrix is changed at each iterative step and a new image is generated with new transformation parameters and the use of interpolation technique. H(B) and H(A,B) will then be recalculated based on this new image and result in a new value of MI at each iterative step. The registration process will be stopped while the MI value reaches the expected threshold or accuracy.

3.1.2 Transformation

The choice of transformation model is critical for the success of the image registration. Thus we give here a fundamental overview of the classical transformation categories for understanding the current progress in this field. One can learn much more in deeper details from the survey on image registration in (Hill et al., 2001;Crum et al., 2014;Holden, 2008). The transformation model mainly can be divided into rigid, affine and deformable types.

The coordinate transformation from one image to another is called rigid when only the translation and rotation are applied. The shape and dimension of the object is kept the same and only the 3D position is changing. The rigid transformation can be described by a homogeneous constant matrix equation for the 3D to 3D mapping:

$$\begin{pmatrix} x' \\ y' \\ z' \\ 1 \end{pmatrix} = \begin{pmatrix} r_{11} & r_{12} & r_{13} & t \\ r_{21} & r_{22} & r_{23} & t \\ r_{31} & r_{32} & r_{33} & t \\ 0 & 0 & 0 & 1 \end{pmatrix} \begin{pmatrix} x \\ y \\ z \\ 1 \end{pmatrix} \qquad (3.8)$$

where the point $p(x, y, z)$ and $p'(x', y', z')$ are the old and new coordinates of voxels of the image respectively, t represents translation vector and r represents a 3×3 rotation matrix which can be defined and decomposed in three Euler sub matrices:

$$r_{im} = r_{ij}^{(1)} r_{jk}^{(2)} r_{km}^{(3)},$$

$$r^{(1)} = \begin{pmatrix} 1 & 0 & 0 \\ 0 & \cos\alpha_1 & -\sin\alpha_1 \\ 0 & \sin\alpha_1 & \cos\alpha_1 \end{pmatrix},$$

$$r^{(2)} = \begin{pmatrix} \cos\alpha_2 & 0 & \sin\alpha_2 \\ 0 & 1 & 0 \\ -\sin\alpha_2 & 0 & \cos\alpha_2 \end{pmatrix},$$

$$r^{(3)} = \begin{pmatrix} \cos\alpha_3 & -\sin\alpha_3 & 0 \\ \sin\alpha_3 & \cos\alpha_3 & 0 \\ 0 & 0 & 1 \end{pmatrix},$$

where $r^{(i)}$ denotes the point rotated around the axis i by the angle α_i.

If scaling and shearing operations are linearly combined with the rotation and translation, it is called affine transformation, in which the parallelism of lines in the source image will be preserved after mapping to the new generated image, but their angle and length will not be preserved.

In contrast, a deformable transformation maps straight lines to curves and is a continuous and differentiable function which is represented as a displacement vector instead of a constant matrix:

$$P' = p + T(x, y, z) \qquad (3.9)$$

where T is a deformable transformation which can be calculated at each specific voxel coordinate.

Many deformable transformation models have been proposed. Holden (2008) divided it into two main categories: physical-based models and function representation-based models. One can learn much more from the review paper (Sotiras et al., 2013) which extends this classification and gives more emphasis on the derived algorithms which are not mentioned in this chapter.

The physical-based model is coming from the theory of continuum mechanics and generally divided into two main categories: elastic models and fluid flow models. The function representation-based model is derived from the interpolation (Meijering, 2002) and the approximation theories (Schumaker, 1981; Powell, 1981) and represents the transformation with a set of functions.

Elastic model

The theory of the elastic model is based on motions of stress strain (Holden, 2008). In the registration procedure, the model is optimized by balancing the external force (the image similarity) and the internal force (the smoothness constrain) and can be represented by the Navier-Caudy partial difference equation (PDE) (Lester & Arridge, 1999):

$$\mu\nabla^2 u(x) + (\mu + \gamma)\nabla\big(\nabla \cdot u(x)\big) + f(x) = 0 \qquad (3.10)$$

where $u(x)$ is the displacement vector at point x, μ and γ are Lam é constants, and f(x) denotes the external force per unit volume and drives the registration.

Broit (1981) firstly introduced the linear elastic model into the image registration area, with an external force f deforming the image and an internal stress μ imposing the elastic property, the registration is completed when an equilibrium is reached between two opposite forces. This PDE is solved iteratively with the use of a finite difference approach.

Bajcsy et al. (1983) improved this approach by using *a priori* affine transformation to correct the global difference. Then a multi-resolution scheme was adopted on the Broit (1981) model. The big limitation of the linear elastic model transformation described by the Navier-Caudy PDE (2) is the inability to deal with large deformation (Holden, 2008). A viscous fluid model was thus proposed by (Christensen et al., 1994;Christensen et al., 1996;Christensen et al., 1997) to tackle this issue.

The "demons" registration algorithm was proposed by Thirion (1998) based on the optical flow model (Horn & Schunck, 1981). The limitation of this model is that it lacks displacement constraints and does not preserve the topology. Some improved algorithms have been proposed to solve this issue (Pennec et al., 1999). The drawback of this family of algorithms is that they are usually combined with SSD as similarity measure which is only suitable for the mono-modal image registration.

Function representation-based transformation model

Function representation-based model derives from either the interpolation theory or the approximation theory. The principle of interpolation theory is that the remaining displacement space can be interpolated from the known values of feature points. The approximation theory considers there is an error in the sample deformation field, thus the transformation should approximate the displacement and result in a smoother deformation than its interpolation counterpart.

The most important transformation model in this category is the family of thin plate spline (TPS) which has been used for more than 15 years (Crum et al., 2014). TPS is a type of radial basis functions which have the property of interpolating a deformation field from irregular known values. The fundamental principle of TPS model is to use a control point grid to deform the shape of an object. The resulting deformation controls the shape of the whole region of interest and produces a smooth and continuous transformation. Each control point of the TPS has a global influence on the final transformation, which means that if the position of one point varies, it will result in all other points to change. Thus, it is difficult for the TPS to model a localized deformation.

B-spline-based transformation model inherits the advantage of TPS and avoids its limitation so that each control point only affects the neighbourhood points. This local support ability

makes it widely adopted for many registrations, notably for the brain (Holden et al., 2002), the heart (Frangi et al., 2002), the chest (Mattes et al., 2003;McLeish et al., 2002), the lung (Z. Wu et al., 2008;Delmon et al., 2013), the liver (Torsten Rohlfing et al., 2004), the breast (Schnabel et al., 2001;Tanner et al., 2002) etc. The property of the B-spline can be described as following.

Let Ω denote the volume size of image data in 3D:

$$\Omega = \{(x, y, z) | 0 \leqslant x < X, 0 \leqslant y < Y, 0 \leqslant z < Z\} \qquad (3.11)$$

where (x, y, z) represents the 3D coordinates of any point of the image data.

Then let Φ denote a $n_x \times n_y \times n_z$ mesh of control points $\phi_{i,j,k}$ with uniform spacing $(\delta_x, \delta_y, \delta_z)$ in each direction. Finally, for any voxel (x, y, z) of volume data, its deformation can be defined as the 3-D tensor product of 1-D cubic B-splines:

$$T_{local}(x, y, z) = \sum_{l=0}^{3} \sum_{m=0}^{3} \sum_{n=0}^{3} B_l(u) B_m(v) B_n(w) \phi_{i+l, j+m, k+n} \qquad (3.12)$$

where $i = \left|\frac{x}{\delta_x}\right| - 1$, $j = \left|\frac{y}{\delta_y}\right| - 1$, $k = \left|\frac{z}{\delta_z}\right| - 1$ and denote the cell containing the (x,y,z), $u = \frac{x}{\delta_x} - (i + 1)$,$v = \frac{y}{\delta_y} - (j + 1)$,$w = \frac{z}{\delta_z} - (k + 1)$. B_l represents the l-th basic function of the B-spline (S. Lee et al., 1996):

$$\begin{aligned} B_0(t) &= (-t^3 + 3t^2 - 3t + 1)/6, \\ B_1(t) &= (3t^3 - 6t^2 + 4)/6, \\ B_2(t) &= (-3t^3 + 3t^2 + 3t + 1)/6, \\ B_3(t) &= t^3/6 \end{aligned} \qquad (3.13)$$

From the above formula, we can conclude that B-splines are locally controlled, which makes them computationally efficient even for a large number of control points. In other words, changing coefficients of any control point$\phi_{i,j,k}$, will affect only the neighbourhood controls points $4 \times 4 \times 4$

3.1.3 Optimization

The optimization, in general, is an iterative progress of finding the "best parameters" of the transformation model, in order to maximize the similarity measurement. At each iterative step, the new similarity measurement is calculated based on the new estimated transformation (with updated parameters), then the optimization algorithm searches for a transformation in

the parameter space determined by the specific search strategy and generate a new corresponding similarity measurement. The algorithm continues until the similarity measurement reaches a threshold or the maximum number of iterations manually defined before the registration.

One issue of the optimization algorithms is that they can converge to an incorrect point like a local optimum. This is caused by the fact that there are multiple optima in the parameter space and the registration will fail if the optimization converges to the wrong optimum. Some local optima are very small, caused by a local good alignment between input images or by interpolation artifacts (Hill et al., 2001). These small optima can be removed by an image blurring operation as a pre-processing step. In addition, a multi-resolution scheme can also be adopted, in which the image registration is firstly performed at a coarse low resolution level obtained by a sampling operation, then the obtained transformation parameters will be used to initialize at a finer registration level, and so on. This can facilitate the optimization algorithm, effectively avoid dropping into local optima and improve the speed of the algorithm convergence at each resolution level.

3.2 Image registration on the abdominal viscera region

The image registration of abdominal viscera is a challenging task, due to the deformation of organs, inherent motion of the abdominal organs, as well as the sliding motion between abdominal viscera and abdominal wall. There has been much registration work presented to register organs or vessels in the abdominal viscera.

Surface-based rigid registration approaches have been proposed for the registration of livers. For instance, Herline et al., 2000 performed a surface-based registration using the iterative closest point (ICP) algorithm of Besl and McKay (1992) on liver phantoms with embedded tumors. An initial point-based marker registration is carried out and used as a "gold standard". This experiment investigated the spatial relationship between liver and tumor in phantom images, which cannot mimic the actual deformation and motion.

Surface-based non-rigid registration has also been studied. Kaus et al., 2007 proposed a model-based deformable registration with surface meshes extracted from abdo-thorax MR images (such as the lung, liver, kidney and pelvic). A point-based deformable registration is then performed on the vertices of target and source images. The obtained deformation field between mesh surfaces is then extended to the volume using an interpolation method (thin plate spline,

Wendland function deformation model). Similar work has been reported by KK Brock et al., 2005; K. K. Brock et al., 2006 who also extract surface meshes of tissue of interest and non-rigidly register them using a guided surface projection method (KK Brock et al., 2005). The volume deformation is then interpolated from the surface deformation using finite element modelling (FEM) which assigns biomechanical property to the corresponding ROIs. Such FEM technique to register the liver can also be found in (Bano et al., 2013).

Although the previous surface-based non-rigid registration approach can obtain accurate results (0.5-3 mm for different organs), they did not take the intensity value information into account, particularly they neglected the spatial relationship between the abdominal organs and the surrounding vessels, which is critical for the diagnosis and the success of some surgical interventions involving several organs. Moreover, the volumetric deformation quality depends on the mechanical property chosen for each structure, which is taken from literature and thus is not necessarily realistic. Finally, their approaches are not robust to segmentation failure or misinterpretation.

Another kind of approach to register liver images is based on intensity. Torsten Rohlfing et al., 2004 modeled the liver motion during the breathing motion using intensity-based non-rigid registration of gated MR images. The consecutive frames were registered to a common reference slice with MI similarity metric. The registration result was evaluated by visual inspection with iso-intensity contour. This method was also evaluated by Lange et al., 2005 who applied this method to register the arteries and veins of CT/MR images. However, such approaches did not take the sliding motion of abdominal viscera into account.

Carrillo et al., 2000 performed a rigid registration on interventional MR images for the treatment of liver cancer. They proposed to use a mask which contains the liver only to remove the motion effect on the registration. There are four similarity metrics tested by the authors: variance of gray scale intensity ratios, entropy, CC and MI. At least eight slices were selected from each patient for the registration result evaluation. The accuracy was measured by calculating the Euclidean distance between segmented iso-contours of the ROI. They showed that the registration with MI as similarity metric was the best and reached 3 mm, however, we believe the rigid transformation cannot accurately recover the shape deformation between different MR image acquisitions, and the evaluation approach on eight slices is limited.

W.-C. C. Lee et al., 2005 compared the registration performance of intensity-based and surface-based methods on CT and MR images of the liver. Both CT and T1 MR images were pre- and post-contrast acquisitions during a routine surveillance with a 5 mm and 10 mm slice thickness respectively. The registration accuracy was evaluated using the mean displacement of automatically selected landmarks. Their result showed that the intensity-based registration reached a 12 mm accuracy in average, which is better than surface-based registration, but still insufficient according to practitioners. The same conclusion has been obtained by Oguro et al., 2011 who compared the registration on CT/MR images between an intensity-based approach combined with a b-spline technique and a rigid registration algorithm.

The common point of above intensity-based approaches is that they rely on the assumption that the global registration transformation is smooth. However, the breathing motion not only causes the deformation of organs, but also results in the sliding motion of the lung, liver, diaphragm, kidney and spleen against the abdo-thoracic wall. This sliding motion leads to the deformation field discontinuity at the sliding interface. Thus, the mechanism and characteristic of the breathing motion in CT images are analysed in the following section, as well as its influence on the registration of thoracic and abdominal viscera.

3.3 Breathing motion

3.3.1 Introduction

Breathing is a physical movement process which refers to the gaseous exchange that occurs when the oxygen is taken in (inspiration) and carbon dioxide expelled (expiration) repeatedly. The actual gas exchange occurrs unconsciously in the lung between the alveoli and capillaries, but the rate and extent of the breathing can be controlled consciously, though it cannot be so during a long period of time.

The inspiration and expiration are accomplished by the expansion and contraction of related muscles (cf. FIGURE 3.3) and also change the volume of the lung due to its elastic property. One of the important muscles is the diaphragm, which separates the abdominal and thoracic cavities from each other. At a relaxed state, the diaphragm remained in a domed shape and intercostal muscles are also relaxed. In FIGURE 3.3, we can see during the inspiration that the diaphragm and external intercostal muscle contract and the lung expand. The contraction of diaphragm make itself flat, moves it downward, thus expanding the thoracic cavity and push-

ing the abdomen in the inferior direction. The abdominal organs (liver, spleen and kidney) are deformed and moved passively. The contraction of the external intercostal muscles also pushes the rib cage up and outwards and increase the thoracic cavity in the antero-posterior direction. After, when comes to the expiration, the diaphragm and intercostal muscles return to a released state passively due to the gravity and elasticity, and the abdominal organs also move back along the superior direction.

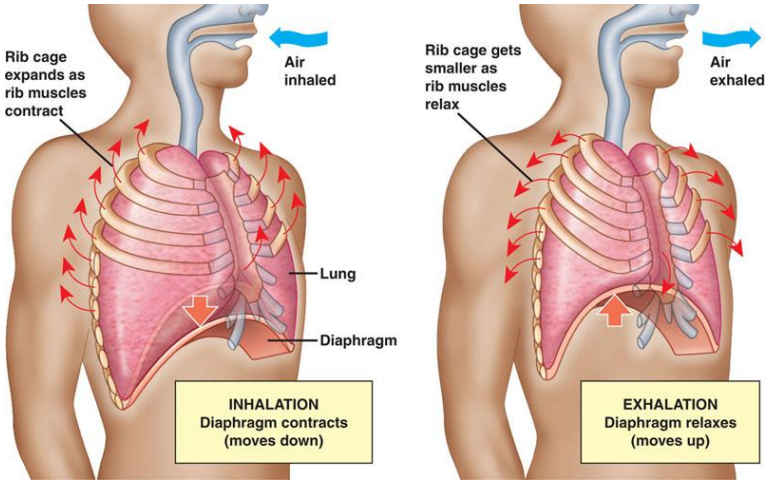

FIGURE 3.3: 1 Illustration of breathing motion. Left: the inhalation motion; Right: the exhalation (Joseph, 2010).

3.3.2 The effect of breathing motion on the abdominal viscera

The quantification of the breathing motion effect on the thorax and abdomen have been investigated by much research (Davies et al. (1994); Hugo et al., 2006; Keall et al., 2006). Since the diaphragm is the main driving factor of the breathing, the motion of the thorax and abdomen is primarily in the superior-inferior direction, particularly the organs closing the diaphragm which have a larger extent. The average moving amplitude of the diaphragm is 15 mm with maximum of 30 mm for general quiet breathing (Keall et al., 2006), though it varies largely from one subject to another. The adjacent organs and tissues show similar motion extent (cf. FIGURE 3.4), the motion of lower liver lobes moves with an average of 12 mm (Seppenwoolde et al., 2002), the spleen is 13 mm along the superior-inferior direction (Brandner et al., 2006). The motion amplitude of the kidney is in 1-25 mm, its variation usually depends on the breathing type as they move and deform more during the abdominal breathing and less during the thoracic breathing. In general, breathing is a mix of both types.

The motion of the liver attracts much research due to its physiology importance (Davies et al., 1994; Clifford et al., 2002; T. Rohlfing et al., 2004). The liver is considered as the "most moving organ" in the abdomen during the breathing cycle (Suramo et al., 1984). The predominant direction of the liver motion is the translation in the superior-inferior direction with 10-26 mm during quiet breathing (Clifford et al., 2002). Some studies indicate that the liver motion can be effectively represented by only superior-inferior movements and that its motion in other directions could be neglected (Davies et al., 1994; Korin et al., 1992). Though this approximation can simplify the registration or modelling problems for the liver, much more recent studies suggest that the motion along other axes cannot be neglected (T. Rohlfing et al., 2004; S. Shimizu et al., 1999). Rohlfing et al. tracked the variation of points within the liver and reported that the liver moves 1-12 mm in the anterio-posterior direction and 1-3 mm in the left-right direction. Relatively, the sliding motion between abdominal organs is small because all of them are attached closely with elastic property.

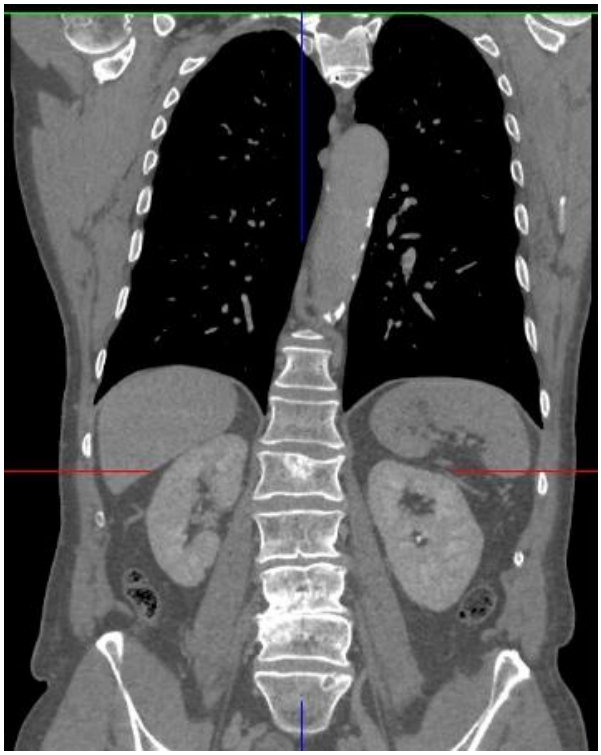

FIGURE 3.4: Illustration of abdominal organs from CT image in the frontal view

The breathing motion is complex and involves many tissues and organs whose shape and motion extent in each direction is patient-specific and irregular from one cycle to another. On the contrary, we can see that the abdo-thoracic wall is relatively static in the superior-inferior direction compared with the movement of the abdo-thoracic organs, thus resulting in a sliding

motion between them (cf. FIGURE 3.5). These structures move and slide almost independently from each other at the *pleural interface*. Thus, on one hand, these organs are moving during the breathing motion with different extents and directions; on other hand, the motion is discontinuous at the abdo-thoracic wall due to the existence of the sliding motion.

As we already mentioned (cf. Chapter 3.2), standard registration approaches consider the deformation field to be smooth and that processing the images as so will generate local errors close to the sliding regions, as it neglects the discontinuous motion (Vandemeulebroucke et al., 2012;Z. Wu et al., 2008). Such issues need to be taken into account to provide accurate and realistic registration results.

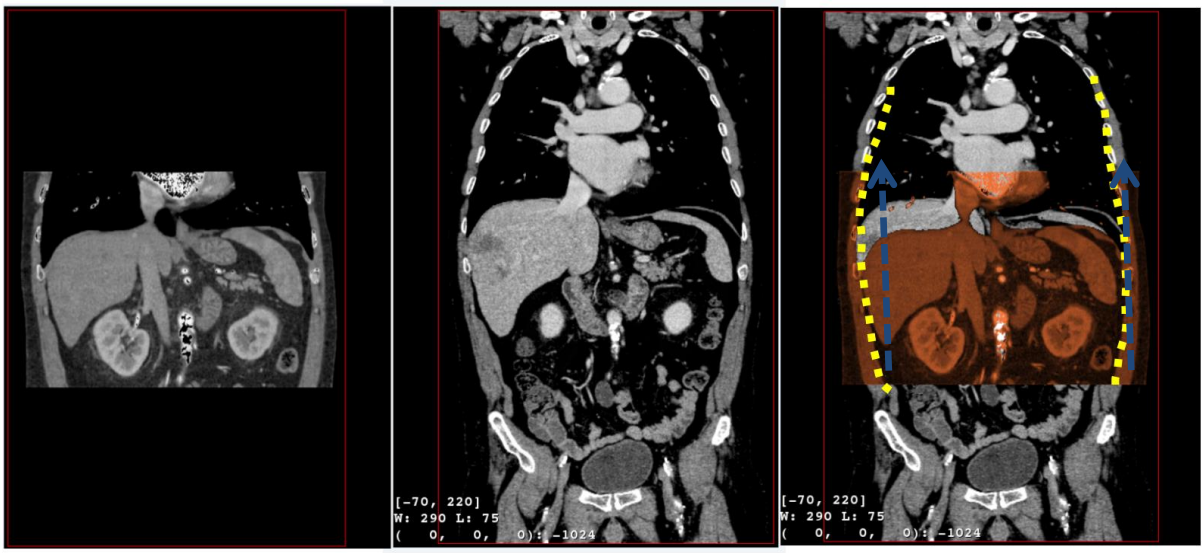

FIGURE 3.5: Illustration of the sliding motion between the abdo-thoracic wall and viscera region as well as the deformation

3.4 Existing registration methods to handle the sliding motion issue

There are many methods attempting to alleviate the sliding motion issue in the registration of thoracic CT images. They can be mainly divided into two categories. One is based on a specially designed regularization scheme, the other one relies on segmenting the images into moving and less moving regions.

CATEGORY 1

An adaptive filter has been proposed to regularize the sliding effect on the deformation field of 4D CT image registration (Wolthaus et al., 2008). This filter processes the regions separately based on the intensity information and works well for the lung and the region above the

diaphragm, although there occurs a blurring on the registration result in the region close the diaphragm and upper-abdomen. This phenomenon can be attributed to the similarity of the intensity value between the upper-abdomen and the abdo-thoracic wall.

Ruan et al. proposed a class of discontinuity preserving regularization and integrated it into the optimization step of the registration (Ruan et al., 2008). This regularization can generate a smooth deformation field in the inside of the organs (lung, heart, and exterior of rib-cage) and preserves the discontinuity on the organ boundaries based on *a priori* knowledge. But it also preserves some undesirable flow singularities which contradict the natural motion of the organs. Improved flow-driven regularization has been proposed later to preserve the large local shear discontinuous and to penalize other types of discontinuities (Ruan et al., 2009). Their approach is motivated by the Helmholtz-Hodge decomposition theory (Abraham et al., 1988) which decomposes the motion field into a solenoidal component, an irrotational component and a harmonic part. Thus, the proposed scheme applies homogenous regularization on the divergence component, penalizes the local volume change caused by the irrotational component to avoid local vacuum or mass collisions and uses a robust regularization energy function on the curl field to remove the small solenoidal component value while preserving the large shear motion on the singular set (Ruan et al., 2009). Though this approach is promising, the authors only evaluate the approach on two coronal CT slices, a more thorough evaluation on the clinical image data is required.

A. Schmidt-Richberg et. al. present a direction-dependent regularization, which allows to incorporate a priori anatomical knowledge about the location of the sliding motion (A. Schmidt-Richberg et al., 2009; Alexander Schmidt-Richberg et al., 2012a; Alexander Schmidt-Richberg et al., 2012b). The approach decomposes the motion field into normal and tangential directions independently based on the boundary of the sliding organ (cf. FIGURE 3.6). The normal-directed regularization can smooth the motion field across the organ boundary and thus prevents the gaps and foldings. The tangential-directed regularization allows the discontinuity between the movement of the organs and background in the tangential direction.

Thus, the prerequisite accurate segmentation of the sliding organ on the reference image is performed, the segmented edge could be used as a priori knowledge about the sliding location. Furthermore, they propose an automatic method to detect the boundary of the sliding motion with the use of an edge detector. Their evaluation results on 23 thoracic CT images show the accuracy is improved on the lung registration. However, their approach is also based

on the edge detector and is not suitable for detecting the sliding motion between the liver and the abdominal wall due to their vague border (Alexander Schmidt-Richberg et al., 2012b).

A similar locally adaptive regularization based on anisotropic diffusion smoothing is proposed by D. Pace for the deformable registration of sliding organs (D. Pace et al., 2013; D. F. Pace et al., 2011; D. F. Pace et al., 2012). Two diffusion tensors are adopted to enforce the smoothness of the motion field within the organ and to allow the discontinuity at the expected surface. It also performs a segmentation of the organs of interest (e.g. the lung and the liver) on the target image in order to define the sliding boundary surface.

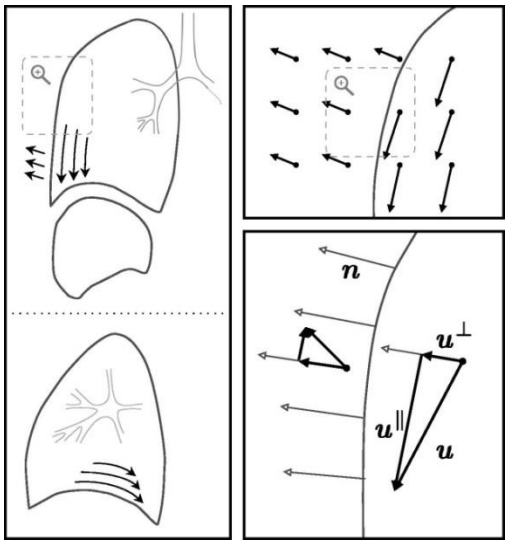

FIGURE 3.6: Illustration of the decomposition of motion field. (1) On the left, the motion of lung/liver and the surrounding tissue is depicted in the frontal and sagittal views. At the organ borders, this motion is not smooth with respect to the diffusion regularization. (2)The motion field is divided into $u^{\perp}$ and $u^{||}$, only the field in the normal direction is smoothed (right). (Alexander Schmidt-Richberg et al., 2012b)

Their registration was performed on mono-modal CT images and the evaluation using target registration error (TRE) indicates the significant improvement on the lung registration, but only a slight improvement on the liver. Since the registration focuses on the lung and liver, the performance of the approach on the entire abdominal viscera cannot be seen.

CATEGORY 2

An alternative strategy is to segment the original images into two regions based on the spatial *a priori* knowledge about the sliding surface. Z. Wu et al. (2008) evaluated the B-spline and

Demons registration algorithm on the lung of 4D CT by segmenting the thorax into moving (lungs, mediastinum) and less moving (the rest) regions which derived from the approach of (Rietzel & Chen, 2006). The two subregions are registered separately and then each single deformation field is integrated into one scene. A boundary-matching criterion is introduced to eliminate gaps and overlaps between the composed deformation fields. It is visible that the accuracy of the subregion segmentation plays an important role for the registration result. The inconsistency of the boundary between the source and target images may result in the erroneness and artifacts (Z. Wu et al., 2008).

Similarly, Y. Xie et al. (2011) also adopted a manual segmentation of the thoracic and abdominal cavities in order to register only the liver. Tissue feature points were automatically extracted inside the lung and liver for the registration (Yaoqin Xie et al., 2009). Then, they performed a TPS registration with combination of feature points on the lung and liver respectively. In their approach, the effect of the left-right (LR) and anterio-posterior (AP) motions of abdominal organs were not taken into account. The registration accuracy on the liver organ was between 2.1 and 2.8 mm by computing the contour errors. We think this accuracy is not sufficient and may be due to the choice of neglecting LR and AP motions which can be above 5 mm according to our own medical data.

Vandemeulebroucke et al. (2012) focused on the extraction of a motion mask for the registration of thoracic CT images. This motion mask not only contains the lung, but also encompasses the diaphragm and the mediastinum, instead of the segmentation of one organ only (Kabus et al., 2009; McClelland et al., 2011;Von Siebenthal et al., 2007). The registration is performed by using the free form B-Spline transformation, their results indicate that the accuracy of the registration using the motion mask is improved compared to the registration using the lung mask. The approach of motion mask extraction is also used by (Delmon et al., 2013) on the registration of thorax CT image (cf.

FIGURE 3.7). They proposed a mapping function which consists of three B-spline transformations to handle the sliding motion. The first B-spline represents the normal component of whole deformation field and enforces the continuity across the sliding interface. The other two B-spline transformations are constrained on the separated regions independently and represent the motion in a plane orthogonal to the normal N. The limitation of this approach is its ability of handling the curved interface at which the calculation of the normal direction is difficult.

Most of the previous approaches have been designed for dealing with the sliding motion on the registration of thoracic CT images. However, little research has been found for handling the sliding motion effect on the registration of abdominal viscera.

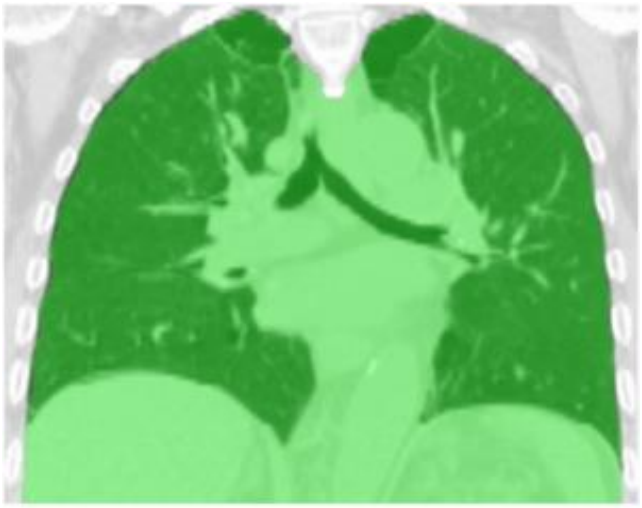

FIGURE 3.7: The motion mask (green) is superimposed on the CT image

3.5 Conclusion

In this chapter, we have given a review of the image registration framework which includes several critical components. The registration problem in the abdominal viscera region caused by the breathing motion has also been introduced. There are two kinds of approaches to handle the sliding motion effect on the registration of thoracic CT images. One is to add constraint in the regularization item by integrating the specific organ boundary information derived from organ segmentation. The other one is to divide the image into moving and less moving regions at the sliding interface (thoracic wall) and perform the registration on each image independently. However, there are also big sliding motions in the abdominal viscera region, particularly between the abdominal wall and abdominal viscera (cf. Section 3.3), which is not processed specifically by traditional registration approaches. Furthermore, the sliding motion between abdominal organs is relatively small due to their elastic properties.

Therefore, we believe an *a priori* knowledge of abdominal wall position is the most relevant approach to obtain an accurate and realistic registration. Two fast interactive segmentation tools based on *this a priori* knowledge have been designed and implemented are presented in

the Chapter 4. With the use of this segmentation result, the registration will be performed on the new images without the abdo-thoracic wall.

.

Chapter 4 Fast segmentation of the abdo-thoracic wall and diaphragm

We have seen in the previous chapter that a standard registration which neglects the sliding motion is not accurate enough. Spatial priori knowledge has thus been adopted to deal with the sliding motion phenomenon, with some success in thoracic regions where the sliding interface is easier to recognize due to the gas into lungs. We believe the equivalent spatial priori is necessary to ensure an accurate registration of the entire abdominal viscera in CT images. In particular, since the liver and spleen are located directly beneath the diaphragm which also slides during the breathing motion, it is meaningful to induce the spatial knowledge of diaphragm with the abdominal wall in the registration of abdominal viscera.

However, the segmentation of the abdominal wall in a CT image is a challenge because of its complex shape and its connection to internal abdominal organs with similar intensity value, thus hindering the use of the deformable segmentation methods. The diaphragm is also difficult to delineate close to the heart since its grey level value can be close to the liver one.

In this chapter, we present two semi-automatic tools to perform a fast segmentation of a patient abdominal wall and diaphragm based on the low curvature along the cranio-caudal direction (resp. left-right), which can provide *a priori* knowledge for the registration. We firstly present the existing work in the field of segmentation of the AW, whose accuracy is not good enough or is usually dedicated to only a specific organ instead of a plurality of organs contained in an anatomical envelop. Secondly, we analyse the challenge of AW segmentation, showing that gradient based approaches can hardly solve this issue, even if mechanical constraints are added. We then highlight that AW and diaphragm are smooth surfaces, which lead us to propose an interactive segmentation method using interpolation between a selection of several segmented slices only. Finally, we provide experiments with patient data showing that an accurate delineation and surface model of the AW and diaphragm can be provided in less than 15 minutes.

4.1 Related work on abdominal wall segmentation

As segmentation of thoracic wall is easy, we mainly review the work related to the abdominal wall segmentation. As far as we know, there has been a few works on the abdominal viscera envelop segmentation. We firstly introduce automatic methods and then semi-automatic ones.

4.1.1 Automatic approaches

A. Shimizu et al. (2007) intended to simultaneously delineate multiple abdominal organs on non-contrasted CT images. The abdominal cavity was roughly extracted using an active cylinder model (Okumura et al., 1998), but the extraction result was not reported and focused on organs only.

Ding et al. (2009) proposed to use a Gaussian mixture model (GMM) to build the intensity value distribution of the abdominal wall. The voxels between skin and bone are identified and used as a sample to estimate the intensity value distribution of the entire abdominal wall (cf. FIGURE 4.1). Then a 3D flipping-free deformable model is adopted to expand and register iteratively to the inner boundary of the abdominal wall (cf. FIGURE 4.2). However, there are many cases where the intensity value of the inner abdominal organs is similar to that of the wall muscles, and the region between rib and skin is relatively small compared with the entire abdominal wall, the estimation is thus not sufficiently accurate. We can also note that the segmentation result includes the spine which contradicts the purpose of the segmentation.

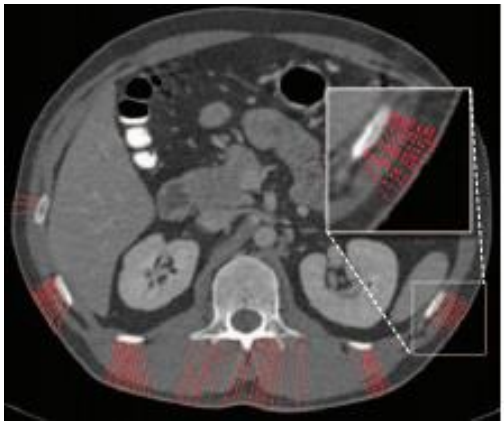

FIGURE 4.1: The extraction of the feature points (red) in the abdominal wall for building the GMM (Ding et al. (2009).

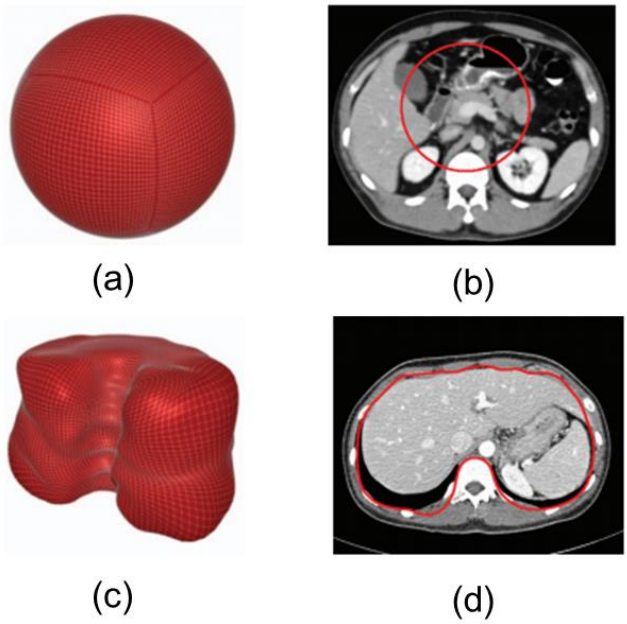

FIGURE 4.2: The process of the quadrilateral mesh expansion. The initial mesh (a) and its 2D view (b) in one axial slice. The expanded 3D surface mesh (c) and its corresponding 2D axial view (d), (Ding et al. (2009).

Deformable segmentation methods, like snake (Kass et al., 1988) or level set (Sethian, 1999;Fedkiw, 2003), are widely used in medical image segmentation (Vese & Chan, 2002;Lie et al., 2006;Paragios & Deriche, 2000;C. Li et al., 2011;Brox & Weickert, 2004), but seem not adapted for the segmentation of abdominal wall. Indeed, the snake algorithm iteratively updates the contours based on the edge information and usually converges to the skin in this context. Vandemeulebroucke et al. (2012) proposed to obtain the lung mask with use of the level set algorithm. An initial ellipsoid is used to initialize the level set function, then the propagation is conducted to the edge of the lung (cf. FIGURE 4.3). The authors also intend to obtain the edge of the upper abdominal wall. However, although their results show that the lung can be obtained due to its distinctive intensity value with surrounding tissue, they did not accurately obtain the abdominal wall (the level set algorithm converged at the skin,marked by red circle in FIGURE 4.3).

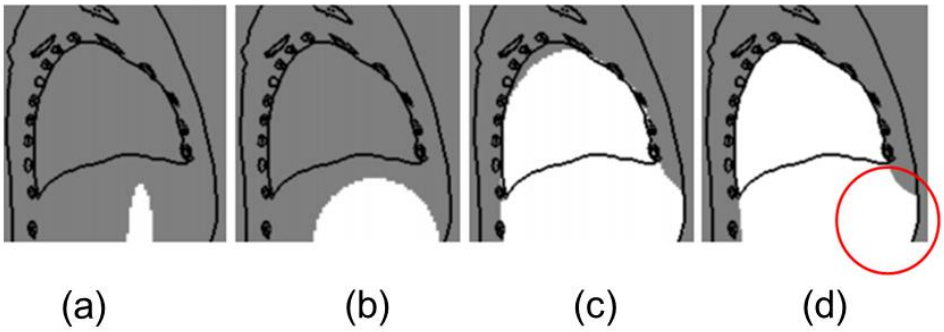

FIGURE 4.3: Illustration of the propagation steps of the level set algorithm to obtain the lung mask in the sagittal plane. The current mask is white and the edges of the extracted features are black. We show (a) the initial ellipsoid, (b) the contour reaching the detection point at the skin, (c) the propagating contour, (d) the final obtained motion mask. (Vandemeulebroucke et al., 2012).

Xu et al. (2013) proposed a texture analysis-based on Gabor filters combined with the level set to extract the anterior abdominal wall (cf. FIGURE 4.4). Obviously, such segmentation is relatively easier since the anterior abdominal wall is connected to the skin, which has distinctive intensity value. The segmentation of the posterior abdominal wall is more difficult since it is attached to many tissues with variable intensity value. W. Huang et al. (2014) proposed to adopt a *priori* shape model and context of the bone localization for the segmentation of abdominal wall. Although they show some interesting qualitative results, they do not quantitatively evaluate the segmentation result on the entire abdominal wall and it clearly appears that their algorithm does not deal efficiently with the region close to the spine and the psoas muscles.

For the diaphragm segmentation, which corresponds to the delimitation between the thoracic viscera (lungs & heart) and the abdominal viscera, no work has been found mostly because the lung segmentation is considered as a trivial step. Practically, this is often true but the thoracic viscera also contain the heart and the frontier between the heart and the abdominal viscera is much more difficult to extract automatically. Moreover, in case of atelectasis the lungs cannot be extracted using a simple threshold.

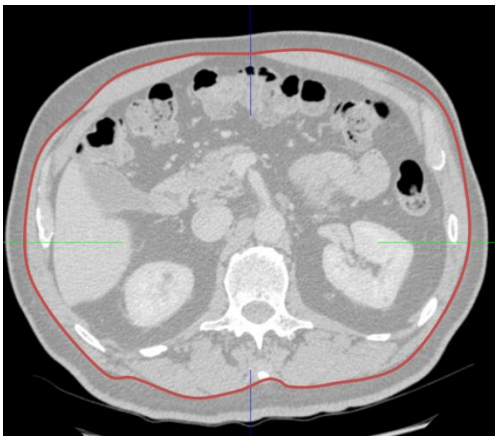

FIGURE 4.4. Illustration of the anterior abdominal wall. The manually drawn red curve represents the border of anterior abdominal wall.

4.1.2 Semi-automatic approaches

Semi-automatic algorithms or tools for specific organ segmentation usually are based on a light *a priori* information. For instance, they can consists of manually clicking seeds inside and outside the organ of interest to initialize watershed, active snakes (Williams and Shah (1992);Yushkevich et al. (2006)) or region growing algorithms (Adams and Bischof (1994)). The final boundaries usually converge close to high gradient areas and are computed through an optimization of a contour that minimizes several criteria (elastic and intensity-based). Since the boundaries of the abdominal wall are in contact with almost all abdominal organs (liver, spleen, stomach, bowel, colon) and since it contains highly different structures (bones, muscles, fat, cartilage), this kind of approach are not adapted. The gradient value which separates the abdominal to the inside viscera is varying from zero (typically the liver or the stomach, which can have identical grey values in a CT image) to several hundreds.

4.1.3 Anatomy of the thoracic and abdominal wall

In anatomy, the abdo-thoracic wall represents the tissues wrapping the abdominal and thoracic cavity (cf. FIGURE 4.5 (a)).

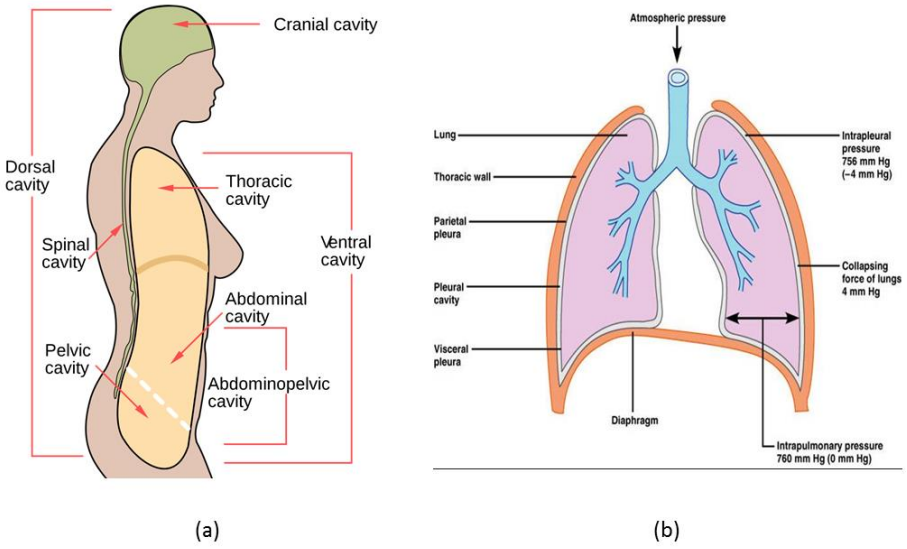

FIGURE 4.5: Illustration anatomy structures. (a)The body cavity; (b) Anatomy shape and position of the thoracic wall and diaphragm. Two figures originated from WIKI, and "Respiratory System," respectively.

The thoracic wall is the boundary of thoracic cavity (Axila, 2006) and consists of skin, muscle, and fascia (cf. cf. FIGURE 4.5(b)), the diaphragm is beneath the lung, their contours of them in frontal view of CT image are shown in FIGURE 4.6 (marked by yellow and blue curves respectively).

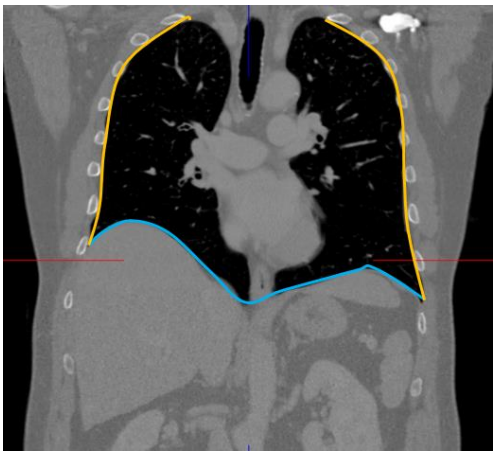

FIGURE 4.6: Illustration of the contour of the thoracic wall and diaphragm in the frontal view of a CT image (yellow and blue curves respectively).

The abdominal wall represents the boundary of the abdominal cavity and consists of the skin, subcutaneous tissue, fascia, muscles and peritoneum (Marieb & Hoehn, 2007). The subcutaneous tissue mainly refers to the fat tissue. The muscles include the external oblique muscle, the internal oblique muscle, the rectus abdominis and so on. Much more details of the ana-

tomic knowledge can be found in Wingerd, 2013. The FIGURE 4.7 (a) illustrates its anatomy structure in the cross section of a human being. The contour of the abdominal wall in a CT image is also shown in the FIGURE 4.7 (b). We can also see the abdominal wall connects to many abdominal organs, especially the liver, spleen, bowel, colon and ribs, also located inside the abdominal wall (cf. FIGURE 4.8).

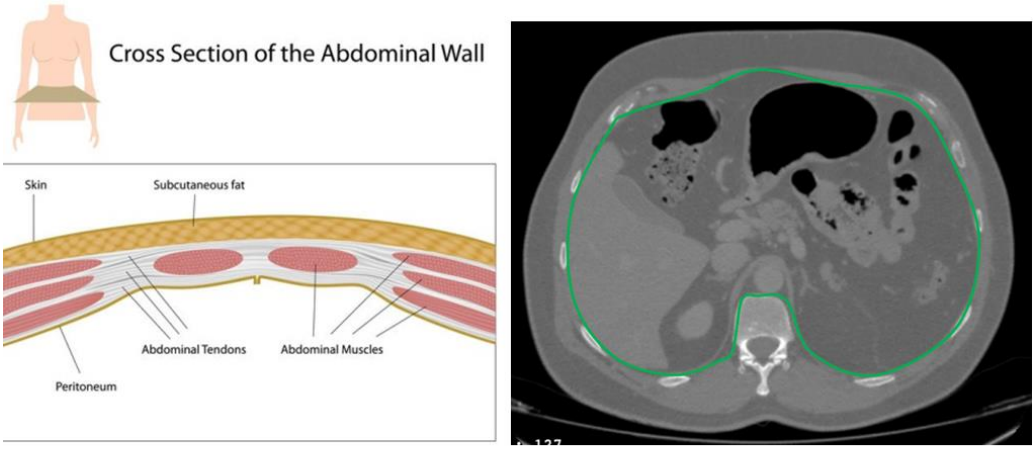

FIGURE 4.7: Illustration of the abdominal wall. (a) Anatomy structure of abdominal wall in the cross section of a human being ("Cross-section-abdominal-wall-image,"); (b) The contour of the abdominal wall in the axial view of a CT image, which is represented by the green curve.

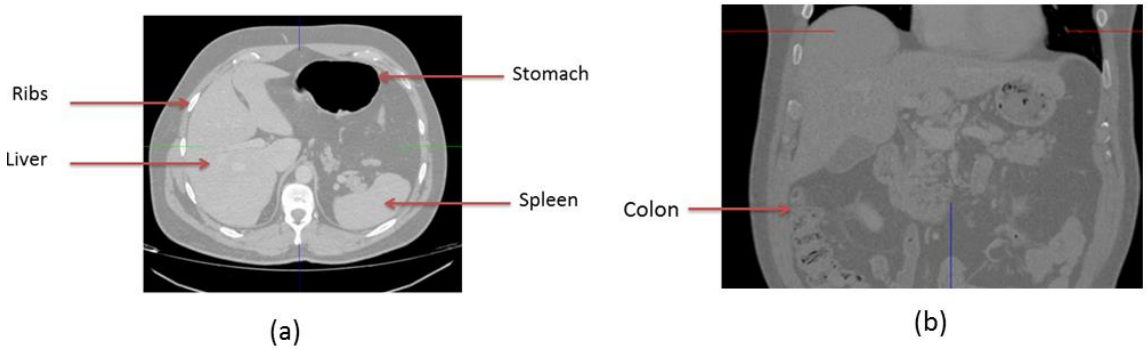

FIGURE 4.8: Illustration of the spatial relation between the abdominal wall and the abdominal organs. (a) The axial view shows the connection between the abdominal wall and the liver, spleen and stomach; (b) The frontal view shows the connection between the abdominal wall and the colon.

4.1.4 Description of the problem

The segmentation of the abdo-thoracic wall is challenging since the abdominal wall is connected to organs or tissues which have similar intensity values (marked by red rectangle in FIGURE 4.9). Also the anterior layer edge is very thin between the muscle and the fatty layer (marked by yellow rectangular in FIGURE 4.9). Here, we highlight that the segmentation of the thoracic wall is easy due to the distinctive boundary between the lung and the thoracic wall (cf. FIGURE 4.6). Thus, the difficult point is that there is no continuous strong boundary between the abdominal wall and the abdominal viscera.

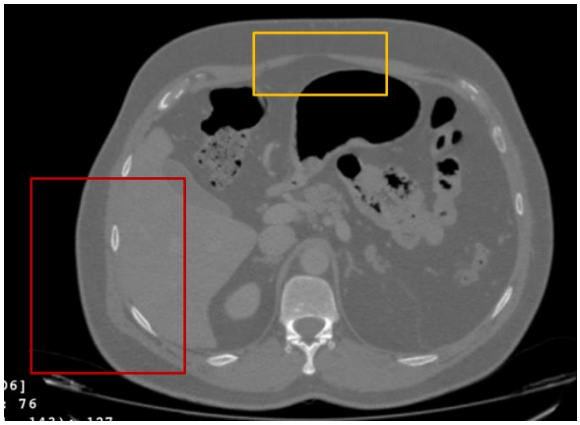

FIGURE 4.9: Ilustration of the abdominal wall in the axial view of a CT image. The region marked by the red rectangle shows that the intensity value of the liver is similar to that of the muscle of the abdo-thoracic wall. The yellow rectangle highlights the thin muscle layer in the anterior area of abdominal wall.

As described in the previous subsection, existing approaches have a limited capability to handle the edge between the abdominal wall and the viscera region due to the varying shape and vague boundary. However, one can also notice that the abdo-thoracic wall and diaphragm have a somewhat smooth curvature, even in the anterior area close to the spine. This suggests that an interactive segmentation sampled on several slices only, followed by an interpolation technique, should provide accurate segmentation results.

4.2 Fast segmentation tool of the abdo-thoracic wall

There are already several *interactive tools* which allow interpolating a shape from points, lines or curves manually drawn on a 3D medical image. In such software, the user usually draws several curves in several slices (successive or not), and an algorithm computes the best surface that passes through all curves (IQQA®-Liver, 2009; Myrian®, 2006;Wimmer et al.,

2007). The surface is usually parameterized by a NURBS (Rogers (2000)) or 3D B-splines (Rueckert et al. (1999)) and can be closed or not, enabling typical organ surface drawing or open surface. The created surface can be further locally updated or refined using intensity-based methods or a statistical model. If no further improvement is planned, this means that the control points/lines/curves only define the shape of the final segmentation. Although organ surface usually corresponds to an individual organ, manual delineation of open surface can be used to separate two organs that were segmented together with an automatic tool.

In this section, we describe our method which adopts some good aspects from the work of (Schenk et al., 2000;Wimmer et al., 2007). Schenk et al. (2000) manually segmented the liver in some slices based on the user-steered live wire algorithm (Mortensen et al., 1992;Udupa et al., 1992) and the contours in the remaining slices are interpolated with the shape-based interpolation (Raya & Udupa, 1990). The main difference between our work and theirs is not linked to the interpolation techniques but to the human machine interface and the update strategy of the segmentation result, which can be checked in real-time in our case.

4.2.1 Description

Given an abdominal 3D image, the strategy of our segmentation tool is as follows (cf. FIGURE 4.10).

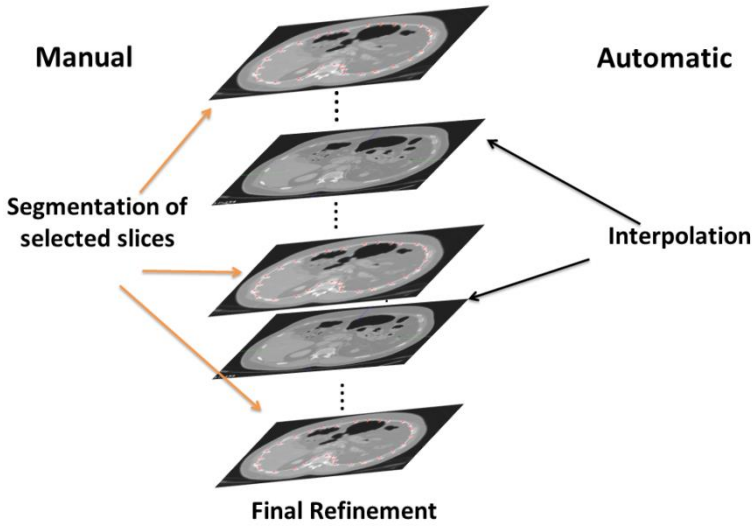

FIGURE 4.10: Illustration of the mechanism for the fast segmentation of abdo-thoracic wall.

The user selects some axial slices in which he interactively delineates the peritoneum using control points. A 2D cubic interpolation spline is adopted to fit the curve of the contour of the abdominal viscera through linking the control points. Then, the remaining slices are automati-

cally segmented in real-time using a 3D B-spline based interpolation technique. Finally, the user refines the segmentation result by checking these interpolated delineations and adding one or more control slice where he reckons that the interpolation is not sufficiently accurate. The detailed process is described hereafter.

Step 1: the user selects the first axial slice. Usually, this slice is approximately in the middle of the image. *The choice of this first slice* can be quite important and is discussed later in the next section. Then, the user adds control points sequentially along the boundary of the considered region (cf. Fig.4.16), here the abdominal viscera. Users can insert, move or delete control points. The generated B-spline curve parameterized by control points is updated in real-time, which provides immediate feedback of the curve location. Thus the place of control points can be adjusted in order to improve the created curve accuracy.

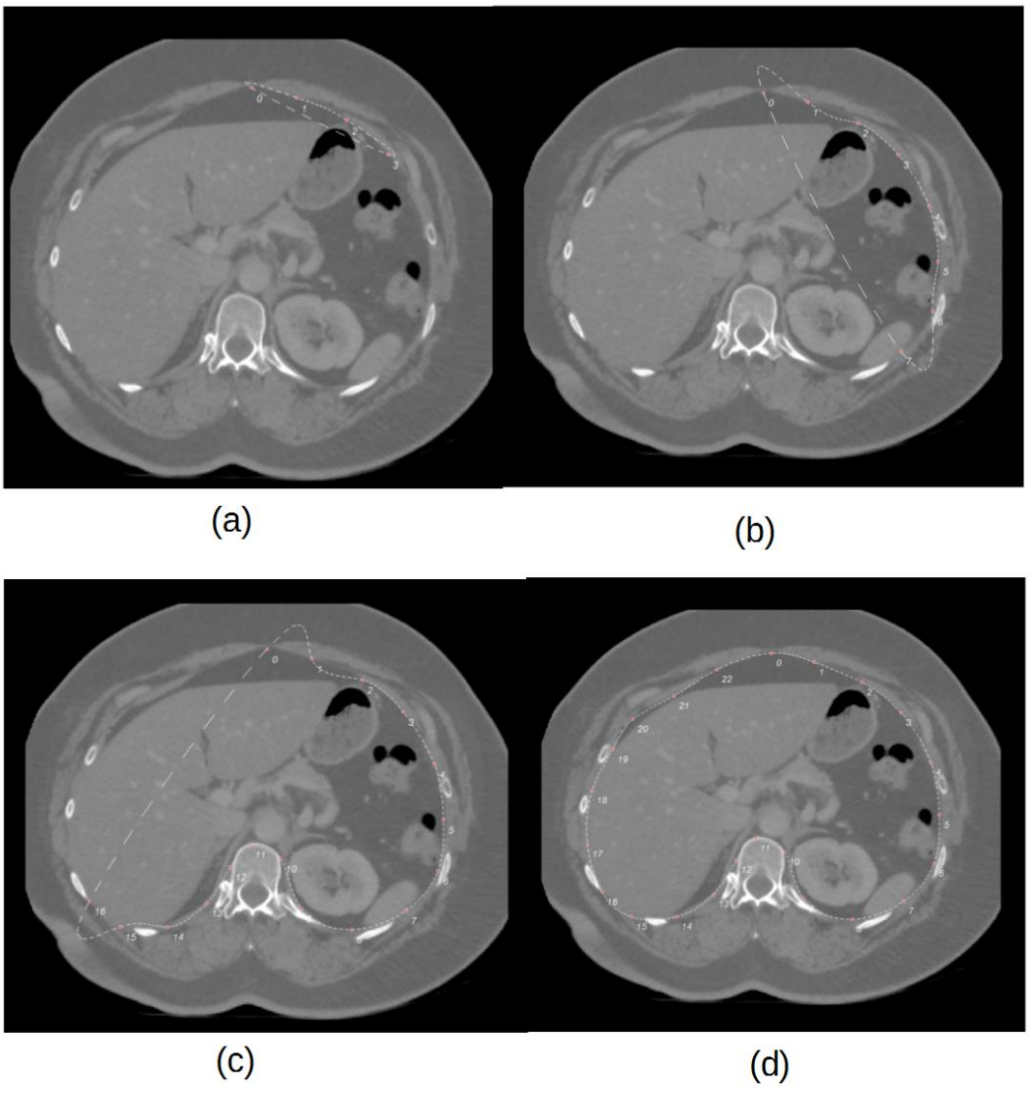

FIGURE 4.11: Illustration of the interactive segmentation on one axial slice.

The distance between adjacent control points is dependent on the curvature of the specific border. It is suggested that the control points should be more dense on the region with high curvature. For instance, if only two control points are put at the border of the spine, then the fitted spline curve cannot remove it completely in the final generated image. Once all control points are added at the boundary, the generated 2D spline curve should correspond to the border of the abdominal viscera (cf. FIGURE 4.11), and we can still modify slightly the place of control points to improve the segmentation accuracy. *The choice of the number of control points* is discussed in the next section.

Step 2: Once this first delineation is finished, the user selects the next slice image. The first created curve and its control points are automatically copied on the current. If the user did not select a new slice too far from the first one, only a few modifications are sufficient to update the curve which delineates the abdominal viscera. Although allowing the user to modify each control point independently seems to be the standard option, we choose another option in two stages that practically makes the delineation faster.

The first stage consists in allowing a linear expansion or shrink along the X or Y axis of the control point set. The software displays a rectangular bounding box around the control points and the user can independently modify each side of the box, the remaining ones being static (cf. FIGURE 4.12). For instance, the user move the side AB along the green row direction, the control points close to this side AB will linearly move in the same direction simultaneously, and the control points close to the opposite side CD will remain almost static. Usually, this kind of position refinement of control points is sufficiently accurate and in case some a few modifications are still necessary, the user passes to the second stage.

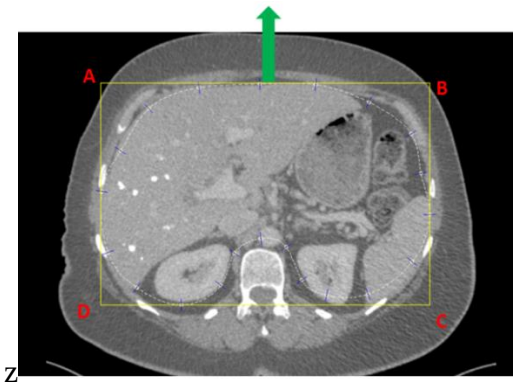

FIGURE 4.12: Illustration of the first stage of the position refinement with the use of a rectangular box ABCD.

During this second stage, the user can modify at the same time the position of a set of consecutive control points locally: the user selects 2 control points to define the zone which has to be refined, they will remain static (cf. FIGURE 4.13(a), where the two fixed control points are set in red, the red segment indicating the part of the whole curve, which will be moved). Then, he clicks on the frontier that he considers proper, and all the control points between the 2 fixed control points will move so that the curve reaches the clicked point (cf. FIGURE 4.13 (b)). The motion of each control point between the fixed points is linearly dependent on its distance to the mouse click. If the control point is the closest point on the curve to the mouse click, it will move exactly on the mouse click. If the control point is close to one of the fixed points, it will almost not move. The motions of the other control points are linearly computed from their weighted distance between the closest fixed point and the closest point on the curve to the mouse click. Depending on the necessary refinement, the user moves simultaneously 3 to 4 points only or sometimes 6 to 8 when a consistent motion occurs on a specific zone.

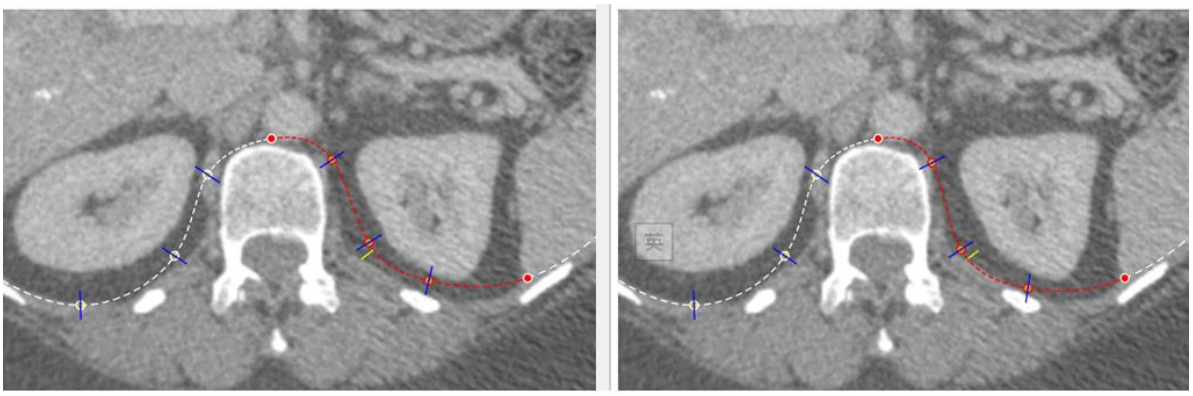

FIGURE 4.13: The second stage for the position modification of control points. (a)The two red control points are selected to define the curve segment for modification (b) The new position of control points after modification.

Step 3: the user selects a new axial slice, on which a copy of the control points from the closest segmented axial slice is performed. Then, the user can refine the control point positions using the 2 tools described earlier. After delineation of at least 4 slices with above tools, the boundary of abdominal viscera in all axial slices comprised between the first one and the last one (along the cranio-caudal axis) can be automatically generated with the use of a 3D B-spline-based interpolation technique.

This process is illustrated in the FIGURE 4.14: since the number N of control points is the same in each selected slice with manual interactive segmentation, it is easy to match the n^{th} point in slice i to its corresponding n^{th} point in slice j, and a 3D B-spline can be generated taking the position of these points as parameters. The intersection of this generated spline with unsegmented slice t generates the corresponding control point in the t^{th} slice (cf. FIGURE 4.14, where the point is coloured in green). From the control points in each slice, a 2D curve is then generated in all axial slices comprised between the first one and the last one.

Finally, a 3D mesh can be created that corresponds to the abdo-thoracic wall. Since all curves are continuous B-splines, the user can independently select the density of grid points along the axial 2D curves and the cranio-caudal 3D curves. The resulting mesh can thus be as dense as needed by the further application. Practically, the number of points on the axial 2D curves is set to 100 to ensure a smooth surface visualization.

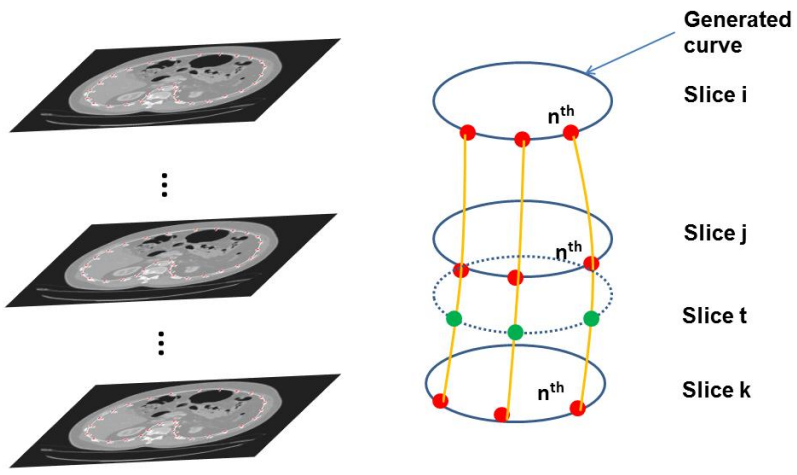

FIGURE 4.14 : The illustration of 3D B-spline interpolation along the cranio-caudal axis

Step 4: A final optimization step is required since the generation of most of the 2D axial curves is based on the 3D interpolation technique only. The optimization includes two aspects. The first one is the accuracy of the segmentation. The second one is the smoothness of the abdo-thoracic wall. In the lateral window which shows the image and the surface mesh, we can conveniently and quickly check the accuracy and smoothness by moving the slices and detect any mistake. For instance, if the ribs are not totally removed in some slices, we can directly locate the 2 slices surrounding this area on which control points had been defined, and modify the control point positions. In case this modification is not sufficient, it may mean that the abdo-thoracic wall is not sufficiently smooth in this area and a supplementary slice

should be manually adapted and validated between these 2 slices using the 2 tools previously presented. After having defined the new slice, all 3D B-splines are recomputed since the number of control points has increased by 1 in the crania-caudal direction. Obviously, if the user has only segmented 4 axial slices, he will certainly have to add several supplementary axial slices.

We illustrate in FIGURE 4.15 the segmentation results from the venous and arterial phases CT image with NSS equals to 20 and 10 respectively. The mesh model can be generated after the proposed 4-step segmentation and the 3D MPR displaying is used to better inspect the position of the mesh and its spatial relation with surrounding tissues, such as ribs and bones.

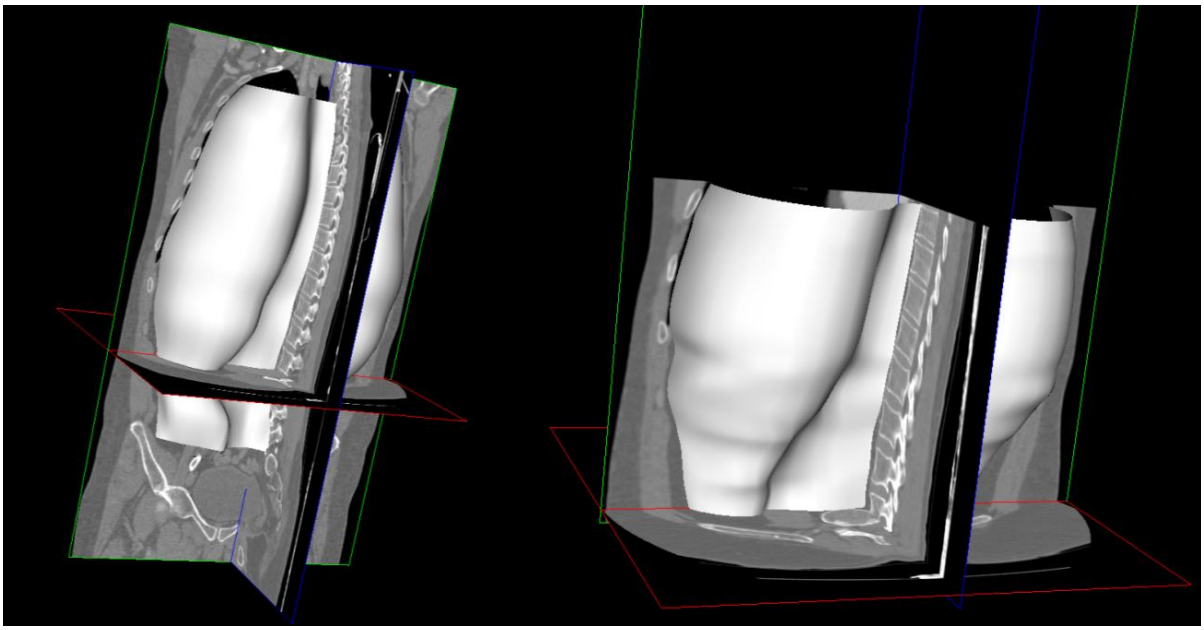

FIGURE 4.15: The generated meshes from the venous (left) and arterial (fight) phases CT image.

4.2.2 Discussion

In our approach, the generated curve in the first slice is copied to the two adjacent slices (below and upper in the cranio-caudal direction). These 2 slices are then copied to the next adjacent slice and so on. Thus, the choice of the first slice for manual segmentation is really important. Based on our experience, if we choose an axial slice below the liver where the peritoneum is quite smooth, then the user may put only 15 control points, which seems sufficient for the current slice. However when we slide to an axial slice close to the lungs, the curve may not perfectly fit the border of peritoneum even if we modify the position of the 15 control

points, since borders with high curvatures are located close to the ribs. It thus requires the curve to have a stronger local fitting capability, namely to increase the number of control points, which contradicts our design principle. On the other hand, if we put too many control points, for instance 50, the distance between control points of B-spline is very small (< 20 pixels) and it is difficult to generate a smooth curve which fit the border very well. Thus, we need to compromise the number of control point and the smoothness of the segmentation result.

We suggest the following principle for the first slice selection:

- The first slice should contain the lower part of the liver and the upper part of the psoas muscles.
- The number of control points for the first slice (and thus of all slices) should be between 20 and 25.
- The frequency of control points should be higher close to the spine (area with relatively higher curvature), typically 5 points.

The two tools we have designed move several control points at the same time. We have adopted this strategy because the border of abdo-thoracic wall in the axial view and in the cranio-caudal direction is very smooth. Thus, the variation of corresponding 2D and 3D interpolated curves should also be smooth. If we refine each control point independently, it will probably reduce the smoothness along the cranio-caudal axis since the user will not take care of their proper alignment in this direction. In addition, the manipulation of control points in group is more efficient and quicker compared to one-by-one operation. Thus, we expand or shrink the curve in group instead of point by point.

4.3 Diaphragm Segmentation Interactive tool

4.3.1 Description

In this section, we describe the interactive tool we have developed to quickly delineate the diaphragm. The principle is based on the same idea, the curvature of the diaphragm is rather smooth and thus the number of samples on its frontier can be limited even if millimetres accuracy is necessary. Although it is possible to use our tool without any prior peritoneum seg-

mentation, it is preferable to have one and this will be assumed in the remained of this thesis later.

Step 1: the user firstly selects a specific axial slice, the axial plane of reference (APR), which is the highest axial slice in the cranial direction that does not contain lung tissue. The software then automatically extracts from the previous abdo-thoracic wall segmentation the 2D curve already delineated in this specific slice, and selects *15* sagittal slices uniformly located between the right and left extremities of the 2D curves (cf. FIGURE 4.16 (a)). The user will have to perform the diaphragm segmentation in these sagittal slices (one example sagittal slice is provided in FIGURE 4.16(b)). The intersection of these sagittal slices and the 2D curve from the APR provide the beginning and end point of the diaphragm segmentation (cf. the 2 red circles in FIGURE 4.16 (b)).

Step 2: The software shows each sagittal slice one by one so that the user delineates the diaphragm boundary on each of them. The standard process is to click at one extremity and to draw the boundary as long as the mouse click is activated until the user reach the second extremity and then release the click action. We design a semi-automatic approach: we firstly draw 12 rays automatically based on the gradient information of the diaphragm in the sagittal view (cf. FIGURE 4.16(b)), which intersect in the middle of the segment, defined by the intersection of the sagittal slice and the 2D abdo-thoracic wall delineation in the APR (cf. the blue circle in FIGURE 4.16 (b)).

In fact, most of the time, the automatic computation of the ray length is sufficient due to the high gradient between the diaphragm and lung, which can accelerate the segmentation process (cf. FIGURE 4.16 (b)). However, it happens the end points of some rays are not on the diaphragm, but on another region which has higher gradient than the diaphragm boundary (cf. the marked rays by yellow circle in FIGURE 4.16 (b)). In this case, such rays can be modified interactively with our software. The user presses the “ctrl” keyboard and moves the mouse along the boundary until the mouse crosses the rays, which length is automatically reduced to fit the current mouse position. The choice of this technique over the standard one is discussed after the steps description.

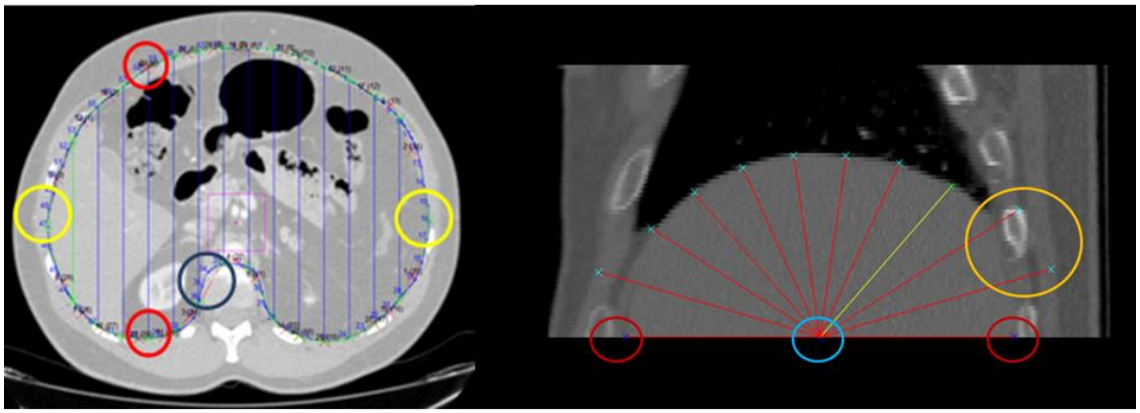

(a) (b)

FIGURE 4.16: Illustration of the mechanisms of the interactive diaphragm segmentation.

Step 3: Once all the sagittal slices have been processed by the user, the software automatically computes in each sagittal slice the 2D spline passing through all ray end points, and over-samples the curve from 12 points to 100 ordered points (which corresponds to the number of sampled points on the abdo-thoracic wall delineated in the APR between the 2 extremities). Then, considering the k^{th} point of the 2D spline in the 15 sagittal slices, a 3D spline can be generated with the position of these 15 points, and oversampled it from 16 points to 100 points (this process is illustrated in the FIGURE 4.17). An accurate quad mesh, describing the diaphragm position can finally be computed using all the generated points from the 2 over-sampling processes (cf. FIGURE 4.18).

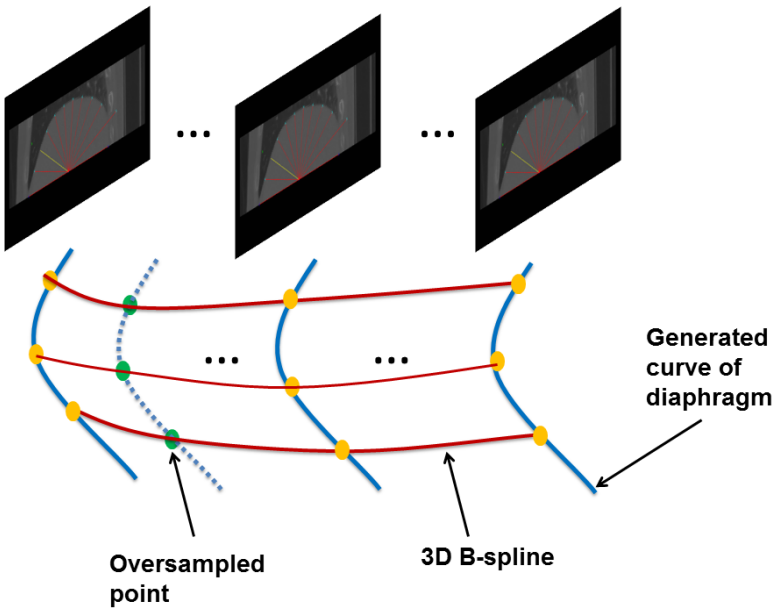

FIGURE 4.17: Illustration of the 3D Bspline interpolation along left-right axis

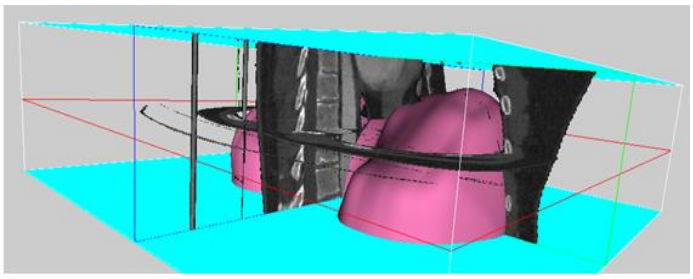

FIGURE 4.18: The created mesh (pink) represents the diaphragm. The number of selected slices in APR for manual segmentation in the sagittal view is 15, and 12 ray casts are created in each slice.

Practically, the creation of the 2D and 3D splines is not possible close to the points on the APR, since a further point is missing in the caudal direction. To overcome this problem, we artificially add a supplementary differential constraint on these points, i.e. the tangent extracted from the abdo-thoracic wall segmentation along the sagittal plane for 2D splines and along the middle frontal plane for 3D splines.

Finally, combining two fast segmentation tools, a mesh model containing only the thoracic viscera can be obtained (cf. FIGURE 4.19).

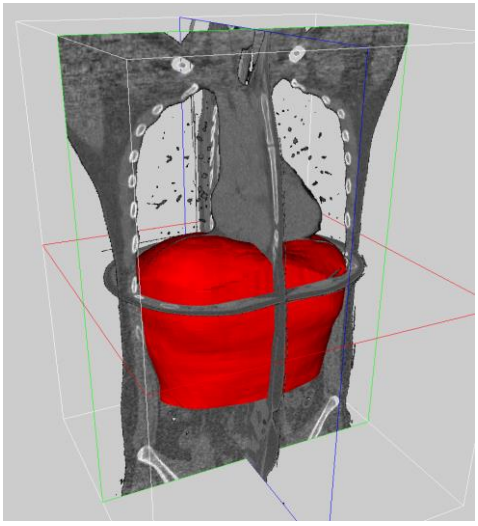

FIGURE 4.19: The generated mesh (red) containing only the abdominal viscera

4.3.2 Discussion

The choice of the APR is more motivated by the liver and spleen frontiers than by the real diaphragm position. Regarding the number of sagittal slices (15) and samples (12) in each sagittal slice, they were chosen empirically by experts who think that this can ensure a very accurate interpolation of the upper viscera boundary in the sagittal view.

The choice of the method allowing to select the ray cast length is certainly one of the most important in our context, where duration should be reduced as much as possible. We originally decided to let the user click and draw the frontier, as it is the case in most standard software. However, we quickly notice that the user often has to redo his drawing when he loses his mental focus, even if almost all the drawing is perfect. Obviously, an eraser tool could allow users to correct the mistaken area, but this action also takes time.

The big advantage is that it allows an extremely efficient of correction of the area where a mistake occurs. The closest ray cast can be automatically activated when the mouse moves toward it, and its length will be adapted to the current position of the mouse in its original direction. The updated length can be conveniently validated using a keyboard control instead of using the mouse left button. Indeed, it avoids the hand tremor when the user clicks on the mouse and maintains pressed the left button. We observed that all users needed two to three times less time to validate the diaphragm frontier with our interface.

4.4 Evaluation of the number of selected slices and tool efficiency

We argued that delineating all slices was not necessary for abdo-thoracic wall, particularly because nowadays resolution of medical imaging device is close to a millimetre. However, how to choose the number of selected slices (NSS) for manual segmentation so that it can provide an accurate 3D surface model, which has a comparable accuracy with a delineation of all slices?

The purpose of this section is to quantitatively answer this question. In particular, we want to find the best trade off so that one has to delineate as few slices as possible, keeping in mind that if too few slices are chosen, the segmentation result might not be satisfying. We will also obviously report the time needed by our method to perform both delineations and evaluate the learning curve of our two segmentation tools.

4.4.1 Experimental set up for the NSS

Using 20 patient CT data (resolution of $512 \times 512 \times 292$ with voxel size of $0.961 \times 0.961 \times 1.8$ mm), our medical staff performed a segmentation with our peritoneum segmentation tool for each of them using 50 slices. The length of acquired abdominal-thorax volume data along the z axis is on average 45 cm. The patient selection was performed randomly among an important database of patients and has an important variability. An expert had previously defined that the segmentation with 50 slices (roughly 1 slice/cm) could be considered as ground

truth due to the low curvature of the abdominal wall. This was mathematically confirmed using the Shannon theory. Then, a selection of 20, 10 and 5 slices uniformly sampled among the 50 delineated slices was carried out and a dense 3D mesh G50, S20, S10, S5 was created for each patient from the segmentation with 50, 20, 10 and 5 slices, using the 3D spline based interpolation described in the previous section. Finally, the surface models S20, S10 and S5 can be compared to the ground truth G50 and the difference between them can be measured by computing the distance from a vertex of the surface models to the closest point belonging to G50.

4.4.2 Results for the choice of NSS

FIGURE 4.20 shows the distance histogram between meshes S20, S10 and S5 with M50 on 2 patient data. We can see that the distance distribution of points is almost the same for S20 and S10 (peak at around 0.6 mm). But for NSS equals to 5, there are many points which distance are larger than 0.8 mm. We also calculate the total average distance and standard deviation between surfaces S20, S10, and S5 with G50 on 20 patient data (cf. Tab. 1). It clearly shows that the mean error is reduced from 1.27 mm (NSS = 5) to 0.84 mm (NSS = 10) which correspond to the voxel size and thus to the ground truth accuracy. However, there is only a slight improvement in accuracy for the NSS increased from 10 to 20.

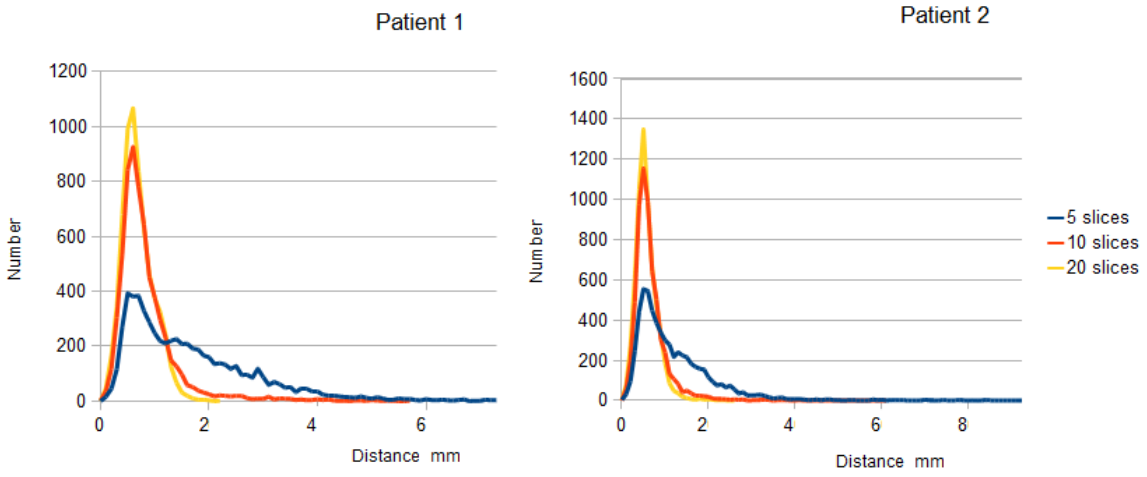

FIGURE 4.20: Distance histogram between S20, S10, S5 and G50. The x axis represents the distance (mm) and the y axis represents the number of points (vertex) at the corresponding distance.

Table 4.1: Average distance and standard deviation between surfaces S_{20}, S_{10}, S_5 and the ground truth G_{50}.

	5 slices	10 slices	20 slices
Average distance (mm)	1.27	0.84	0.71
SD (mm)	0.99	0.52	0.36

From these statistical charts and tables, we can conclude that the NSS for interactive segmentation should be chosen below 20, but above 10.

4.4.3 Evaluation of the segmentation duration

We have evaluated the time needed by 6 users to perform the segmentation of the abdo-thoracic wall and diaphragm of the 20 medical images of patient abdomen from the previous section. We removed from the average value the 2 first segmentations since they were much longer due to the learning curve. Users were 2 engineers, 2 surgeons and 2 radiology technicians.

The time cost on the segmentation of abdo-thoracic wall and diaphragm for each user has been summarized in the TABLE 4.2. Results show that the abdo-thoracic wall segmentation is performed on average in 363 s. (5 min.) and that the diaphragm segmentation is performed in 215 s. No significant difference was reported between the 3 classes of users. This experiment also shows that the abdo-thoracic wall can finally be fully segmented with an excellent accuracy and in a very reasonable time compared to clinical workflow constraints.

TABLE 4.2: The time cost for the segmentation of AW and diaphragm

	User 1	User 2	User 3	User 4	User 5	User 6	Total
AW (sec.)	375±24	295±37	384±41	347±35	361±34	420±44	363.6±41
Diaphragm (sec.)	211±32	215±31	189±24	260±34	175±23	243±37	215.0±31
Total	586	510	573	607	536	663	579.1

AW: Abdo-thoracic wall

4.5 Application: Visualization of the image without abdo-thoracic wall and diaphragm

Although *a priori* knowledge of sliding area is employed in this thesis for registration purposes, we show here that it can be also used for a different application, more specifically the patient organ visualization. Its critical application in the registration of abdominal image can be seen in the Chapter 5.

The volume rendering display of medical data is now available on each radiological console and allows a 3D visualization of the patient data, which can be extremely useful to plan resection planes in case of liver tumor dissection or to assess relative positions of vessels (A. Shimizu et al., 2007; Bano et al., 2012a). Since the abdo-thoracic wall (which contains fat, muscles and bones) cannot be automatically removed from the medical data, a practical solution is to modify its opacity to view the inside organs using the transfer function. Although the transparency setting enables to view the abdominal organs much more clearly, it simultaneously makes some part of the organ transparent since the intensity value between abdo-thoracic wall and abdominal organs are very similar. Thus, a preliminary segmentation of abdo-thoracic wall can effectively remove or eliminate this issue to help surgeons obtain a better understanding of the patient's anatomy.

We show below on 2 patient data the benefit of abdominal wall removal. We compare the volume rendering visualization of the original image with the same image after removal of the abdo-thoracic wall and diaphragm. This is performed by setting voxels outside of the the viscera segmentation to -1024 (cf. FIGURE 4.21: The new images containing only the abdominal viscera are created by two segmentation tools. The first and second rows are from two patients respectively. The three columns represent the displaying in axial, frontal and sagittal views, respectively.).

The first patient has several tumors in his liver and a proper visualization of the liver shape is important to assess the position of the resection planes. We show on the left of FIGURE 4.22, the original image where one can see that the ribs and cartilage does not allow to clearly see the liver shape. We highlight that no standard transfer function available in the software allows to completely remove the bones without degrading the image. We have also tried to manually modify the transfer function, but results are still not acceptable for a clinician. On

the contrary, the image without abdo-thoracic wall (cf. right in FIGURE 4.22) clearly allows a good visualization and understanding of the liver shape.

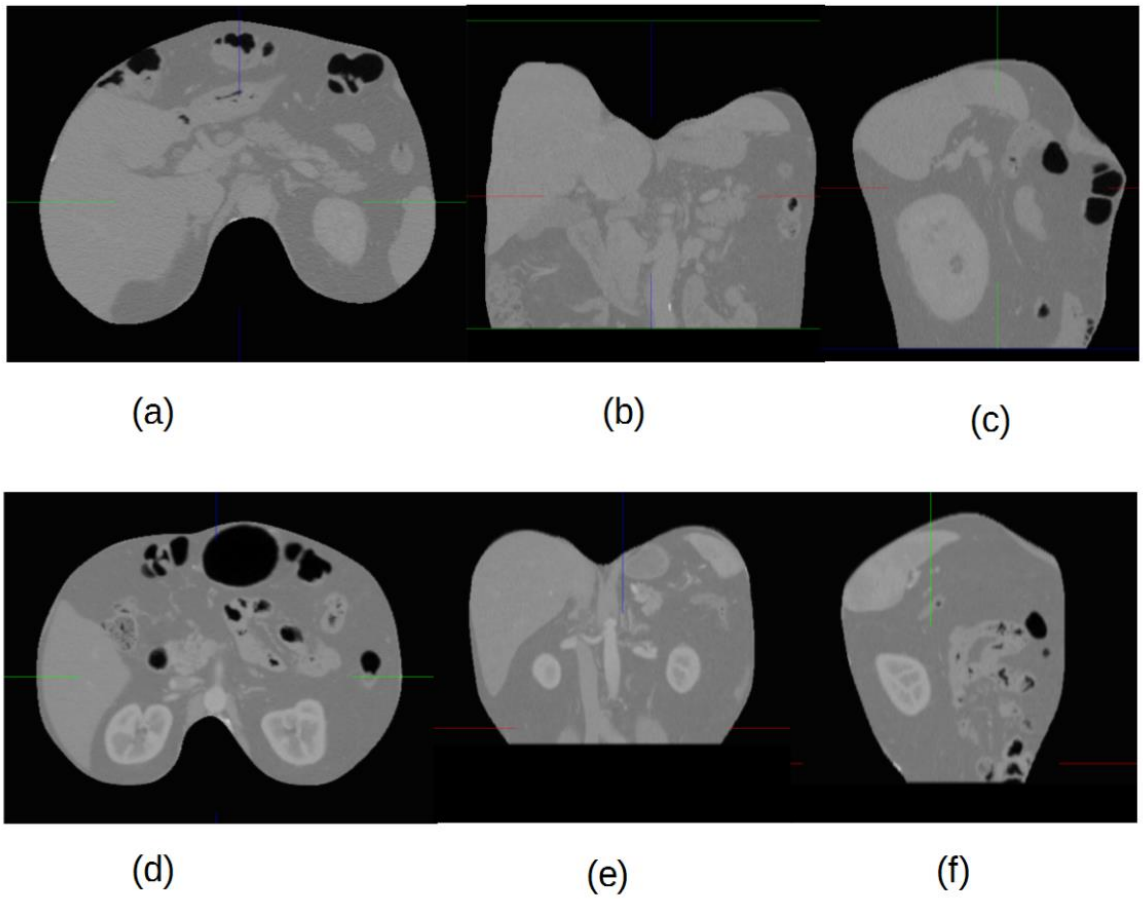

FIGURE 4.21: The new images containing only the abdominal viscera are created by two segmentation tools. The first and second rows are from two patients respectively. The three columns represent the displaying in axial, frontal and sagittal views, respectively.

The second patient has a tumor in the left kidney and an assessment of the positions of the renal artery and vein is important. This is usually done from a back point of view. The left of FIGURE 4.23 shows that the spine prevents the user from seeing clearly structures surrounding the kidneys. Again no transfer function allows to remove the spine from image. We have thus tried to crop the volume in order to remove the spine (using the standard bounding box cropping tool: it removes here from the volume rendering a stack of frontal slices in the patient back that contains the spine). However, such process also degrades the structures we are interested in since they are also contained in the frontal slices embedding the spine (cf. middle

in FIGURE 4.23). Obviously, this problem is overcome if the abdominal wall is removed with our method, as can be checked in the right of FIGURE 4.23.

FIGURE 4.22: Illustration of the benefit of abdominal wall and thoracic viscera for patient data visualization. Left: original CT image. Right: new image where voxel value corresponding to abdominal wall and thoracic viscera has been set to -1024.

FIGURE 4.23: Illustration of the benefit of abdominal wall and thoracic viscera for patient data visualization. Left: original CT image. Middle: original image after cropping using bounding box tool. Right: new image where voxel value corresponding to abdominal wall and thoracic viscera has been set to -1024.

4.6 Conclusion

In this chapter, we have presented two interactive but fast tools for the segmentation of the abdo-thoracic wall and diaphragm. Our choice has been motivated by the unsatisfactory result obtained by previous approaches which mostly fail due to important variation of grey level along the viscera interface. Since the abdo-thoracic wall and diaphragm have a somewhat smooth curvature, we believe that an interactive tool which automatically generates a surface from relevant points or lines drawn by the user in some slices only, can be sufficient to properly interpolate the whole abdo-thoracic wall and diaphragm.

In particular, we have carefully described our methodology and explained why it allows the user to perform both segmentations efficiently. We have provided experimental results on 20

patients, which showed that a NSS of 15 is enough to reach an excellent accuracy and can be completed within 5 minutes. We have also observed that practicing on one or two patient data was enough for the new users to be experienced. On average, we evaluated with 6 users that both segmentation could be finished within 600 seconds (10 minutes). We finally provided visualization result using our segmentation methods, which exemplify how useful our tools can be in such medical image analysis area.

We would like to emphasize that the *abdo-thoracic wall segmentation* can also be important for breathing and surgical simulation. For instance, Hostettler et al., 2010 proposed a breathing model that can be used in radiotherapy and interventional radiology, but which relies on a segmentation of the abdo-thoracic viscera (cf. FIGURE 4.24) and the creation of independent structured grids of abdominal and thoracic viscera (Hostettler et al., 2010).

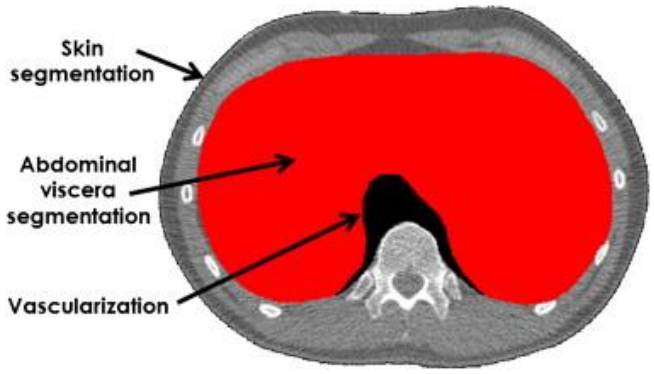

FIGURE 4.24: The segmentation of the abdo-thoracic viscera on a CT image by using the VRMed software. The figure originated from the paper of Hostettler et al. (2010).

Bano et al., 2012b developed a patient specific pneumoperitoneum simulator to predict the abdominal organ motion after the gas injection. His work relies on the modelling of the thoracic and abdominal viscera (cf. FIGURE 4.25), which are easily available if a proper abdominal wall segmentation can be realized. Obviously, in case such work had to be used in a hybrid OP room containing a CT acquisition device, the segmentation should be performed in a few minutes. All these works clearly show the benefit of the abdo-thoracic wall segmentation as a prior knowledge for registration or simulation applications. It is interesting to note that the diaphragm delineation is also necessary in the previously mentioned applications, and is not as easy as one could imagine.

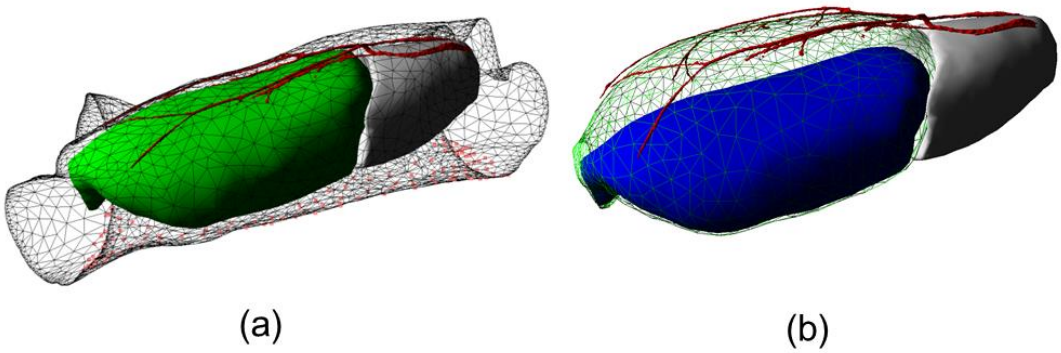

FIGURE 4.25: The simulation of the abdominal wall lift with an applying force (a)Before simulation (b) After simulation. Black wireframe: skin; Green: abdominal cavity; White: thoracic viscera; Blue: abdominal viscera; Red: abdominal wall arteries. The figures are from the paper of Bano et al. (2012a) .

Chapter 5 Abdominal wall & diaphragm removal for accurate non-rigid registration of multiphase clinical image

We have explained that the registration of multiphase CT image on abdominal viscera is extremely important for surgical planning. This registration is still a challenge due to the sliding interface between the abdominal wall and the abdominal viscera, which led us to develop two interactive software allowing a quick delineation of this interface, so that this interface can used as *a priori* information for the following registration step.

In this chapter, we propose a simple approach to use the preliminary delineation of the AW and diaphragm for the registration of abdominal multiphase CT. In the first section, we explain our registration strategy based on the removal of AW and diaphragm in the original images, then the details of each step is described. In section 5.2, the experimental setting is described, including image data pre-processing and evaluation metrics. In section 5.3, we present the experimental results, which demonstrate the registration accuracy improvement with our proposed approach compared to standard ones.

5.1 Methodology

5.1.1 Overview of our approach

Our strategy is to use the delineation of the AW and diaphragm in the source and target images to create new images containing abdominal viscera only. In order to evaluate the supplementary benefit of diaphragm removal, we create a set of images without the AW and a supplementary set without AW and Thoracic Viscera (AW&TV). Then, two state-of-the-art non-rigid registration algorithms are applied to each of the original image, the new generated image without AW and without AW&TV. The flowchart is illustrated in FIGURE 5.1.

The first step is the acquisition of multiphase CT image data. Subsequently, since performing the non-rigid registration on the CT image with original size is a huge load for computation time and memory requirement, a cropping and sub-sampling operation is conducted. The interactive segmentation of AW and diaphragm can be completed within 10 minutes as we described in the Sec.4.4.

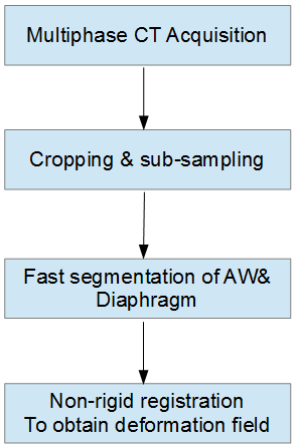

FIGURE 5.1: Flowchart of our approach on abdominal image registration.

Then, we propose two non-rigid registration algorithms for the non-rigid registration, one consists of using a B-spline based transform function and Mattes mutual information (MMI) as a similarity metric (cf. Sec.5.1.2), its implementation is described, including the main code function to ensure the reproducibility of our work by others. The other one is called Super Baloo (cf. Sec.5.1.3) which is based on a pyramidal block-matching algorithm using squared correlation coefficient (SCC) as a metric and has been proved robust and efficient in thorax image registration (Garcia et al., 2010; K. Murphy et al., 2011).

5.1.2 B-spline-based non-rigid registration

The goal in multi-modal CT abdominal image registration is to find a spatial transformation $T(x, y, z) \rightarrow T(x', y', z')$ that correctly maps any point in the source image $I(x, y, z, t)$ at a time t into the corresponding point in the target image $I(x', y', z', t_0)$, taken at the time t_0. Though research has shown that the abdominal-thoracic motion is mainly along superior-inferior (SI) direction during breathing, the antero-posterio and left-right motions can still not be neglected for the sake of a realism requirement registration. Obviously, taking all of these factors into account, using a rigid or affine transformation only is not sufficient to accurately describe this spatial transformation. Therefore, we choose a combined transformation T which contains global transformation (rigid and affine) and local deformable transformation based on free form deformation (FFD):

$$T(x, y, z) = T_{localDeformable}\left(T_{globalAffine}\left(T_{globalRigid}(x, y, z)\right)\right) \quad (5.1)$$

Firstly, the rigid transformation is employed to align the source image with the target image. The output transformation parameters are used to initialize the corresponding member variables in the following affine transformation. After applying global rigid and affine transformation on the abdominal viscera, an additional deformable registration is required to implement the local deformation, since the shape of abdominal organs is also deformed by elastic forces generated by the breathing motion. Therefore, we choose a B-spline-based FFD model whose ability in modeling the local 3D deformation field has been applied and proved (Rueckert et al., 1999; S. Lee et al., 1997; Rueckert et al., 2006; Glocker et al., 2008;K. Murphy et al., 2011).

5.1.2.1 Choice of similarity metric

For the registration of arterial and venous phase CT image data, it is necessary to define a registration metric. The intensity value difference between these two data types for same organs prevents from using standard criteria used for mono-modal registration, e.g. sum of squared differences. An alternative approach is MI which is a concept from the information theory. MI means how much information of one random variable contains about another random variable and should be maximized if the corresponding regions of two images overlapped. This was introduced into medical image registration area by Collignon and Viola independently (Collignon et al., 1995; Viola & Wells III, 1997) and has also been reporeted as an accurate and robust similarity measurement in the literature (Pluim et al., 2003; Sakai et al., 2015).

Regarding the registration of two images, we assume that the MI would be maximized if the corresponding regions of two images overlapped. The computation of MI about one image A with another image B is as following:

$$I(A, B) = H(A) + H(B) - H(A, B) \qquad (5.2)$$

where $H(A)$ and $H(B)$ denote the marginal entropy of image A and B respectively, $H(A, B)$ denotes the joint entropy of A and B, which can be calculated from the joint histogram of A and B. In this method, we adopt the class itk::MattesMutualInformationImageToImageMetric to implement the similarity measurement. More details can be obtained via accessing the user guide (Schroeder et al., 2003).

5.1.2.2 Implementation of the algorithm

The ITK is an open-source and cross-platform library that has been widely used in theimage segmentation and registration field. The details of how to configure, compile and integrate it into our application can be found on the official ITK website ("ITK," 2003). In our registration approach, the main steps are written as following:

1. Read multi-phase source and target images and initialize the registration framework in ITK.

```
registration->SetMetric(MattesMutualInformationMetric)
registration->SetTransform(rigidTransform);
registration->SetOptimizer(optimizer);
```

2. Set the parameters for the rigid registration, and start it:

```
metric->SetNumberOfHistogramBins( 50 );
optimizer->SetMaximumStepLength( 0.2000  );
optimizer->SetMinimumStepLength( 0.0001 );
optimizer->SetNumberOfIterations( 250 );
MattesMutualInformaitonMetric->SetNumberOfSpatialSamples(10000);
registration->StartRegistration();
```

3. After completing the rigid registration, we set the parameters of the affine registration, the final rigid transform parameters being assigned as input for the affine transform:

```
affineTransform->SetMatrix(rigidTransform->GetMatrix());
affineTransform->SetTranslation(rigidTransform->GetTranslation() );
MattesMutualInformaitonMetric->SetNumberOfSpatialSamples(10000);
```

4. B-spline-based multi-resolution registration for obtaining the local deformation field with the use of multi-resolution. We firstly perform the lower level:

1) Lower resolution level:

```
bsplineTransformCoarse->SetNumberOfGridNodesInOneDimensionCoarse();
bsplineTransformCoarse->SetGridSpacing( spacing );
bsplineTransformCoarse->SetGridOrigin( gridOrigin );
bsplineTransformCoarse->SetGridRegion( bsplineRegion );
bsplineTransformCoarse->SetGridDirection( gridDirection );
bsplineTransformCoarse->SetBulkTransform( affineTransform );
optimizer->SetMaximumStepLength( 10.0 );
optimizer->SetMinimumStepLength(  0.01 );
optimizer->SetRelaxationFactor( 0.7 );
optimizer->SetNumberOfIterations( 50 );
```

2) Higher resolution level. After performing the coarse level registration, the coefficients of the B-spline grid at this low level are used to initialize the corresponding coefficients for the higher resolution image.

```
bsplineTransformFine->InitializeCoefficients(); //compute it based on
the   coefficient from lower resolution bspline
bsplineTransformFine->SetGridSpacing( spacingHigh );
bsplineTransformFine->SetGridOrigin( gridOriginHigh );
bsplineTransformFine->SetGridRegion( bsplineRegion );
bsplineTransformFine->SetGridDirection( gridDirection );
bsplineTransformFine->SetBulkTransform( affineTransform );
```

B-spline transform is not capable of accounting for big rotations or shearing differences. In order to compensate for this limitation, we perform first the global rigid and affine registration. With the use of a multi-resolution registration scheme, we can effectively improve the accuracy, speed and robustness of the algorithm.

5.1.3 Super Baloo non-rigid registration

To make the evaluation more convincing, another robust and automatic non rigid registration algorithm was selected. It is based on block-matching scheme and demonstrated good results in recovering large displacements in thoracic image registration.

Given a source image F and a target image R, the registration process estimates a dense transformation T (one displacement vector per voxel) to superimpose F on image R: $R \approx F \circ T$. To achieve this purpose, an iteractive framework with a multi-resolution scheme is used.

At each iteration l, blocks are regularly placed on the target image R, and for any block $B(x_v) \subset R$ (x_v being the center), the best match block $B(y_v)$ in the local neighborhood position $V(x_v)$ of corresponding source image $F \circ T^{l-1}$ will be searched. The criteria of this best match is defined according to the similarity measurement S,

$$y_v = arg \max_{y \in V(x_v) \subset F \circ T^{l-1}} S\big(B(x_v), B(y_v)\big). \qquad 5.3$$

$S\big(B(x_v), B(y_v)\big)$ represents the similarity measurement between the two blocks $B(x_v)$ and $B(y_v)$. According to experiments described in (Garcia et al., 2010), the chosen size of matching block is 5×5×5 voxels. It means that a small number of tissue classes are presented in each block, which fits well the use of squared correlation coefficient (SCC) as similarity metric. At the end of this iteration step, a set of pair points (x_v, y_v) is obtained, and a sparse deformation field $C(x_v)$ can be calculated:

$$C(x_v) = y_v - x_v \qquad 5.4$$

If we define the S_v as optimized similarity value for the block $B(x_v)$, then the dense transformation δT^l can be interpolated by convolving C with a 3D Gaussian:

$$\delta T^l = \frac{G_\sigma * (S_v C)}{G_\sigma * S_v} \qquad 5.5$$

where σ represents the standard deviation of the Gaussian, allowing to compute a smoother or sharper displacement field. This interpolation can also be seen as a fluid regularization of the transformation proposed in (Christensen et al., 1996) with the aim of reducing the influence of outliers. Finally, the obtained dense deformation from the full resolution source image will be used to resample the floating image to get the registration result. In this paper, we use the software platform MedINRIA (Ourselin et al., 2000) which has integrated this algorithm.

5.2 Experimental setup

5.2.1 Image data

We performed our evaluation on 10 patient multiphase CT scans arterial and venous phase). The original size of the venous phase image is roughly 512×512×500 (resp. arterial 512×512×400) with an average spacing of 0.961×0.961×0.961 mm. Following the recommendations on the ITK website, we cropped and sub-sampled by a factor 2 along the cranio-caudal axis and brought the venous phase image size to 512 × 512× 250 (resp. arterial 512×512×200) with average spacing of 0.961×0.961×1.8 mm. Since we want to evaluate the benefit of the removal of AW&TV, we use three sets of images: one is the original image with AW&TV, the second one is the new image without AW (FIGURE 5.2) and the third image is without AW&TV. The venous phase image is used as the target image, and the arterial phase image as the source image.

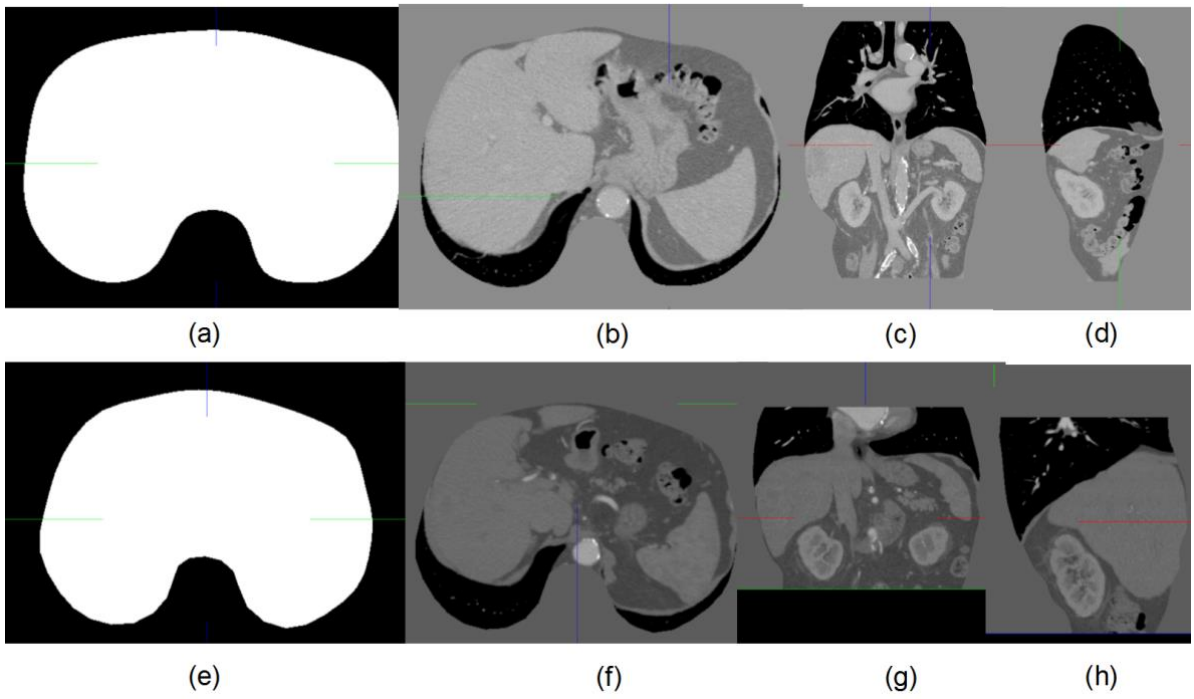

FIGURE 5.2: The generated result of the AW segmentation from venous (first row) and artery (second row) phase. The example of mask image (a, e) and new images in axial (b, f), frontal (c, g) and sagittal (d, h) view. The new volume image containing the abdo-thoracic viscera only is created by replacing the voxel values outside the mask by 0 in order to visualize better of the lung boundary

5.2.2 Evaluation metric

Performance evaluation of an image registration algorithm applied to real images is not straightforward (Mattes et al., 2003;Salvi et al., 2007). The lack of ground truth prevents from the possibility of automatic assessment of the registration accuracy (Maes et al., 1999). In the case of registration with linear transformation models, the retrospective evaluation can be performed if fiducial markers are set before the image acquisition is conducted (J. West et al., 1997). However, this metric is not suitable in our context since it is difficult to place fiducial markers for the registration in the abdominal region. For registration where placing the fiducial markers is not available or possible, some researchers have turned to evaluate or validate the registration result with the use of physical/simulated phantom or other simulated data (W. P. Segars et al., 2010;W. Paul Segars et al., 2001). Though this method can provide some insight on the performance of the algorithm, the evaluation result is still not very meaningful on real images.

Since there is no gold standard for the image registration evaluation, we propose three common metrics to evaluate the final registration accuracy. The first evaluation metric is to qualitatively inspect the result images by overlapping them in 2D which can directly indicate the registration performance. Though the direct superimposition is not accurate and prone to error, an experienced physician can roughly assess the quality of the registration in a very short time if the displaying manner is friendly. In addition, these experts have *a priori* knowledge of where the region should be accurately registered and where relaxed accuracy is acceptable.

From the result point of view, the registration is a smooth and continuous mapping between corresponding points in the source image and those in the target image (Ashburner, 2007;M. Miller et al., 1997; M. I. Miller et al., 2005;). This mapping can be represented as a deformation field which can explicitly display the transformation position of each point (Llibre et al., 2007; Tittgemeyer et al., 2002; J. Helman & Hesselink, 1989; J. L. Helman & Hesselink, 1991; Tittgemeyer et al., 2002). Thus, we also qualitatively analyze the displacement vector of the deformation field and check the realism of the registration.

The second metric is the quantitative measurement of distance of critical organ surfaces after the registration. Four organs (liver, left/right kidney, spleen) were segmented semi-automatically on both the source and target images, the surface mesh model of each organ being generated with the use of the Marching Cubes algorithm. The proposed registration will

output the transformed source image and the deformation field. Let $\vec{D}$ represents one displacement vector of deformation field and A the corresponding coordinates of a mesh vertex from source image, then the new transformed vertex coordinates A' can be obtained with the following formula:

$$A'(x', y', z') = A(x, y, z) + \vec{D}(x, y, z) \qquad (5.6)$$

The spatial position and shape difference between these new transformed meshes and those from the target images are visualized in 3D and quantitatively compared. The distance is defined as the length of the orthogonal projection of the gravity center G of the source mesh triangles on the closest triangle of the target mesh. The contribution of each triangle is weighted according to its area size. Statistical measurements such as the average distance, standard deviation (SD) and maximum distance are calculated to assess the result quantitatively.

The third metric consists in measuring the vessel bifurcation registration error in the abdominal viscera region. For each patient data, five or six specific vessel bifurcations were selected in the abdominal region of target image and identified in the corresponding source image by an anatomy expert. The average distance between these bifurcation pairs are provided.

5.3 Results

All the image processing and the registration algorithms are performed on a computer with an Intel ® Core (TM) i7-2600(3.40GHz) processor coupled to 16GB of RAM. The algorithms are compiled with Visual Studio 2012 in 64 bits. The four organs (liver, left/right kidney, spleen) were segmented interactively with use of the VRMed software("VRMED," 2005).

5.3.1 Image comparison

FIGURE 5.3 and FIGURE 5.4 show a qualitative comparison of the B-spline+MMI and Super Baloo algorithm with two different patient cases respectively. The results are displayed by superimposing the registered image (colored in green) on the original fixed image (colored in red) and the opacity is modified for better inspection. The three rows represent the fused image before registration, registration with AW&TV and registration without AW&TV. The three columns represent axial, frontal and sagittal view respectively. We can see that the big displacement of ribs in the original image especially shown in the sagittal view of the first row (FIGURE 5.3 (c) and FIGURE 5.4 (b) & (c)) is effectively improved in the registration result with AW as shown in second row (FIGURE 5.3 (f) and FIGURE 5.4 (e) & (f)). Howev-

er the big sliding motion and the deformation of abdominal organs have not sufficiently improved. This observation holds for all other patients, where ribs and spines lead the registration due to the high contrast of the bone. The registration results without AW&TV are illustrated in the third row of FIGURE 5.3 and FIGURE 5.4, respectively. To better inspect the registration improvement, we selected some parts of the organ boundary as the region of interest (ROI) and modified the opacity of the top layer image. It revealed that the previous big displacements are compensated for and the boundaries of the abdominal organs from the source and target images are correctly aligned. In the axial view of FIGURE 5.4(g) and FIGURE 5.4(g), we can see that the boundary sections of the liver and kidney with high curvature are well aligned.

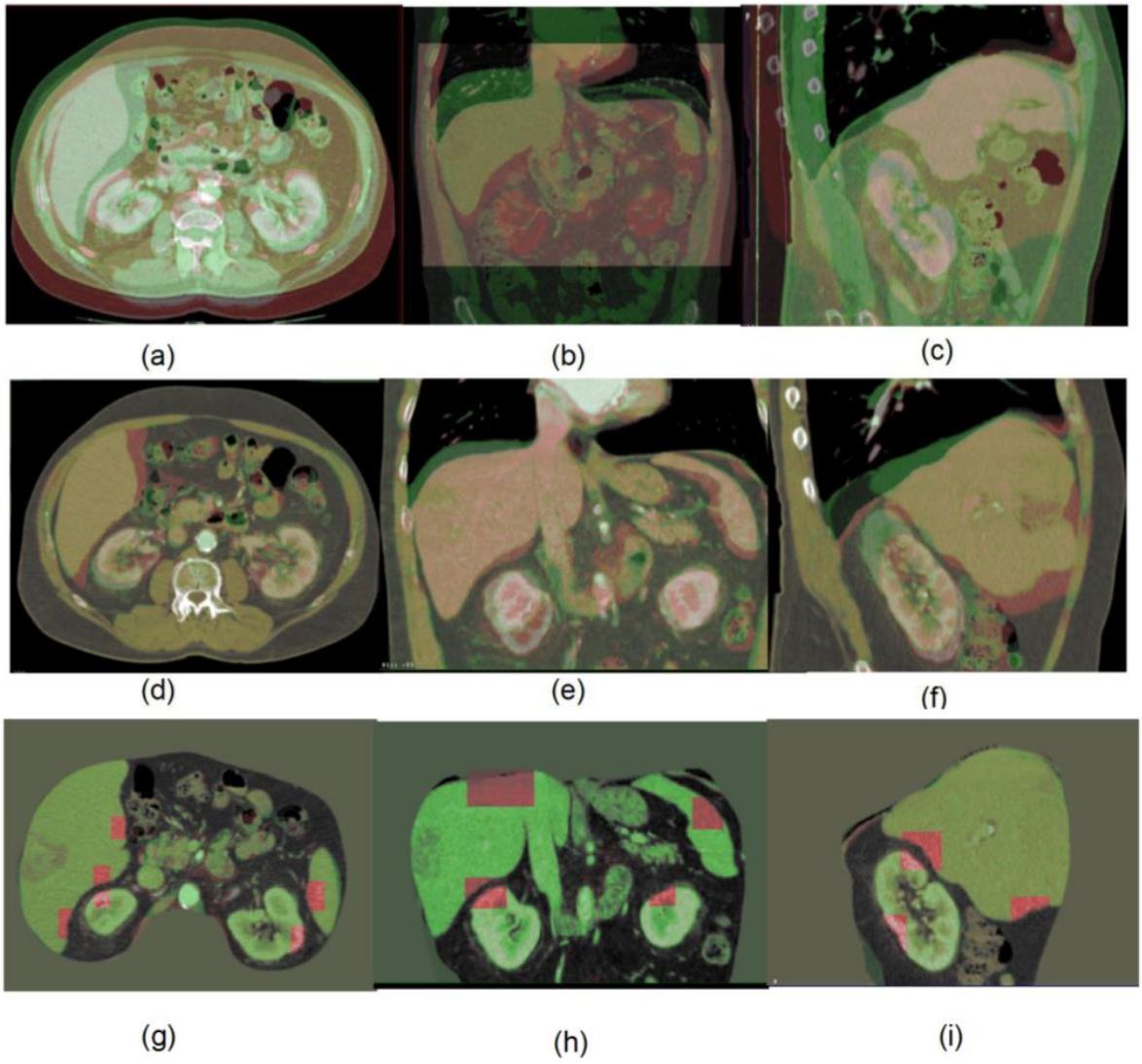

FIGURE 5.3: Registration result comparison with B-spline+MMI algorithm on one patient. The three rows represent the fused image before registration, registration with AW&TV and

registration without AW&TV. The three columns represent the axial, frontal and sagittal view of volume images.

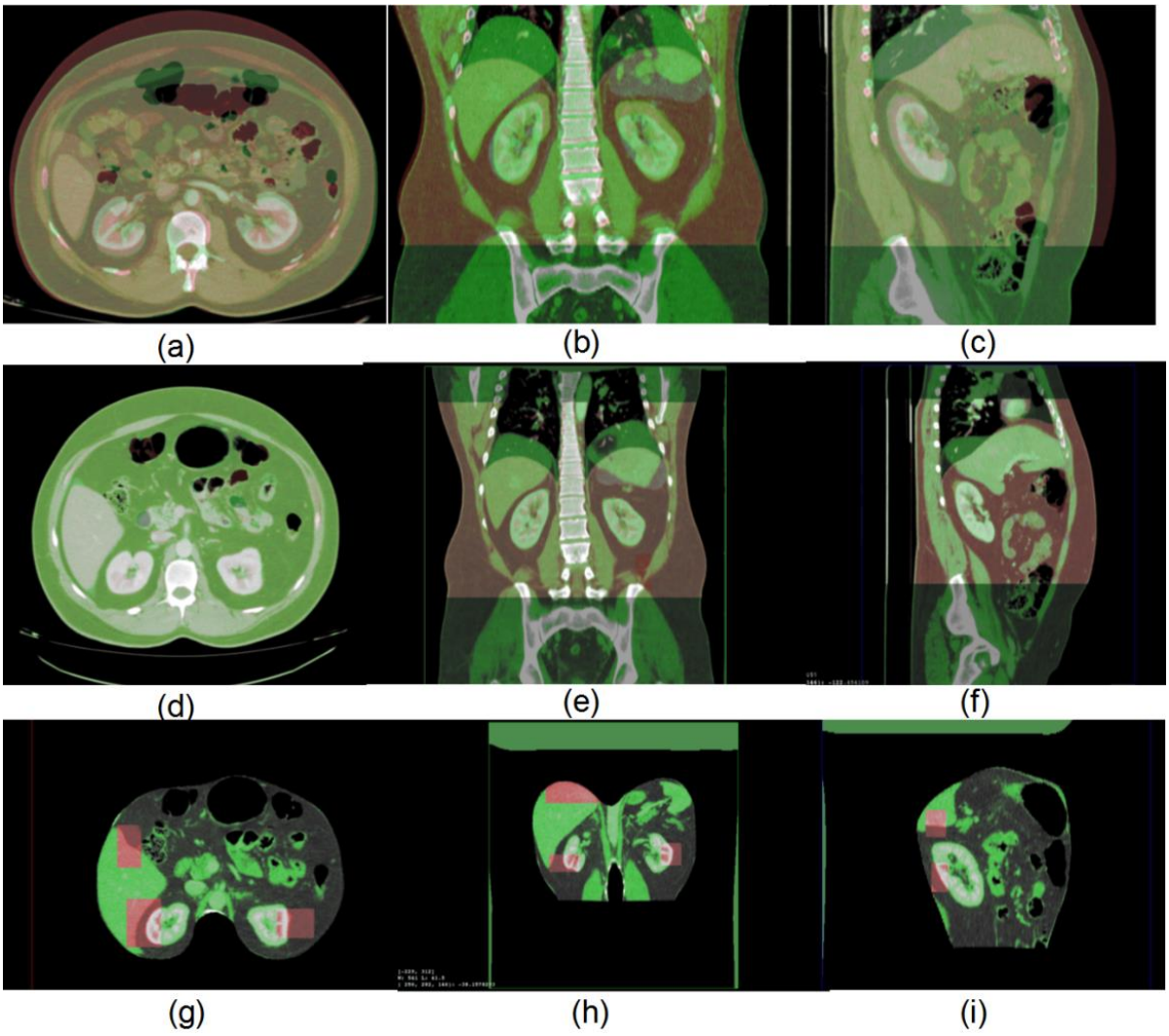

FIGURE 5.4: Registration result comparison with Super Baloo algorithm on one patient. The three rows represent the fused image before registration, registration with AW&TV and registration without AW&TV. The three columns represent the axial, frontal and sagittal view of volume images.

5.3.2 Deformation field analysis

The deformation field of the B-spline+MMI registration with (resp. without) AW&TV is illustrated on one patient data by yellow arrows in FIGURE 5.5(a) (resp. (b)). Each arrow corresponds to its projection in the visualized plane. The target (colored in pink) and source (colored in green) images are superimposed for better understanding of the spatial mapping of corresponding points. The scale factor for both deformation vectors is set to 1 in order to

show the real displacement magnitude of the registration result. Note that we properly selected a sagittal slice index in which the left-right motion was negligible, so that the 3D motion of each voxel can be almost entirely represented by an arrow in the sagittal plane. On this patient case, the registration result with AW&TV is not good, the deformation vector direction and magnitude do not reflect the expected motion of tissues. Only vectors around ribs have consistent direction and magnitude, mainly because they are close to the spine (cf. FIGURE 5.5 (a)). On the contrary, the deformation vector with our proposed approach represents realistic transformation of abdominal viscera regions (cf. FIGURE 5.5(b)). The arrows show the mapping direction and magnitude of each point, the arrow PP' in Fig.5(c) means the point on the liver border of the source image is correctly transformed to the corresponding point on the target image which is also located at the border of liver. It also indicates that the main movement direction of this point is along this vector. We can also see a similar situation such as displacement vector SS' at the border of abdominal viscera (cf. FIGURE 5.5 (d)) and displacement vector KK' at the border of right kidney (cf. FIGURE 5.5 (e)).

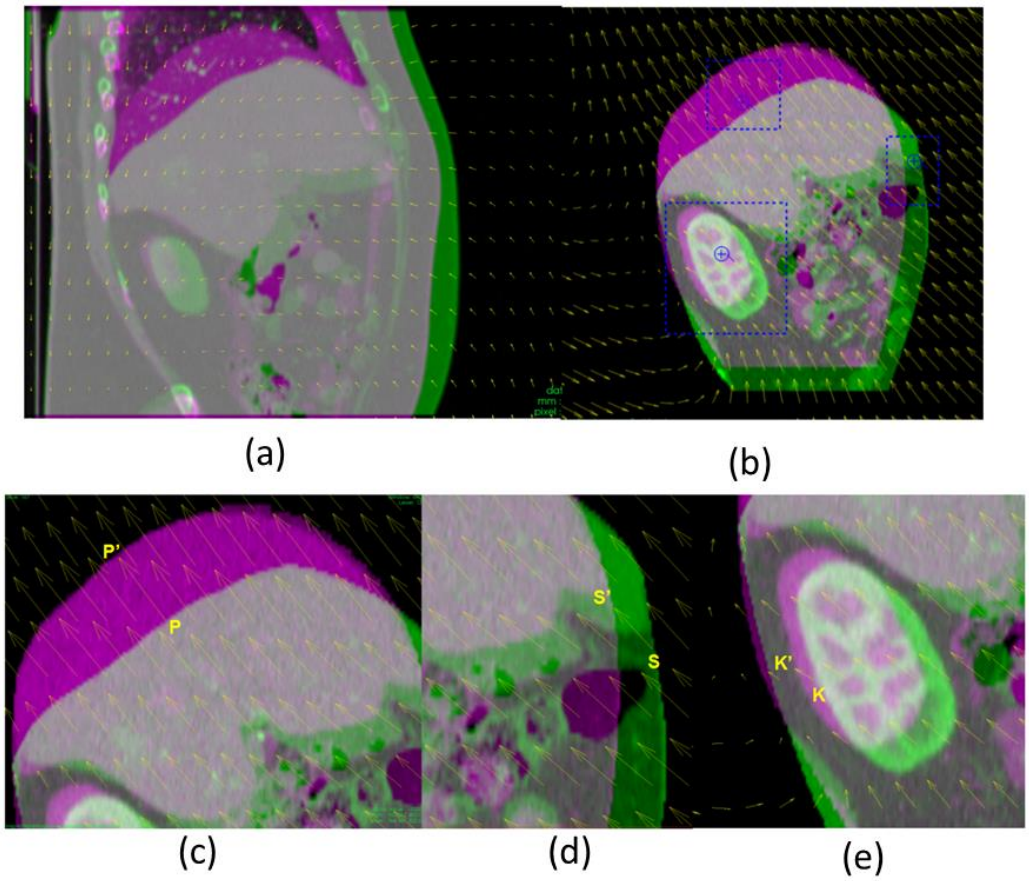

FIGURE 5.5: Illustration of deformation field obtained with B-spline+MMI algorithm applied on the images with AW&TV (a); without AW&TV (b). To better assess the validity of the deformation field with our approach, the three regions in boxes are zoomed in (c), (d), (e).

The same type of results has also been observed on the other nine patients. In the sagittal view, we can also see that there is a big movement of the abdominal viscera along the anterior-posterior direction.

In addition, we projected the 3D deformation field in the frontal view and FIGURE 5.6 shows selected slices from three patient data respectively. The direction of arrows indicates that the abdominal viscera moves not only along the superior-inferior direction, but also along the left-right direction. Thus, based on the analysis of deformation field projected on the sagittal and frontal view, we can see the motion of the abdominal viscera in the left-right and anterior-posterior directions cannot be neglected during the non-rigid registration contrary to the assumption in (Y. Xie et al., 2011).

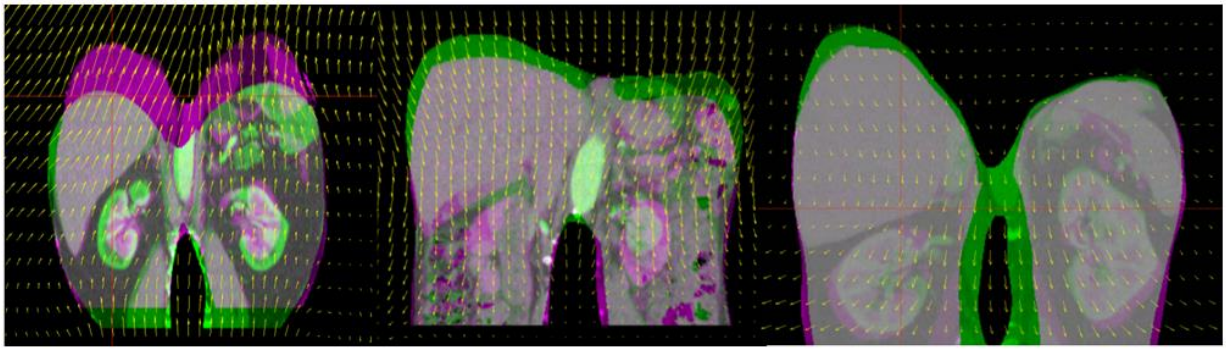

FIGURE 5.6: The visualization of deformation vector is projected in the frontal view (a),(b),(c) from three different patient data, respectively.

5.3.3 Quantitative analysis of registration on four abdominal organs

This section analyzes the quantitative registration error on the surface of the liver, the left/right kidney and the spleen. The two registration algorithms were applied on all images with the same parameters, respectively. The average registration time of the B-spline+MMI algorithm is 300±20 seconds, and 500±25 seconds for the Super Baloo algorithm. A summary of the registration results on *ten* patients is shown in TABLE 5.1 and contains the average surface distance for each organ with its SD and Max, after standard registration with AW&TV, and after registration without AW&TV.

TABLE 5.1: Accuracy results for the B-spline+MMI and Super Baloo registration algorithms of the liver, left/right kidney and spleen.

Liver		BR	BSM with AW&TV	BSM without AW&TV	SB with AW&TV	SB without AW&TV
	Average Distance(mm)	6.7	3.6	1.1	3.3	2.2
	SD(mm)	4.8	3.6	0.3	2.8	2.7
	Max(mm)	15.4	11	1.4	8.6	8.4
Left kidney		BR	BSM AW&TV	BSM without AW&TV	SB with AW&TV	SB without AW&TV
	Average Distance(mm)	3.1	1.5	0.3	1.4	0.7
	SD(mm)	1.8	1.1	0.1	1.0	0.8

	Max(mm)	7	3.4	0.5	3	2.5
Right kidney		BR	BSM AW&TV	BSM without AW&TV	SB with AW&TV	SB without AW&TV
	Average Distance(mm)	2.9	1.2	0.3	1.4	0.8
	SD(mm)	1.8	0.9	0.1	1.3	0.9
	Max(mm)	6.7	2.9	0.5	3.7	2.7
Spleen		BR	BSM AW&TV	BSM without AW&TV	SB AW&TV	SB without AW&TV
	Average Distance(mm)	4.8	3.5	0.5	2.9	1.0
	SD(mm)	3.8	4.4	0.3	2.5	1.1
	Max(mm)	11.5	12.3	1.1	7.4	3

Note: BSM: B-spline+MMI; SB: Super Baloo.

One can see the registration result of B-spline+MMI with AW&TV is sufficient for the left and right kidney with an accuracy below 1.5 (±1.1) mm, but is not good for the liver and spleen which are above 3.5 (±3.6) mm. However, we can see that there is a bigger improvement of the registration result without AW&TV for all four organs, the average distance and SD is below 0.5 (±0.3) mm, only the average distance of the liver is 1.1 mm. The improved SD value also indicates the result between different patients is relatively stable. In addition, the surface mesh distance is also largely reduced with the use of the Super Baloo algorithm (TABLE 5.1). As expected, our approach allows the other algorithm Super Baloo to obtain a better surface distance error.

From FIGURE 5.7, the improvement of the average distance for four organs with different registration algorithms can be inspected in a different way. It then appears that the distance error is reduced by a factor 4 in the case of B-spline+MMI and by a factor 2 in the case of the Super Baloo algorithm.

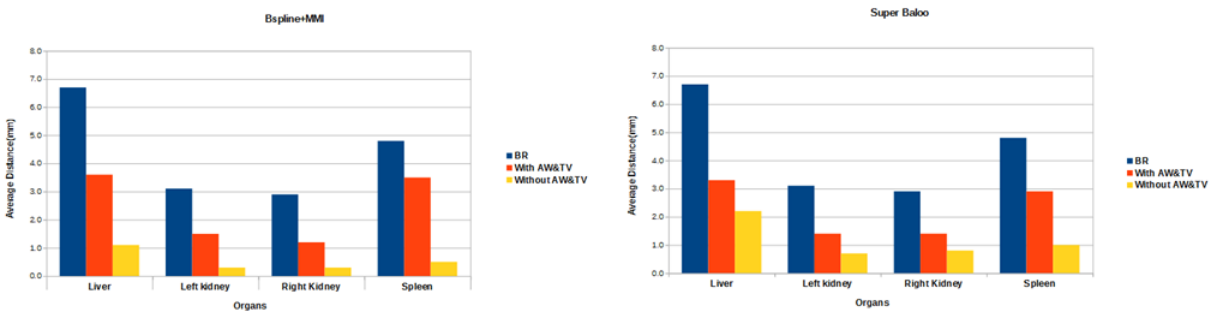

(a) (b)

FIGURE 5.7: The comparison of registration accuracy for four organs with B-spline+MMI(a) and Super Baloo(b) algorithms. The blue bar means the average distance before registration; the orange bar represents the algorithm applied on the images with AW&TV, the yellow bar represents the result without AW&TV.

Finally, the important improvement of our registration approach can be inspected visually on 3D models. FIGURE 5.8 shows the visualization result from one patient case with Bspline+MMI and Super Baloo algorithm, respectively. We can see from the FIGURE 5.8 (a) that there is a large distance between the surface of the transformed mesh from the result with AW&TV and the target mesh (the second column in the FIGURE 5.8(a)). However, this distance has been largely reduced on data without AW&TV (right column in the FIGURE 5.8 (a)). A similar result is obtained with a registration using the Super Baloo algorithm (cf. FIGURE 5.8 (b)).

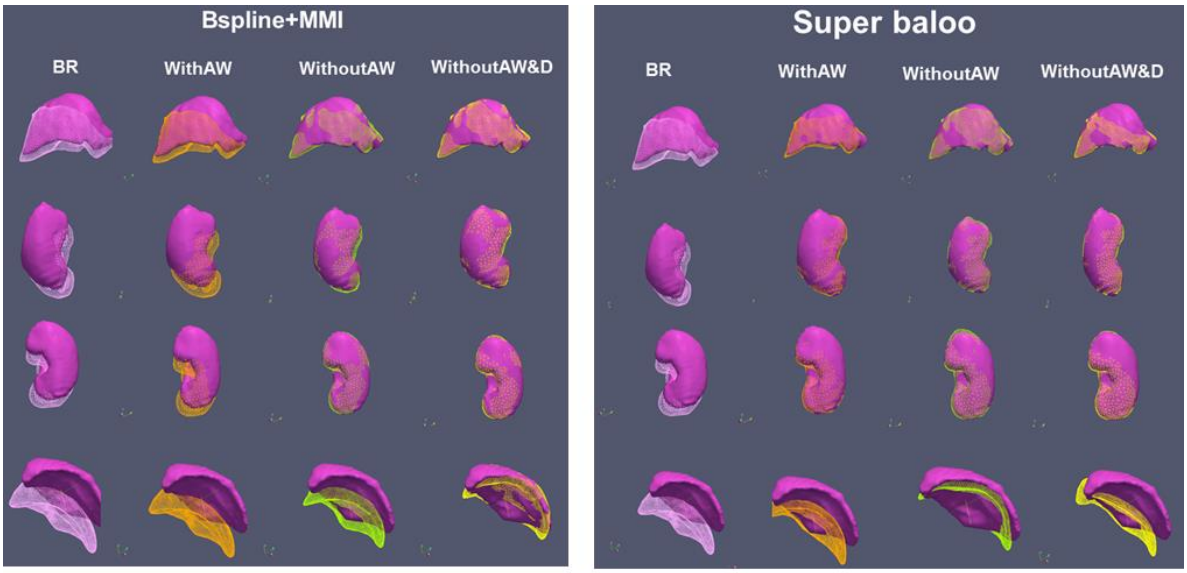

FIGURE 5.8: Visualization of target mesh model and transformed mesh models with different algorithms. At each row of the picture, the mesh model from target image is displayed in surface style with pink color. It is compared with the mesh model from the source image, after standard registration with AW&TV (middle column), and with the mesh model after registration without AW&TV (right column), colored in pink, orange and yellow from left to right. From the first row to the last one the considered organ is liver, left kidney, right kidney, spleen respectively.

5.3.4 Accuracy analysis of abdominal vessels

In addition, another quantitative analysis is performed by calculation of the distance between manually selected vessel bifurcations inside the viscera and outside organs. The average distance before registration for all patients is 11 mm, this value is reduced to 8 mm on the registration results with AW&TV, and finally reduced to around 1 mm on the registration without AW&TV. FIGURE 5.9 shows an example of the comparison of vessel matching with B-spline+MMI algorithm from two patients. The three rows represent the image comparison before registration, after registration with AW&TV, and after registration without AW&TV. The three columns represent the target image, the source image and the superimposition of the result image on the target image. In the first row, one can see that the vessels marked by a red circle in the target image do not appear in the corresponding region in the source image (cf. FIGURE 5.9(a)). Whereas there is no significant improvement after the registration with AW&TV (cf. FIGURE 5.9(a)), one can see that the corresponding vessels are matched very

well after the registration without AW&TV (yellow circle). To better assess the comparison between both registration results we superimposed the registered image on the target image, allowing to see that the motion has been well compensated with our approach. Similar conclusion can be obtained from inspection of the second patient data (cf. FIGURE 5.9 (b)).

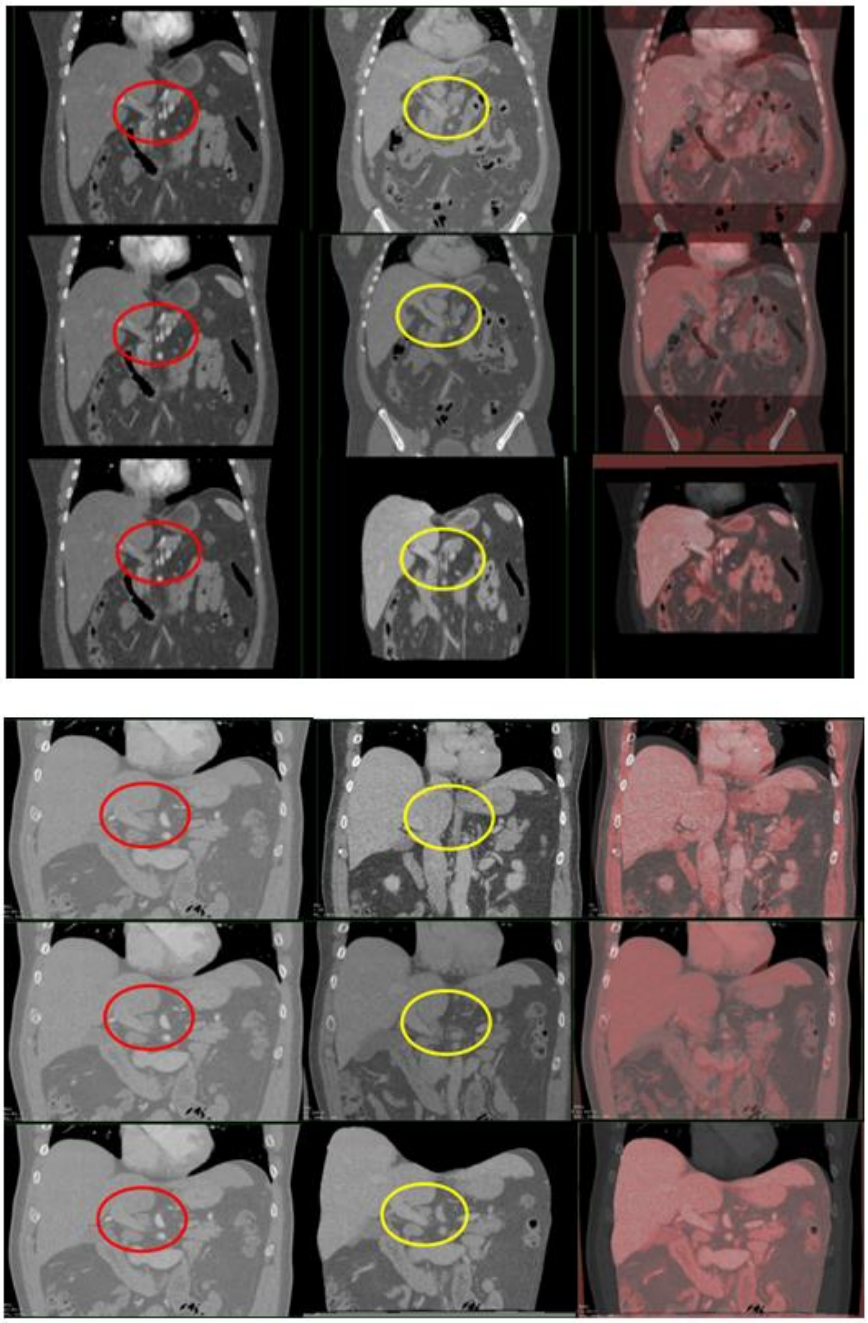

FIGURE 5.9: Comparison of abdominal vessels with Bspline+MMI registration algorithm on two patients. The vessel region of interest is highlighted in red (resp. yellow) in target (resp. source) image. The first row is before registration, the second row is the result after registration with AW&TV and the third row is the result after registration without AW&TV. The

three columns represent the target image, source image and the superimposition of the registered image on target image.

5.4 Discussion and conclusion

In this chapter we have proposed a simple yet efficient approach to accurately register abdominal viscera in multi-phase CT images from a priori knowledge of the AW and the diaphragm. Indeed, we have basically chosen to remove from both source and target images the anatomical structures outside prior segmented envelops and to replace it by a constant value. In order to show that this solution does not depend on the registration method, we have tested it using two state of the art algorithms: MMI + B-splines and Super Baloo. Experiments on 10 patients have demonstrated that both registration algorithms obtain a much better accuracy using our approach, since it reduces the registration error on average from 2-3 mm to 1 mm or less. Our experiments also indicated that removing the thoracic viscera from the source and target images is not always necessary, particularly when the breathing motion is not significant. However, further tests are still necessary to clearly quantify when thoracic viscera should be removed to ensure the registration accuracy. Since this error mainly comes from the inconsistent motion between the lungs (which expand) and the liver (which slides on the diaphragm), a basic analysis of the lung deformation may be sufficient to decide when the thoracic viscera should be delineated.

We would like to highlight that our registration can be helpful for a vessel segmentation task. Indeed, arteries are usually easy to recognize in arterial phase CT scans due to their very high intensity whereas veins are almost invisible. On the contrary, veins are visible in the venous phase but since arteries are also visible with a similar intensity value (due to the remaining contrast agent in the arteries), it is not possible to separate them. Using the registration of the arterial phase image on the venous phase one, it should be much easier to automatically extract the veins positions during the venous phase.

To conclude, since it clearly appears that the knowledge of the AW position provides crucial information for many applications (registration, visualization, segmentation), we believe it is worth trying to find an algorithm that automatically (or nearly automatically) delineates it in CT images. In the next chapter, we will propose an alternative analysis of this problem and provide some prospective results

.

Chapter 6 Automatic segmentation of AW: preliminary results

We have shown in the previous chapter that the removal of the AW in the multiphase CT images had a great influence on the registration accuracy. Although we already provided in Chapter 3 two efficient tools for fast delineation of the AW and TV, it is clear that it would be better to avoid such step and provide it automatically. We have already analyzed in Chapter 3 the literature regarding the automatic segmentation of the AW and results were not sufficiently convincing, which is not surprising due to the challenging properties of abdomen CT image. Most of work relied essentially on local gradient based approach in addition (or not) to some elastic constraint on the general segmentation shape.

In this chapter, we propose a first step toward automatic segmentation of abdominal wall based on the spatial a priori knowledge of muscle border and ribs. We firstly analyze the features of CT image and propose our strategy to perform the segmentation in a selected stack of consecutive 2D frontal views, and treat the abdominal wall separately in left and right part. Secondly, we explain how we automatically extract spatial a priori knowledge which includes lung mask, muscle border and rib mask using morphological operators.

Then, we explain how we provide an initialization of the abdominal wall segmentation from muscle in the AW and how we refine it using gradient information. Finally, an initial result of this automatic segmentation approach on 3 patient data is presented and shows that our approach is promising even if many improvements are necessary to reach a sufficient accuracy.

6.1 Image analysis

Since the thoracic wall is distinctive in CT image and easy to segment (cf. FIGURE 6.2), we focus on the segmentation of abdominal wall in this chapter.

We have reviewed in section 4.1 that there has been several work related to segmentation on abdominal wall in the axial or sagittal view, but the result is not accurate enough. The complex shape of abdominal wall in axial view makes it difficult to be segmented automatically. The automatic segmentation work on sagittal view has also been investigated by Vandemeulebroucke et al., 2012, they obtain the thoracic wall edge based on level set algorithm, whilst it converges to the skin edge in the upper abdomen area.

We here show three views of CT images from three patient and five slices are extracted in each view (FIGURE 6.1). We can see the AW has circular shape in the axial view and multiple contacts with liver, spleen and colon. In such cases, it is very difficult to distinguish the border of AW, except in the region below the liver. In sagittal view, the anterior shape of the lung can help extrapolate the AW anterior border, however this strategy holds only in the sagittal slices which do not contain the heart and psoas muscle

In the frontal views, the left and right frontiers of AW seem easy to identify, though there are vague regions where AW is connected to abdominal organs. Typically, the shape of ribs can be extracted to extrapolate the AW segmentation. The psoas close to the spine and can be identified based on their position with respect to the spine.

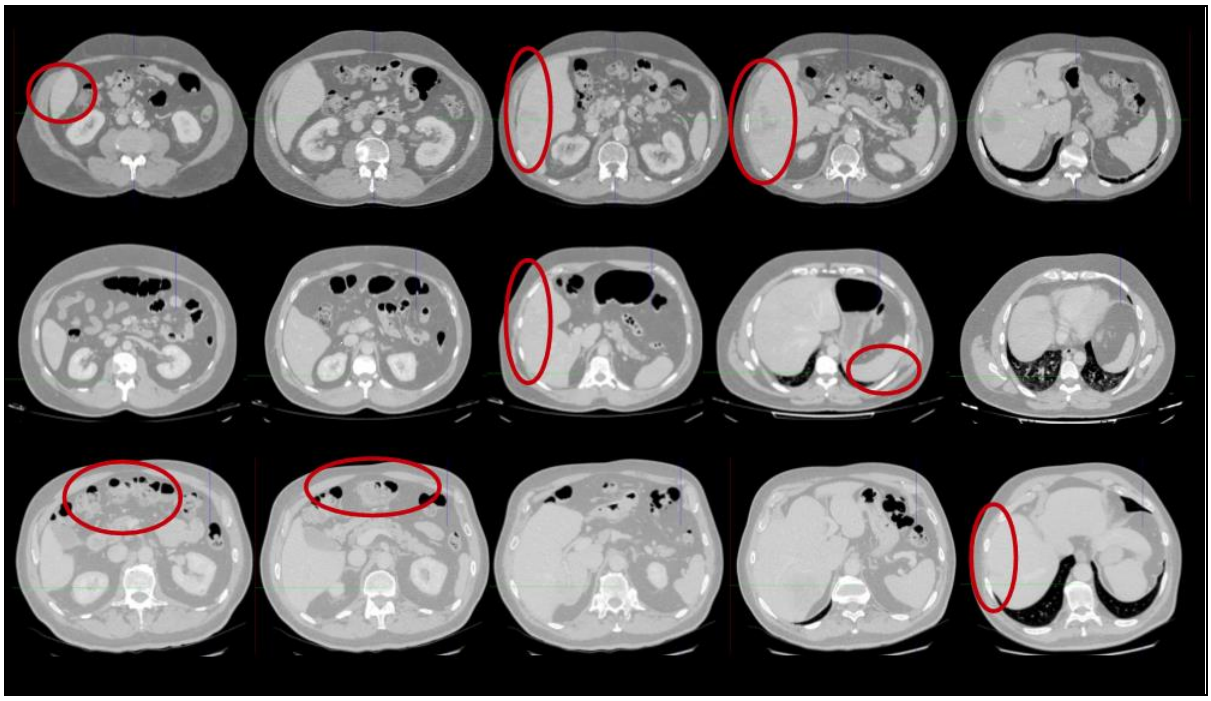

(a)

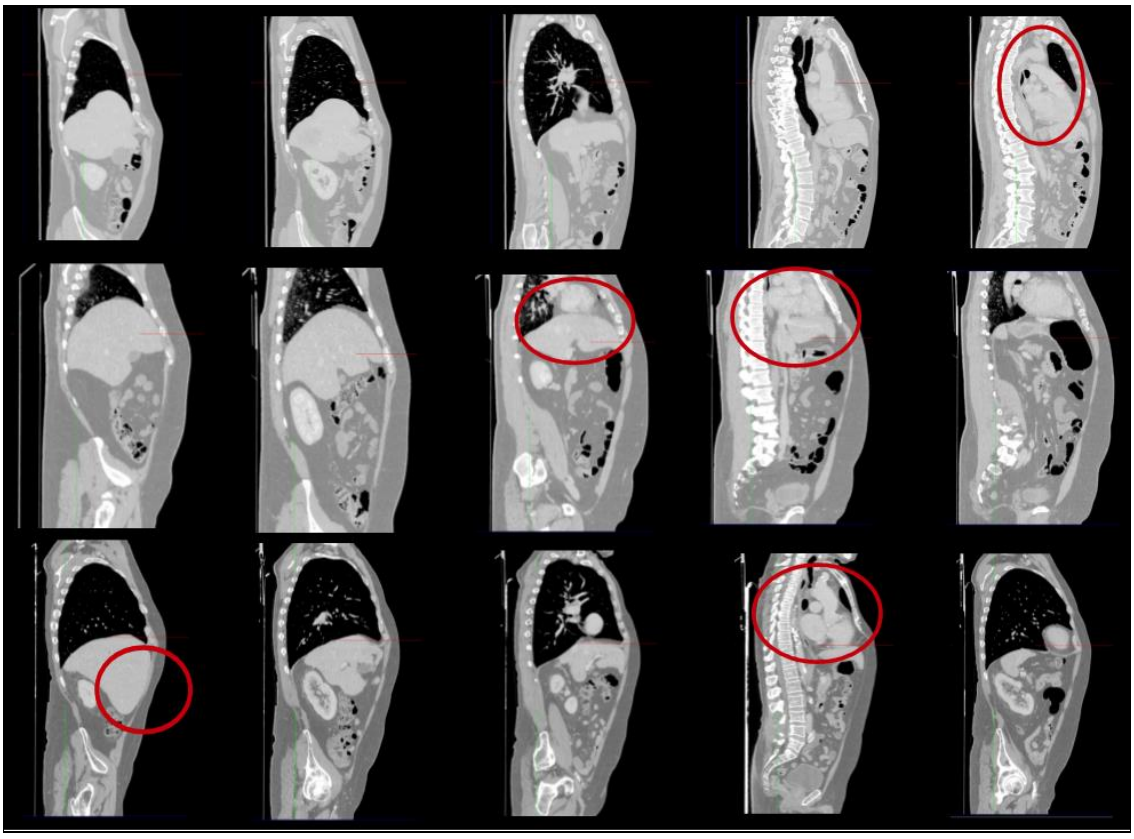

(b)

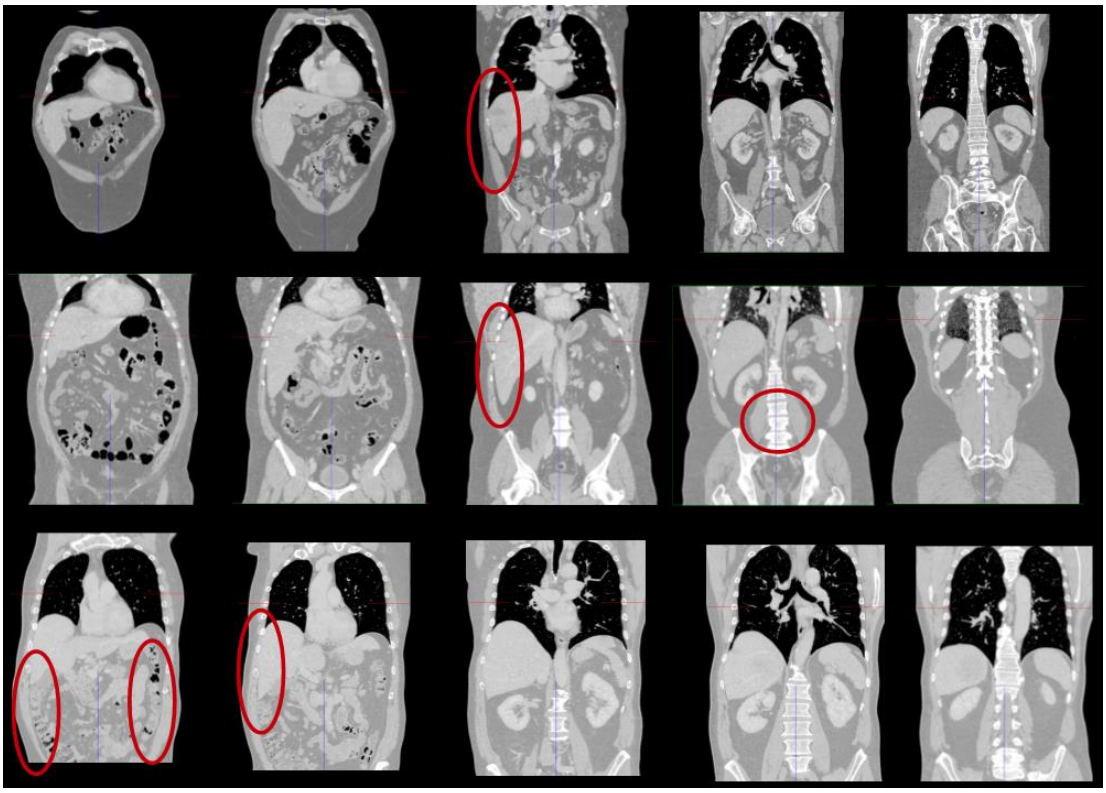

(c)

FIGURE 6.1. Image analysis of three views from three patients. (a) axial view (b) sagittal view (c) frontal view. In each view, each row represents the image from one patient and five slices are extracted to show the features of AW. We highlight in red typical region are difficult to extract.

Furthermore, in Chapter 4, we have seen that the curvature of abdominal wall is low and its shape varies smoothly along the cranio-caudal direction. The AW muscle (marked in blue in FIGURE 6.2) also has similar curvature and a distinctive intensity value with respect to the surrounding fat tissue. Therefore, we propose a new strategy with use of this spatial knowledge to automatically delineate the AW in the frontal views.

The AW segmentation is processed in left and right separately. Using the right AW segmentation as example, the details of our strategy is as follows. The bottom point of right lung closing the AW is used as a first control point (orange point in FIGURE 6.2). The distance along x axis between this point and the muscle border can be calculated. Then a second control point is obtained below the ribs closing the AW from the shape of the muscle border. Based on the similar shape between the AW and AW muscle border, an initial estimation of AW can

be obtained (cf. FIGURE 6.2). Finally, it will be refined based on gradient information along the X axial direction.

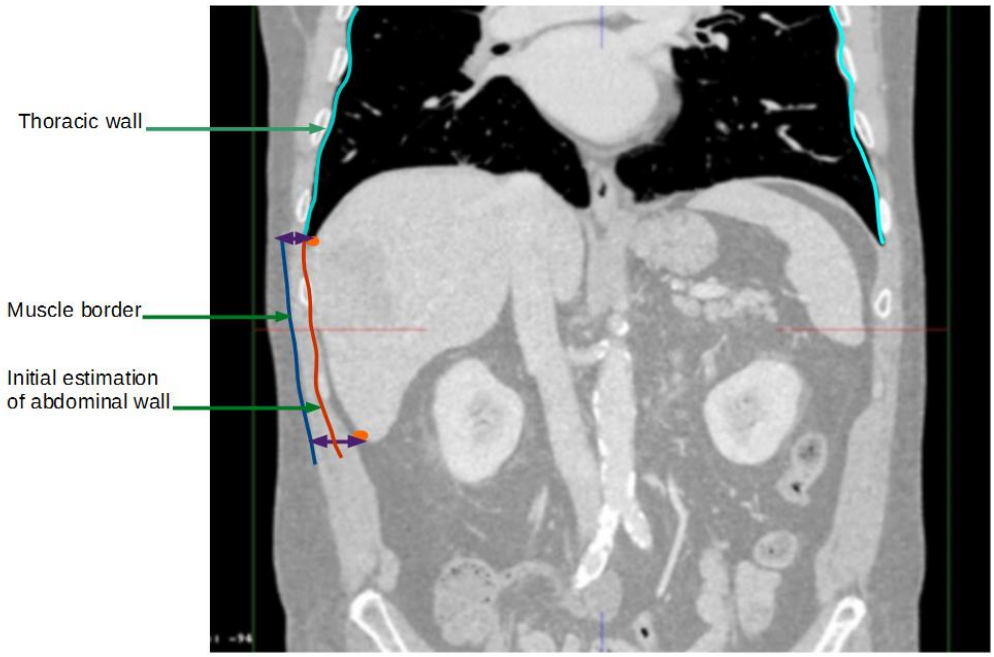

FIGURE 6.2: Illustration of the segmentation strategy of the abdominal wall in 2D frontal view. The place of muscle border is marked by a blue curve.

6.2 Method overview and a priori data extraction

6.2.1 Overview of strategy

The flow chart of our strategy is summarized in the FIGURE 6.3. Firstly, the following images are generated: lung mask image, the muscle border mask image by removing the fat tissue and skin and rib mask image without spine and pelvis. Then, the first and second control points are extracted based on previous generated images. The rib information is also used to select the region of segmentation in the frontal view. The initial border of abdominal wall is generated based on the distance between both control points and the muscle border. Finally, the refinement of the initial border of the abdominal wall is carried out using the gradient information between the abdominal wall and the abdominal viscera.

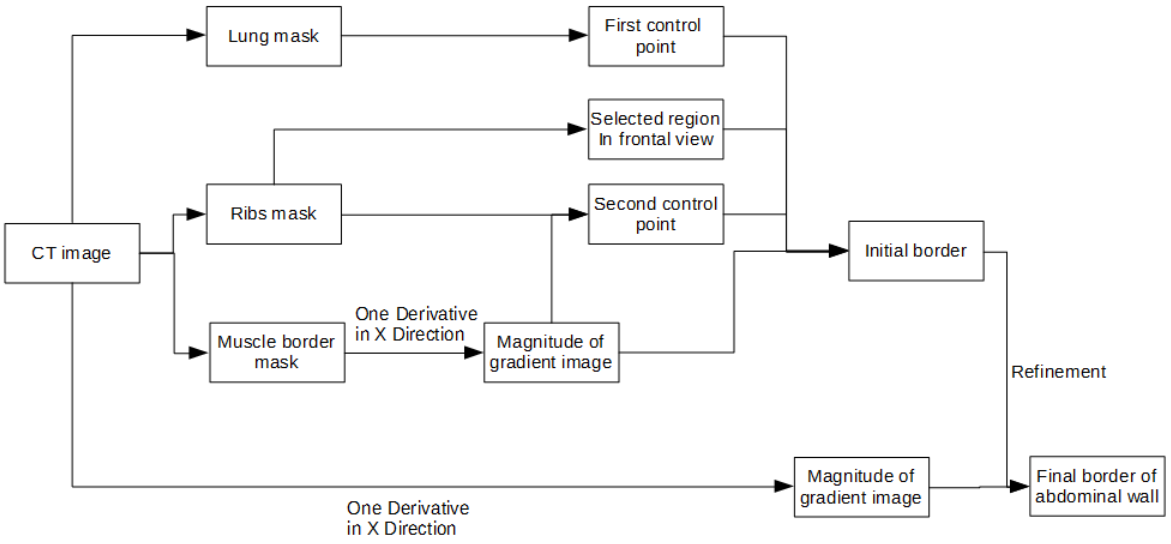

FIGURE 6.3: Flow chart of our strategy.

6.2.2 Generation of lung mask

There are already many efficient and automatic approaches for the segmentation of lung, which are based on pixel information (Kalender et al., 1991;S. Hu et al., 2001). Here, we propose an automatic segmentation method for the lung using a standard sequence of morphological operations. The detail of our approach for extracting lung mask is as follows. In the CT image, the intensity value of air is approximately -1000 Hounsfield units (HU), the lung is in the range of -900 HU to -400 HU, and the chest wall, ribs, fat tissues, muscles are bigger than -400 HU (Brown et al., 1997 ; M.-T. Wu et al., 1994).

Therefore, a 3D binary threshold operation with the range parameter [-950, -450] is firstly performed to roughly obtain the lung region (cf. FIGURE 6.4(b)). After this operation, there are still some voxels, such as noise or the outer skin layer remaining in the image. Therefore, we extract the largest region using a 3D labeling technique, which removes unconnected voxels (cf. FIGURE 6.4 (c)). Then, a 2D labeling technique is carried out to obtain two largest regions in each frontal view slice (cf. FIGURE 6.4 (d)). The opening and closing operators with 3*3 element size are performed to remove some remaining tissues such as trachea and bronchi in the image. Since the first threshold step will also lead to some holes in the mask due to some tissue within the lung, a median operation with 3*3 element size and hole filling filter are subsequently applied. The final lung mask is generated (cf. FIGURE 6.4(e)).

(a) (b) (c) (d) (e)

FIGURE 6.4: The generation process of lung mask. (a) Original CT image (b) Threshold operation (c) 3D labeling (d) 2D labeling on frontal view (e) Final lung mask after hole filing filter

6.2.3 The segmentation of muscle border

The outer layers of abdominal muscle are the fat tissue and the skin with varying thickness in different slices (marked by pink ellipse in FIGURE 6.5(a)). Since the intensity value distribution of fat tissue is between [-200, -50], a threshold operation with range parameter [-1024, -50] is applied. To remove the remaining skin (cf. FIGURE 6.5(b)), a morphological OPENING operation with element size 3*3*3 is performed, followed by a CLOSING operation with same element size to close the possible holes caused by the previous OPENING step. The mask image without the fat tissue is obtained after using the MEDIAN operator for removing some noise in the entire volume image (cf. FIGURE 6.5(c)). Finally, the magnitude of the gradient of this mask image in x direction (MGX) is calculated by a 3*3 convolution with the first derivative of a Gaussian (cf. FIGURE 6.5(d)). The image of signed edge will be used in Sec. 6.3.2 for control points extraction.

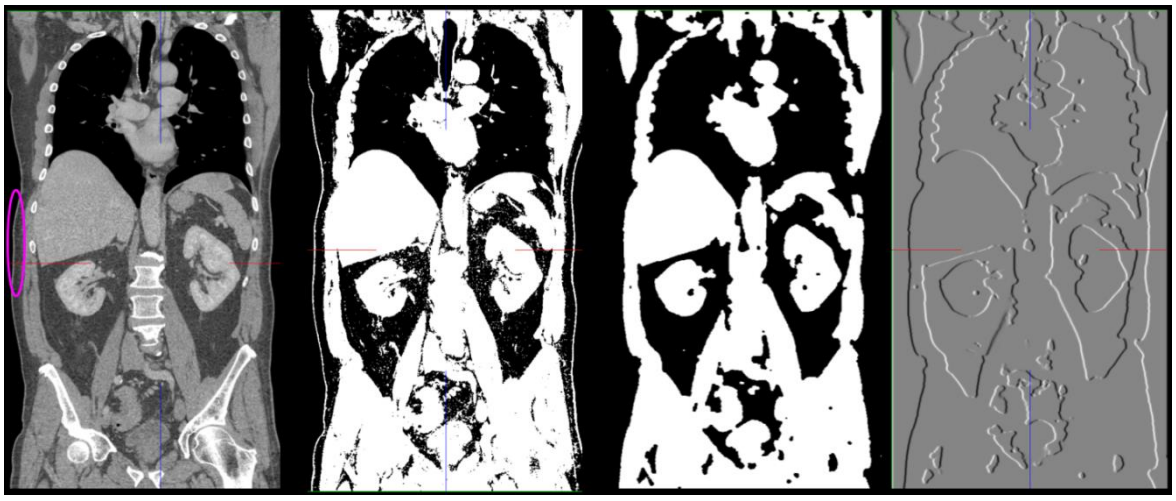

(a) (b) (c) (d)

FIGURE 6.5: The segmentation of muscle border. (a) Original CT image in frontal view; (b) new image after the fat tissue removing;(c)New mask image without fat tissue and skin; (d) Magnitude image of the gradient in x direction.

6.2.4 The segmentation of ribs

There are 12 pairs of ribs in the human body, and 8-10 pairs are usually visible in the CT image depending on the acquisition protocol (Shen et al., 2004). One end of them connects with the spine, while upper ribs also connect with the sternum at the anterior end. The CT value of the bone ranges from 250 HU to 1000 HU which is bigger than the value of most surrounding organs or tissues. They enclose the whole thoracic viscera and part of upper abdomen viscera. They are located symmetrically with a stable ellipse shape in the 2D frontal views. These anatomical features can facilitate their labeling in CT image. There are much work on the segmentation of bones, which includes ribs, spine and sternum (D. Kim et al., 2002;Banik et al., 2010;Yao et al., 2006;Klinder et al., 2007;Kang et al., 2003), however, there are few about rib segmentation only with the purpose of using them as feature points (Staal et al., 2007; L. Zhang et al., 2012;Shen et al., 2004).

Our approach contains main ideas from the work of (L. Zhang et al., 2012; Shen et al., 2004). The segmentation algorithm mainly includes three steps. Firstly, bones are extracted from an original grey level CT image, the result contains all ribs, spine and pelvis. Secondly, a special template slice in a frontal view is selected, which intersects almost all ribs, but does not contain the spine and sternum regions, and the centroid of each rib can be obtained. Finally, a recursive extraction based on the template slice along Y direction is used to extract all ribs independently. The details are described below:

-Step1: **extraction of bones**

The bones are roughly extracted using a threshold operation with the range of [200 HU, 1000HU] (cf. FIGURE 6.6(a)). In the CT image, an elliptic rib may be split into several regions due to the noise and partial volume effect. Taking the rib size, shape and position into account, we designed four rules to solve above issues.

Rules 1: A morphological closing operation with a structure element (SE) of 2 pixels radius is performed to merge small closing regions and fill holes, which should be originally belonged to one rib.

Rule 2: The largest 3D region is selected by using the LABELING operation.

Rule 3: Size constraint is employed to exclude most of the non-rib regions. The size range of the rib is set between 10 and 450 pixels in 2D frontal view.

Rules 4: Ribs should be close to the leftmost or rightmost boundary of the lung, the x axial distance should be smaller than 25 pixels.

Using the *Rule 1*, one connected component per rib is obtained (cf. FIGURE 6.6(a)) and the bone mask which contains ribs, spine and pelvis are finally extracted with use of *Rule 2* (cf. FIGURE 6.6(b)).

-Step2: extraction of seed points of ribs in a template slice

After the generation of the bone mask image, the next step is to remove the spine, sternum and pelvis. We firstly select a frontal slice which intersects almost all ribs but does not contain the spine and sternum. We call this slice a template slice, which requires a priori information of the anatomy. The choice of this slice index is patient specific and is usually around the middle slice in frontal view. However, there are still pelvis and other objects which are not region of interest in the template slice (cf. FIGURE 6.6(c)). The extraction of ribs in this template slice is illustrated in FIGURE 7.

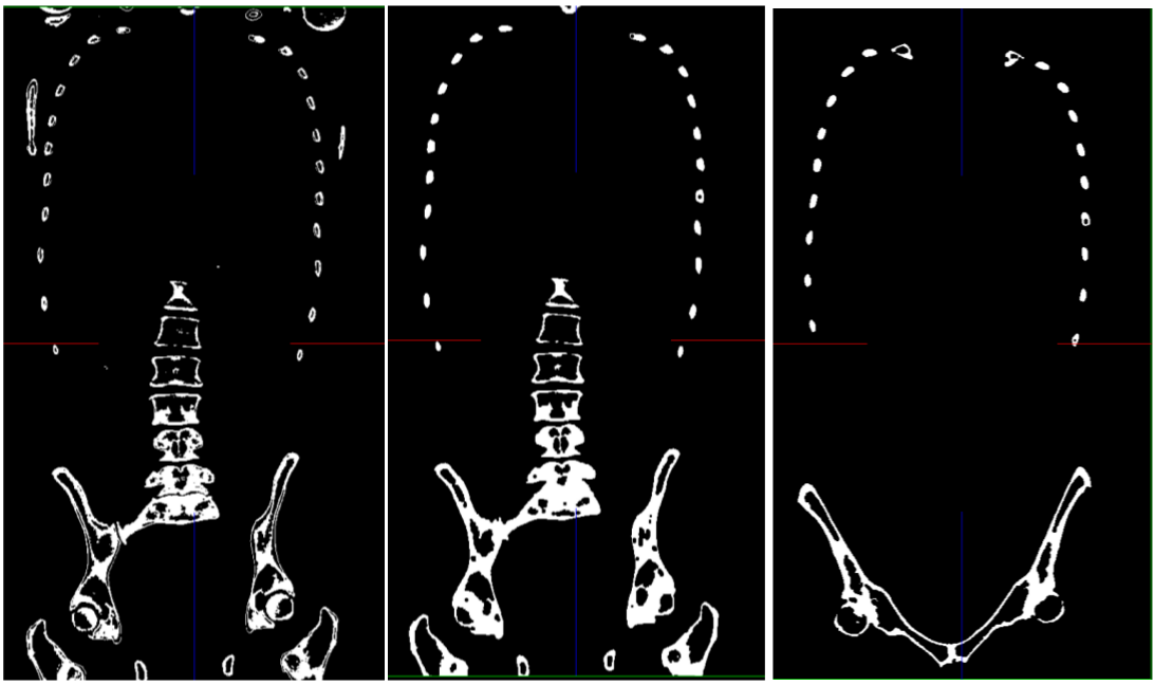

(a) (b) (c)

FIGURE 6.6: Illustration of the bone extraction using morphological filter.

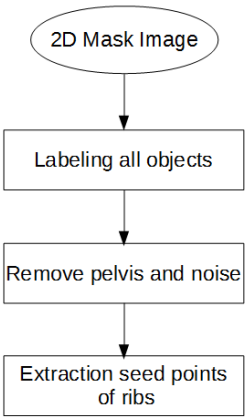

FIGURE 6.7: The diagram of rib extraction in the template slice

Firstly, a 2D labelling operator is applied to separate all individual objects in the template slice. The geometric information of all labeled objects, including size, label ID, centroid and bounding box is obtained. Since the pelvis is located at the bottom of the image, a good solution for removing it is to use the Rules 4 we have defined before.

In addition, the *Rule 3* is applied to remove outlier objects which size is smaller than 10 pixels or bigger than 450 pixels. Finally, all ribs in this template slice (9-11 pairs) are extracted, and the coordinate of centroid of each rib is stored in a vector.

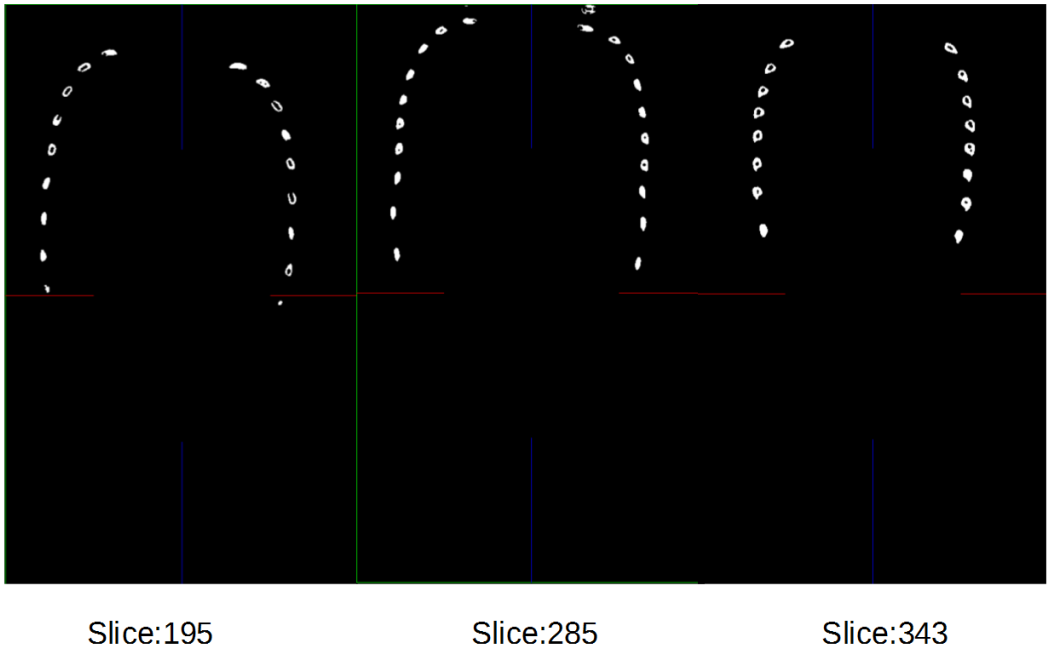

FIGURE 6.8: Example of rib extraction in several frontal slices of a same patient.

Step 3: recursive propagation

Once all ribs have been obtained in the template slice, a recursive propagation of the ribs from the template slice along anterior (to 1st slice) and posterior direction (to Ymax slice) will be performed. Ymax represents the index of maximum number slice in frontal view. This propagation scheme is illustrated in the FIGURE 6.9.

More precisely, the centroid of each rib from template slice is employed as an initialization to search the closest connected component in both next anterior and posterior frontal slice. The search region is a rectangle of 20*20 pixels. The centroid information of the found components is stored and used to initialize the search in the next slice. This process is iteratively carried out until all slices in anterior and posterior directions are processed.

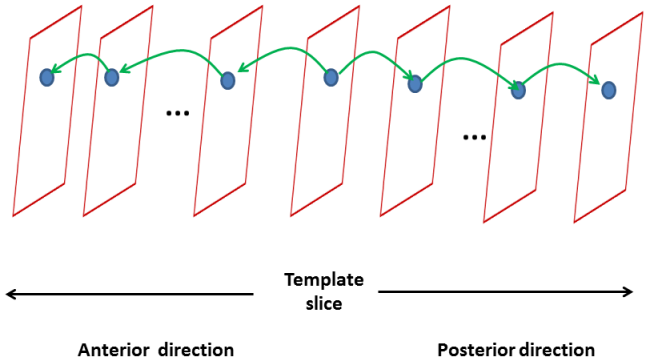

FIGURE 6.9: Illustration of the mechanism of rib extraction. The recursive propagation starts from the template slice and goes toward anterior and posterior directions.

6.3 Segmentation of the AW

The generation of the initial border is based on the anatomy shape of AW muscle border. The left and right regions of a frontal slice are processed separately. In each region, we propose to generate two control points close to the AW. The first control point, is the bottom point of right (resp. left) lung, attached to the right (resp. left) abdominal wall, and is represented by CP_{RF} (resp. CP_{LF}). The second one (CP_{RS}) is attached to the AW but located below the liver. The second point in the left region (CP_{LS}) will be computed from the position of CP_{RS}. Finally, the initial right (resp. left) border of AW is generated from the AW muscle shape between the height of both control points CP_{RF} and CP_{RS} (resp. CP_{LF} and CP_{LS}), and is refined using gradient magnitude.

6.3.1 Search of the first control points C_{RF} and C_{LF}

The left bottom point of the right lung (resp. right bottom point of the left lung) is chosen as the CP_{RF} (green circle in the FIGURE 6.10(a)). The algorithm to compute the CP_{RF} coordinate is as follows (this flow chart can be seen in FIGURE 6.10(b)). In the lung mask image, we start at the top-left corner of the image and scan each vertical line from top to bottom and from left to right. The scanning stops once it reaches a pixel which value is 255 (point P in the FIGURE 6.10(a)). Then, we begin to search along the border of the right lung until it reaches its bottom (marked by a green circle on the right lung in the FIGURE 6.10(a)). The searching approach for CP_{LF} is similar and symmetrical.

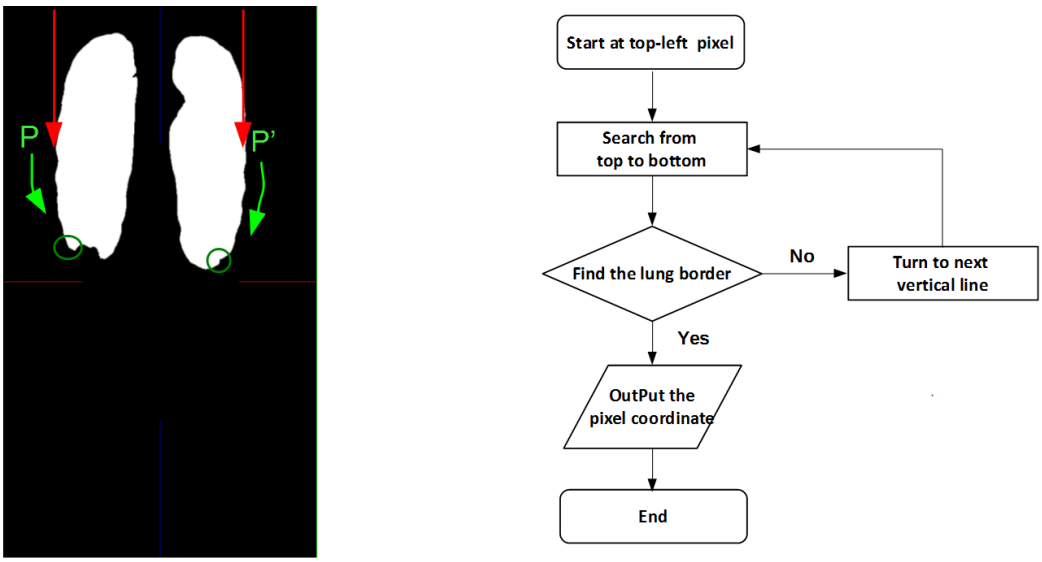

(a) (b)

FIGURE 6.10: (a) Illustration of the searching of C_{RF} and C_{LF} (b) Flow chart of the algorithm to find of C_{RF} and C_{LF}.

6.3.2 Search of second control points CP_{RS} and CP_{LS}

The second control point (CP_{RS} and CP_{LS}) is searched in the MGX image (cf. FIGURE 6.11(a)) generated at the previous step (cf. Section 6.2.3). The search process of CP_{RS} in the right AW is illustrated in FIGURE 6.11(b). Firstly, we choose the lowest point of rib as a starting point (point P_R in FIGURE 6.11(b)). Then we search toward the left in the MGX image to find the border of AW muscle. The threshold value of the border should be smaller than -5. Once we reach the border, then we change the search direction toward down along the border of AW muscle (red arrow in FIGURE 6.11(b)). For each point of the border, we check toward right if there is a pixel with a high gradient value (bigger than 5). The search extent of 30 mm is based on our prior knowledge about the width of the AW muscle. We continue along the border until this point is found. This point is the second control point CP_{RS} (cf. FIGURE 6.11(b)).The flow chart of this search process is illustrated in FIGURE 6.12. CP_{LS} is the symmetrical point to CP_{RS} on the AW and has the same Z coordinate (cf. FIGURE 6.11(b)).

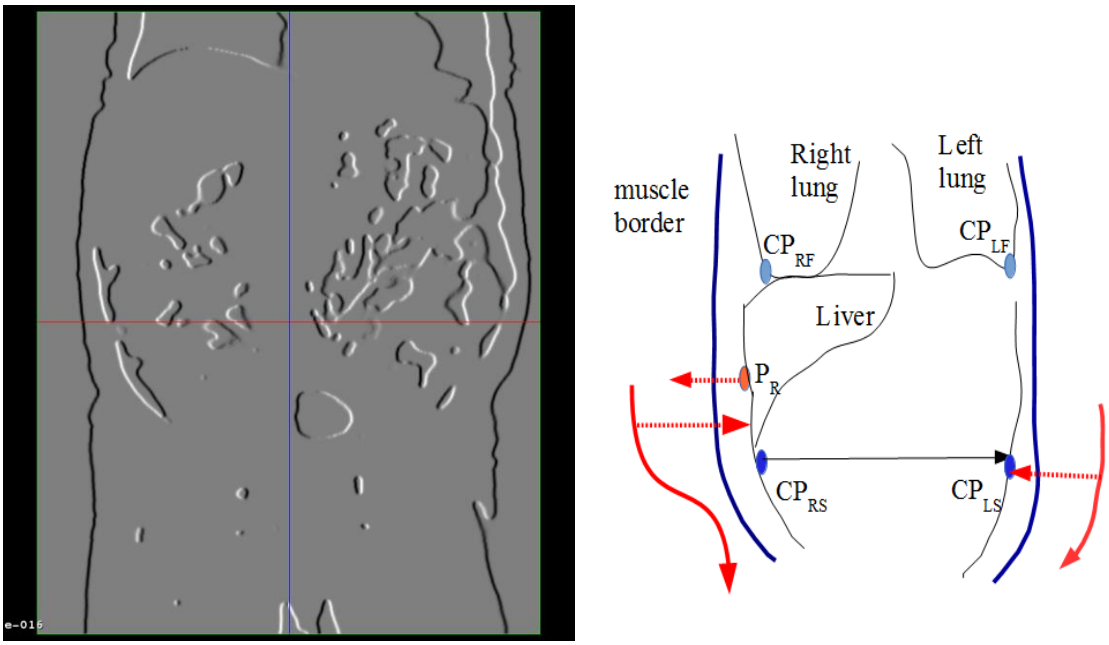

(a) (b)

FIGURE 6.11: (a) The MGX image generated from mask image without fat tissue; (b) Illustration of the process to define CP_{RS} and CP_{LS}. The point P_R is the lowest centroid of ribs. CP_{RS} and CP_{RF} are illustrated in FIGURE 6.13).

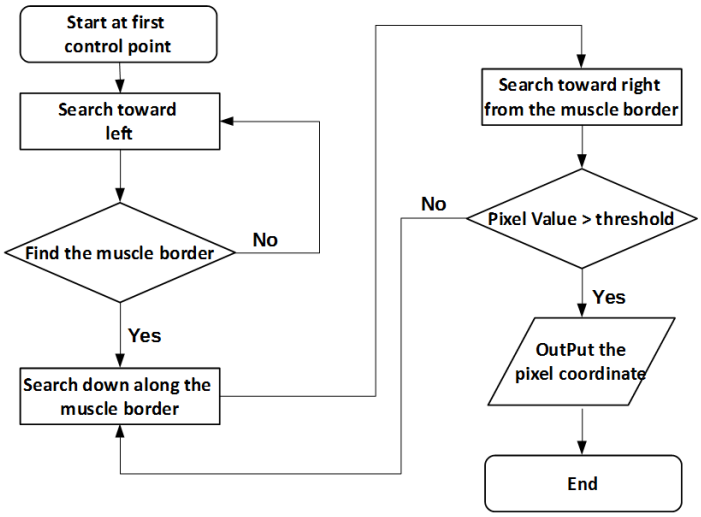

FIGURE 6.12: The flow chart of CP_{RS} and CP_{LS} localization in the MGX image

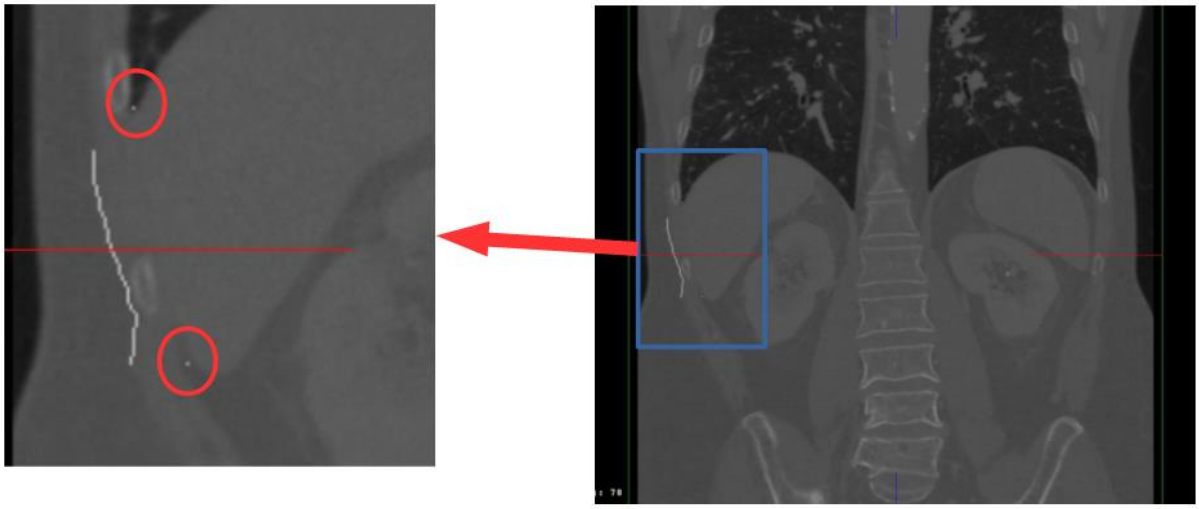

FIGURE 6.13: Illustration of two control points in the AW region. To better show the points, the region in the blue rectangle is enlarged. CP_{RS} and CP_{RF} are highlighted in the red circles.

6.3.3 Generation of the initial border of the AW

The generation mechanism of the initial border of the right AW can be illustrated in the FIGURE 6.14.

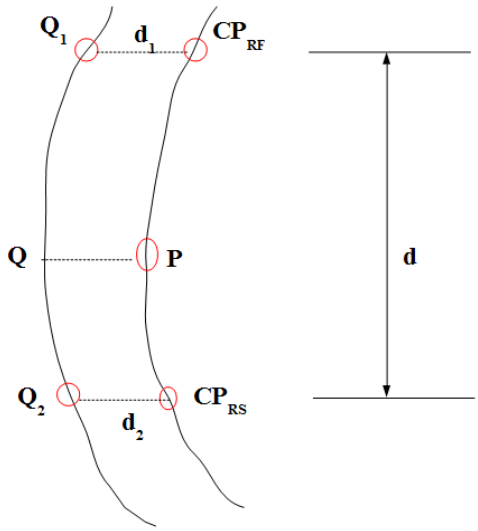

FIGURE 6.14: The mechanism of the initial AW border generation. Q_1Q_2 represents the muscle border. CP_{RS} and CP_{LS} are the control points.

We firstly compute vertical distance $d_{vertical}$ between CP_{RS} and CP_{RF} ($d_{vertical} = CP_{RS}(z) - CP_{RF}(z)$). Let Q be one point of Q_1Q_2, its corresponding point P on the AW is located on the right of Q at the distance:

$$d(P,Q) = \alpha * d_2 + (1-\alpha) * d_1 \qquad (6.1)$$

where $\alpha = \frac{p(z)-p_2(z)}{d_{vertical}}$, d_1, d_2 represents the distance of point CP_{RS} and CP_{RF} to the AW muscle border, respectively.

The AW muscle border and the generated initial border of the right abdominal wall can be seen in the FIGURE 6.15.The initial border of the left abdominal wall is obtained with a similar approach using CP_{LF} and CP_{LS}.

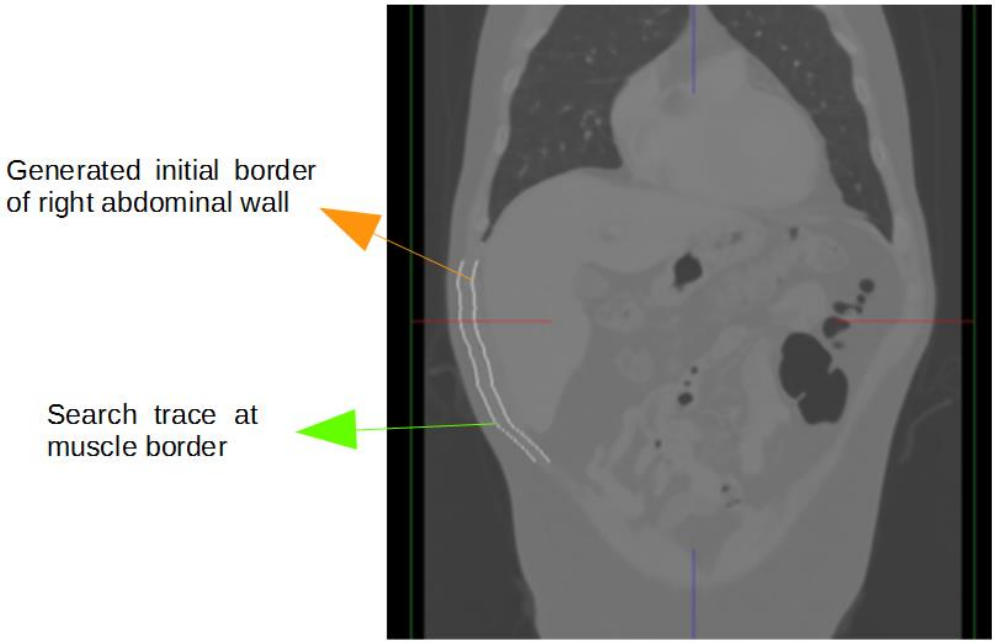

FIGURE 6.15:The generated initial border of right abdominal wall is completed from the AW muscle border.

6.3.4 Refinement of the segmentation

The generation of the initial border is based on the assumption that the AW and the AW muscle border are parallel. However, the width of the abdominal wall is usually bigger than the parameter $d_1$or d_2. The initial generated border is thus usually located inside the true AWl (cf. FIGURE 6.15). A further step is required to refine the border to the actual position of AW.

Our refinement strategy is to search the edge of the AW at the right side of the initial border (cf. FIGURE 6.16(a)). The refinement is performed using the gradient magnitude in the x axial direction of original CT image (cf. FIGURE 6.16 (b)). Given each point of the initial bor-

der, we search toward right to find the pixel with the highest gradient in a limited distance range. There are three types of pixel that can be found: (1) edge of a rib (2) edge of the AW (3) not the expected pixel. For the first and second type pixels, we can directly employ them as border of abdominal wall. For the third type pixel, we abandon it. The points at such position can be obtained using interpolation technique from neighbor frontal slices. Finally, the result of our approach has been applied on three patient CT images (cf. FIGURE 6.17).

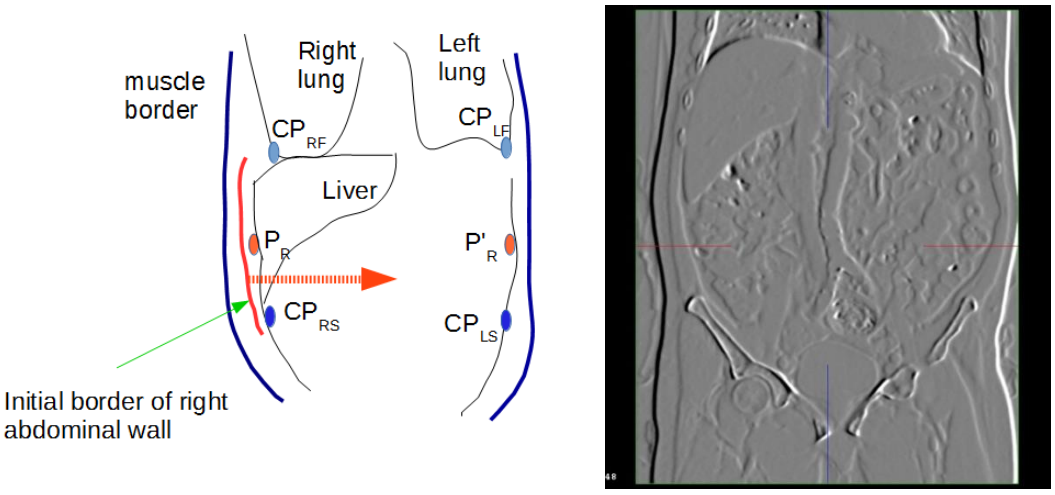

(a) (b)

FIGURE 6.16: Illustration of the refinement step. (a) Illustration of the position of the initial border; (b) The magnitude of gradient in x direction of the original CT image

6.4 Discussion and conclusion

In this chapter, we have developed an automatic algorithm for the AW segmentation in a specific stack of frontal slices, using a priori knowledge of lung, ribs and muscle of abdominal wall. We believe this work is a first step toward a complete methodology to fully extract the AW in CT images.

Indeed, the left and right frontiers of the AW in the frontal view are almost symmetrical and easy to identify. Though there are vague regions between AW and abdominal organs or tissues, its shape is approximately parallel to the AW muscle border which is easy to obtain. To compute the AW initialization, we thus define and automatically extract two control points to construct a spatial relationship between the AW muscle border and the AW. Initial qualitative experiments on three patient data indicate that our approach can obtain reasonable results

close to the liver despite the weak gradient between it and the AW, which is usually a critical issue in the segmentation.

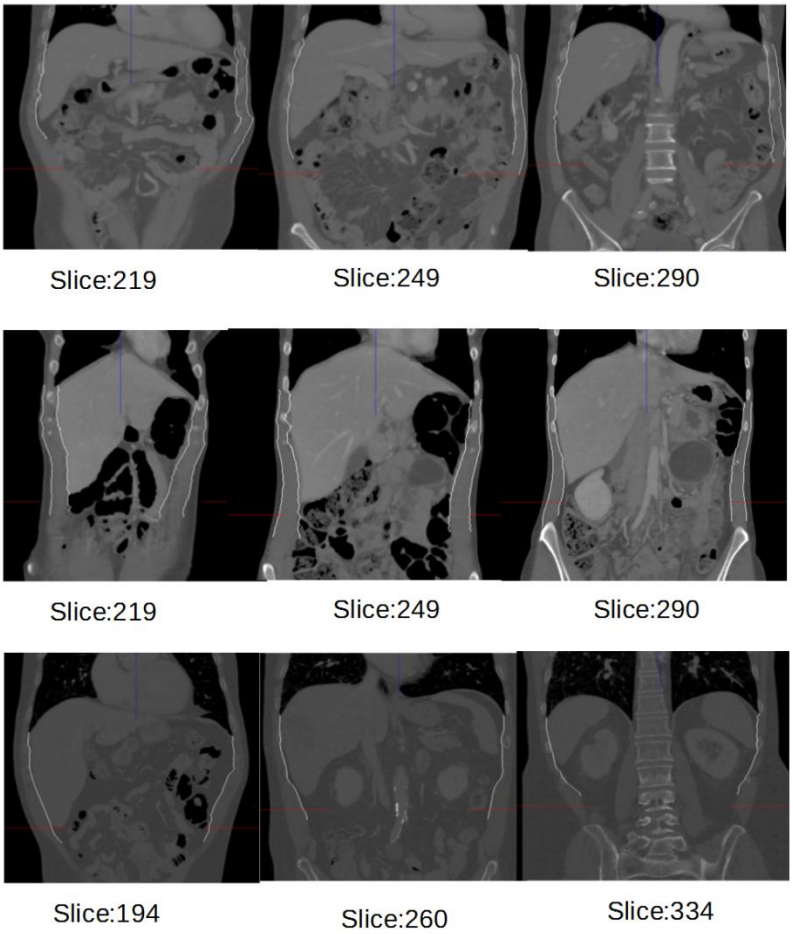

FIGURE 6.17: Automatic segmentation of AW in frontal slices. Three rows represent the image from different patients and several slices are extracted for each patient, the slice index has been marked.

Since our approach generate control points in each frontal view based on rib and the bottom points of lung, it does not work in the slices where rib information is missing. We think that an analysis in sagittal or axial slice may allow to perform the segmentation of AW in the anterior region that our approach currently does not consider. We believe it may be an advantage to perform a piecewise segmentation using different slice angle in the data volume, so that we can combine all good features or a priori information of each view and avoid its limitation.

To conclude, we believe our approach may lead to a fully automatic approach since the methods use a good prior to find the real position of the AW and also inspire the segmentation of other tissues in similar context. To reduce the sensitivity to fast density changes, we should include some mechanical constraint on the extracted contours so that they remain smooth. A

quantitative comparison of our segmentation result with ground truth data, which has been obtained in the Chapter 4 is also required in the future.

Chapter 7 Conclusion and perspective

The purpose of this thesis was to implement an accurate registration of multi-phase CT image on abdominal viscera to help the diagnosis and treatment of abdominal cancers. We have designed two segmentation tools to remove the AW and thoracic wall quickly after analyzing the registration issue caused by the breathing motion. We applied two non-rigid registration algorithms on the new images without AW and TV generated from previous segmentation, the evaluation on patient data demonstrates that our solution can remove the sliding motion effectively and obtain realistic accuracy. Since the position of AW can be used as a prior for many applications, its automatic segmentation has also been explored. The contributions of our research can be categorized as following.

7.1 Contributions

7.1.1 Analysis of the motion mechanism in the abdominal viscera

We have analyzed that the diaphragm and the inter-costal muscle are the main driving factor of the breathing motion which results in different kind of motion in the thoracic and abdominal viscera. During the breathing motion, the lung moves along cranial-caudal direction with a big magnitude while the AW moves mainly in the antero-posterior direction: thus a big sliding motion happens at the AW interface. There is also a sliding motion between abdominal organs (in particular the liver and spleen which are located beneath the diaphragm) and lung since these organs rotate and slide along antero-posterior direction

These two sliding motions cause the motion field discontinuity at sliding interface and contradict standard registration approaches which assume the spatial deformation is homogeneous across the whole image region. We conclude that the position of these sliding motions should be taken into account as a prior information to obtain an accurate registration result on abdominal viscera, whereas the small sliding motion between abdominal organs should be properly recovered with a standard local deformable transformation model.

7.1.2 Fast segmentation of abdominal and thoracic wall

We have proposed to adopt the sliding motion interface as a spatial a priori for the registration of abdominal image. However, the segmentation of abdominal wall is a challenge because of its multiple connections with abdominal organs with similar intensity values. Diaphragm is also difficult to delineate close to the heart since grey level values can be close to liver ones.

To tackle these segmentation issues, we used smooth curvature property of the AW and implement two semi-automatic softwares which automatically generate interpolated surfaces from control points drawn by the user in some slices only. Our quantitative experiment on 20 patient images has demonstrated that 15 slices on average are enough to reach an accurate segmentation. We have also shown that these segmentation steps could be performed in a very reasonable time slot thanks to a tricky user interface, especially adapted to the task.

7.1.3 Accurate registration of abdomen multiphase CT

We have proposed a simple yet effective approach to provide an accurate registration of abdominal viscera in multiphase CT images based on sliding motion interface position. Indeed, replacing the tissues outside the AW and the diaphragm interface by a constant intensity value is sufficient to remove the discontinuous deformation area in the images to be registered. Evaluation on 10 patient CT images has demonstrated the efficiency of our strategy using three evaluation metrics. In addition, two state of the art algorithms (MMI + B-splines and Super Baloo) have been tested and similar outcome has been obtained which show the proposed strategy is not algorithm dependant. These experiments also indicated that there is sometimes a big registration error close to the diaphragm when the TV has not been removed from the images to be registered. This is consistent with our previous analysis of the motion mechanism in abdominal viscera, where we highlighted that the sliding motion between the lungs and the abdominal viscera can be important, and thus highly discontinuous. Further tests are still necessary to clearly quantify when thoracic viscera should be removed to ensure the registration accuracy. Since this error mainly comes from the inconsistent motion between the lungs (which expand) and the liver (which slides on the diaphragm), a basic analysis of the lung deformation may be sufficient.

It is interesting to note that if an accurate registration of entire abdomen is obtained, the segmentation of abdominal organs can be propagated from one segmented image only to the oth-

er images. Such method is thus extremely useful for surface mesh based research, since it helps to avoid an important segmentation task on the other images of the same patient.

7.1.4 Automatic segmentation of AW

Since the registration result based on interactive segmentation is very satisfying, we have further investigated an automatic segmentation approach of the AW. After analysis CT images in axial, frontal and sagittal views, we found that there are some advantages to perform the segmentation in the frontal view. In particular, the AW muscle border is approximately parallel to the AW border. Therefore, we have designed an automatic segmentation algorithm for a selected stack of frontal view by employing a priori spatial information of ribs, lung and muscle border. Though the experiments on three patient images are not sufficient, results have shown that our approach can successfully solve the critical issue of vague regions between the liver and the abdominal wall.

7.2 Perspective

7.2.1 Extension to other image modalities

On the one hand, we need to apply our approach on much more arterial and venous image data in order to confirm its robustness. On the other hand, we know that the sliding motion is a common problem for all 3D intensity-based registrations on the abdominal region. Thus, it is necessary to extend our approach to much more modalities which are also used in surgical planning or post-operative surgical evaluations. For instance, preoperative CT and MR images are used for surgical planning, pre-operative CT/MR and intra-operative MR images are integrated for image-guided surgery, pre-operative CT/MR and post-operative CT/MR are used for outcome evaluation of a surgical treatment. However, in such case, the image information matching is probably more complex due to the long interval between the acquisitions. Therefore, the feasibility and accuracy of our registration approach needs to be evaluated.

7.2.2 Improvement of the fast segmentation of AW

For the fast segmentation of AW, we empirically evaluated the number of necessary slices to obtain an accurate segmentation. However, we have to admit that this selection is user-dependent, which also leads users to spend much time on this choice. We believe an automatic selection can be achieved by taking two factors into account: the length of the volume image and the curvature of the AW along the cranio-caudal direction. The first factor can be

used to automatically calculate the NSS based on the knowledge resulting from the previous experiment. Although the second factor cannot be computed directly, a good approximation of the AW curvature can be computed from the AW muscle shape which is easy to extract. Once the curvature along cranio-caudal direction is known in each point, we can use Shannon theory to automatically adapt the density of slices with respect to the shape (considering the shape as a signal with a varying frequency). This approach would have two advantages, speeding up the segmentation process and making the surface interpolation more accurate.

7.2.3 Improvement of the automatic segmentation of abdominal wall

Automatic extraction of ribs is mainly based on threshold operation, however, this value is patient specific, and also depends on the amount of contrast agent in images. There are also some overlaps between the lowest intensity value of bones and highest values of surrounding tissues, particularly in the contrast enhanced image, the intensity value of vessels or the liver is around 400 HU. Other approaches about ribs segmentation have been proposed using rib center line progressive tracing (Yao et al., 2012), region growing (Ramakrishnan et al., 2011) and shape descriptor (Gargouri et al., 2013), we plan to implement and combine them with our current method in order to decrease the influence of contrast agent.

In the initial border generation, we use the shape information of muscle border and the position of two control points. Then, this initial border is used to refine the edge of abdominal wall. The refinement strategy finds the pixel with a highest gradient magnitude which is seen as edge of abdominal wall. However, there is tissue or region with relative low intensity at right of the initial border but within the abdominal wall. In such context, this edge will be recognized as an edge of abdominal wall by our algorithm. We believe that if an intensity value distribution model of the AW can be built, it will be easier to recognize the outliers.

One limitation for segmentation in the frontal views is that there is no rib information that can be employed, particularly at the end of slices in anterior and posterior direction. Therefore, a solution should be investigated to decide the range of segmentation along anterio-posterior direction. We think the number of ribs in frontal slice can be used as a reference for the range selection. For the remaining slices, we propose to switch the segmentation process in sagittal or axial views.

The posterior part should be tackled in axial view, since it follows the spine boundary. However, a dedicated process should be included to take the psoas muscle into account. This

seems feasible using anatomical knowledge: psoas are located on the right and left regions of the spine, have a specific elliptic shape in axial slices and its grey value is rather constant.

The anterior part may be tackled either in axial or sagittal slices. Indeed, it seems easy to follow the lung curvature to extract the AW in sagittal slice, yet this basic strategy will not work on sagittal slice containing the heart. We may then resort to axial slice analysis using the sternum or anterior muscle border. More generally, it seems relevant to try to find the advantages of each orthogonal view to perform a piecewise extraction of the AW.

7.2.4 Integrating our registration algorithm into a surgical planning software

Since our registration accuracy has reached one pixel level, it is meaningful to integrate it into a surgical planning software to facilitate the surgeons understanding of tumor and vessel position with respect to surrounding tissue. However, there is always gap between research and clinical application. For instance, we know that the abdomen registration works well if the segmentation of the AW and the TV have been properly performed, yet it is hard to predict to what extent the registration will fail if the prior segmentation contains some mistakes (like piece of rib or muscle included in the segmented images), which will certainly happen from time to time. Since the surgical planning cannot afford such mistake, we should be able to provide a supplementary tool allowing the user to quickly understand whether the registration is accurate or not, and if possible to give instructions to correct the mistake. The path to reach a certified registration software of the abdomen is still long.

Part II Appendix and bibliography

A. French summary

A.1 Introduction

A. 1.1 Contexte Clinique

Le nombre de cancer de l'appareil digestif, incluant le foie, les reins et le pancréas est en augmentation constante et représente un facteur de mortalité non négligeable dans le monde. Les traitements actuels, comme la transplantation, la résection et la thermo-ablation par radio-fréquence, sont efficaces et réduisent l'atteinte aux tissus sains avoisinant la/les tumeurs.

Le choix du traitement se fait habituellement à l'aide d'images préopératoires (typiquement TDM) pendant la planification chirurgicale. Comme les images TDM standard ne permettent pas souvent de bien différencier les tissus cancéreux des tissus sains, il est classique de procéder à une injection de produit de contraste dans le sang du patient. Cela permet d'obtenir deux images différenciées, appelées temps artériel et temps veineux, selon la position de l'agent de contraste dans le réseau sanguin du patient. Néanmoins, certaines informations visibles dans une des modalités ne le sont pas forcément dans l'autre (tumeur visible dans le temps artériel uniquement et veines dans le temps veineux). Il est donc nécessaire de procéder à une fusion d'images TDM artérielle et veineuse, communément appelée multi-phases, afin de pouvoir bénéficier de toutes les informations importantes simultanément. Cette fusion est communément appelée recalage multi-phase.

Afin de réaliser cette tâche, il est habituel de recourir à un algorithme de recalage. Cependant, le recalage d'images abdominales est complexe car les tissus sont déformés en permanence par les muscles et par la gravité. En particulier, les organes abdominaux glissent le long de la paroi abdominale pendant la respiration, ce qui rend une fusion d'image souvent inutile étant donné que le patient n'arrive que très rarement à reproduire la même respiration pendant les 2 acquisitions TDM artérielle et veineuse. La FIGURE.A. 1, montrant 2 coupes frontales issues d'images multi-phases, illustre bien ce phénomène : on peut voir que le foie est descendu de plusieurs centimètres et que les reins ont été déformés en plus d'avoir bougé aussi dans la direction antéro-postérieure. Ce phénomène génère un champ de déformation discontinu au niveau de l'interface de glissement. A noter qu'il y aussi un glissement entre les poumons et les viscères abdominaux qui ne peut pas non plus être négligé.

(a) (b) (c)

FIGURE.A. 1: Illustration du glissement et des déformations des viscères le long de la paroi abdominale après superposition de l'image de phase artérielle (a) sur l'image de phase veineuse (b) dans une vue frontale. Le résultat de la superposition des deux images est visible dans (c), la courbe jaune en pointillé soulignant l'interface de glissement.

A.1.2 Objectifs

L'objectif de cette thèse est de fournir une méthode permettant de recaler les images multi-phases TDM des viscères abdominaux, malgré le phénomène de glissement évoqué dans la section précédente. Notre approche devra surmonter les problèmes suivants :

1) La technique devra permettre de recaler les organes de l'abdomen et leurs vaisseaux environnants.

2) Nous souhaitons que notre approche prenne en compte la respiration et son influence sur les viscères abdominaux.

3) Nous nous limitons dans l'immédiat au recalage d'images TDM multi-phases, et étendrons si possible au recalage TDM-IRM.

A.1.3 Notre stratégie

Notre état de l'art n'a pas mis en évidence de travail de recalage sur la région abdominale prenant en compte le phénomène de respiration. En revanche, des travaux gérant les problèmes liés à la respiration ont été réalisés sur des images du thorax (Ruan et al., 2008; A. Schmidt-Richberg et al., 2009; Alexander Schmidt-Richberg et al., 2012a; Alexander Schmidt-Richberg et al., 2012b; D. Pace et al., 2013; Y. Xie et al., 2011; Vandemeulebroucke et al., 2012).

En accord avec les conclusions de ces travaux, nous pensons que l'information a priori de la zone de glissement est nécessaire pour permettre un recalage réaliste et précis dans la zone abdominale. Notre stratégie est illustrée sur la FIGURE.A. 2. La première étape consiste à réaliser une segmentation rapide de la paroi abdominale et du diaphragme, et de générer de nouvelles images exemptes de la paroi abdominale et des viscères thoraciques. En second lieu, un algorithme de recalage non-rigide approprié est appliqué sur les nouvelles images

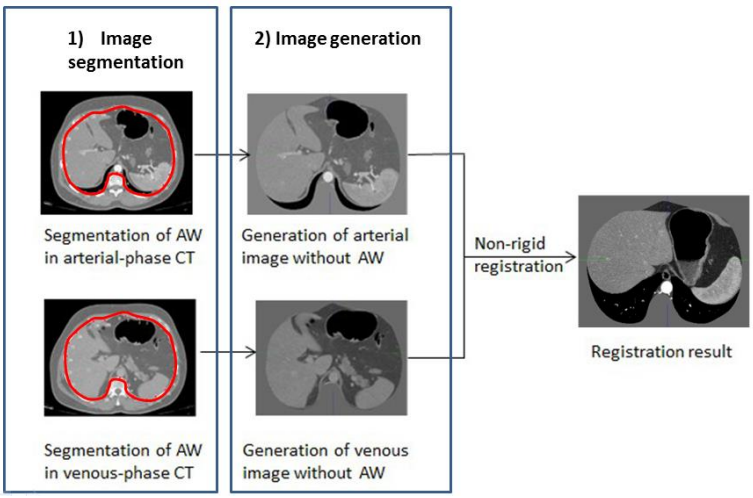

FIGURE.A. 2: Illustration de notre stratégie.

A.2 Segmentation rapide de la paroi abdominale et du diaphragme

A.2.1 Outil de segmentation rapide de la paroi abdominale

La segmentation rapide de la paroi abdominale est basée sur la faible courbure de la paroi dans la direction cranio-caudale. Etant donné une image 3D de l'abdomen, la stratégie de notre outil de segmentation rapide est décrite ci-après.

L'utilisateur sélectionne plusieurs coupes axiales, espacées d'un ou plusieurs centimètres, dans laquelle il va segmenter la paroi abdominale à l'aide de points de contrôle. Une interpolation cubique 2D de type spline à partir des points de contrôle est choisie pour estimer le contour des viscères abdominaux dans les coupes axiales sélectionnées. Les coupes restantes sont alors automatiquement segmentées en temps réel à partir d'un calcul de spline 3D reliant les points de contrôle adjacents dans le sens cranio-caudal (cf. FIGURE.A. 3 (a)). Finalement, un maillage 3D peut être généré et une vue MPR 3D classique est utilisée afin de vérifier la qualité de la segmentation par inspection de la position du maillage vis-à-vis de tissus avoisinants, comme les os et les côtes. La FIGURE.A. 3 (b)FIGURE 4.15 illustre le résultat d'une segmentation réalisée sur deux images TDM multi-phases avec un nombre de coupes axiales respectifs de 20 (phase veineuse) et 10 (phase artérielle).

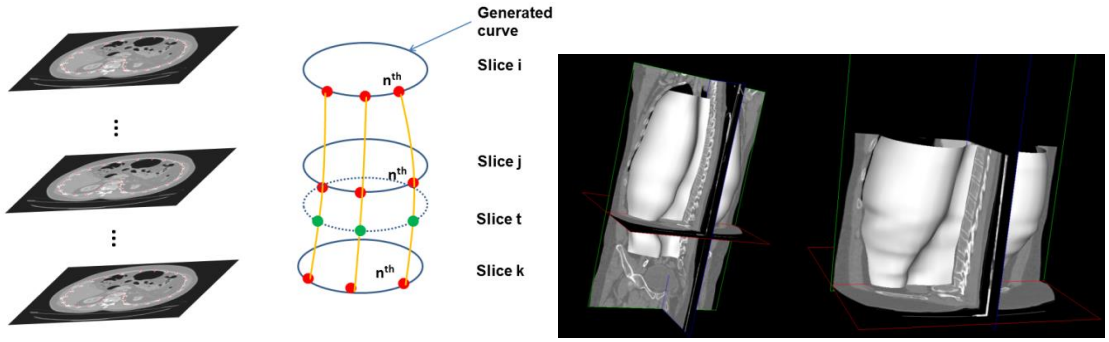

(a) (b)

FIGURE.A. 3: (a) Illustration de l'interpolation par B-spline 3D dans le sens cranio-caudal. (b) Le maillage généré à partir de l'image TDM en phase veineuse (à gauche) et en phase artérielle (à droite).

A.2.2 Outil de segmentation rapide du diaphragme

Le principe de la segmentation est basé sur la même idée, la courbure du diaphragme étant plutôt faible dans les coupes sagittales. Quelques segmentations dans plusieurs coupes sagittales devraient donc suffire à interpoler précisément l'intégralité du diaphragme.

L'utilisateur sélectionne d'abord une coupe axiale au milieu du patient qui ne contienne aucun tissu correspondant au poumon. Le logiciel sélectionne alors 15 coupes sagittales uniformément réparties entre les extrémités droite et gauche de la frontière 2D de la coupe axiale (cf. FIGURE.A. 4(a)). L'utilisateur réalise la segmentation du diaphragme dans ces coupes sagittales (un exemple de coupe choisie est présenté dans la FIGURE.A. 4FIGURE 4.16(b)). Une fois que toutes les coupes ont été segmentées, chaque extrémité des rayons est reliée avec son voisin de droite et gauche en utilisant une spline 3D dans la direction latérale (cf. FIGURE.A. 5(a)). Finalement, un maillage de type quad décrivant la position du diaphragme est produit (cf. FIGURE.A. 5 (b) FIGURE 4.18).

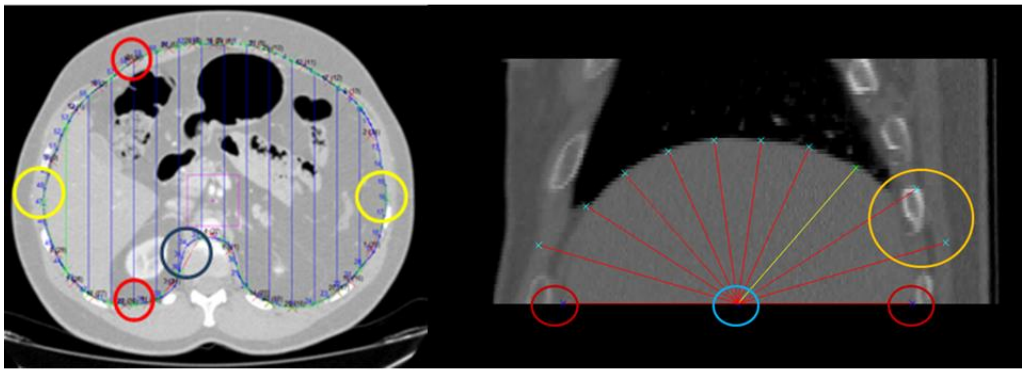

(a) (b)

FIGURE.A. 4:Illustration du mécanisme pour la segmentation interactive du diaphragme.

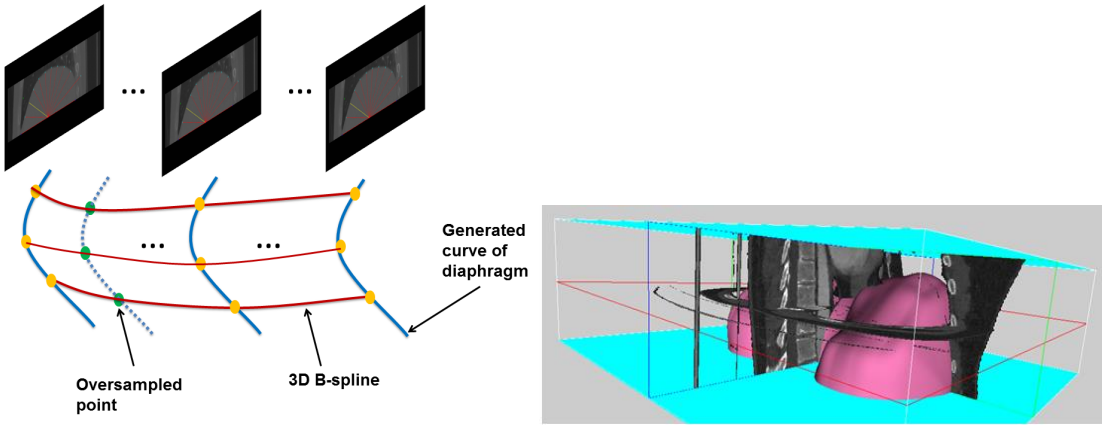

(a) (b)

FIGURE.A. 5: (a) Illustration de l'interpolation latérale dans les coupes sagittales par des Bspline 3D. (b) Le maillage généré (en rose) représente le diaphragme.

Afin d'évaluer le nombre de coupes nécessaires pour réaliser une segmentation rapide précise, nous avons procédé à l'expérimentation suivante. Nous avons segmenté sur 20 images TDM la paroi-abdominale avec les nombres de coupes suivants: 5, 10, 20, 50 considérant que la segmentation à 50 coupes (environ tous les centimètres) correspond à la vérité terrain. Concrètement l'erreur de segmentation avec 10 coupes et 20 coupes est de l'ordre de grandeur du voxel de l'image (1 mm). La durée de segmentation a aussi été évaluée avec 6 utilisateurs et nous montrons que la segmentation conjointe de la paroi abdominale et du diaphragme peut être réalisée en 10 minutes, ce qui est compatible avec les contraintes de routine clinique.

A.3 Recalage non-rigide précis d'images TDM multi-phases par effacement de la paroi abdominale et des viscères thoraciques

Deux algorithmes reconnus ont été utilisés pour évaluer le recalage non-rigide après application de notre stratégie.

A.3.1 Données expérimentales

L'évaluation est réalisée sur 10 images TDM multi-phases (10 phases artérielles et 10 phases veineuses). La taille originale des images de phase veineuse (resp. artérielle) est $512 \times 512 \times 500$ (resp. $512 \times 512 \times 400$) avec une résolution de $0.961 \times 0.961 \times 0.961$ mm. Nous avons effectué les recalages sur trois ensembles d'images : les images originales avec paroi abdominale et viscère thoracique, les nouvelles images sans paroi abdominale (cf. FIGURE.A. 6 错误!未找到引用源。(a)), et les nouvelles images sans paroi abdominale ni viscère thoracique (cf. FIGURE.A. 6 错误!未找到引用源。(b)).

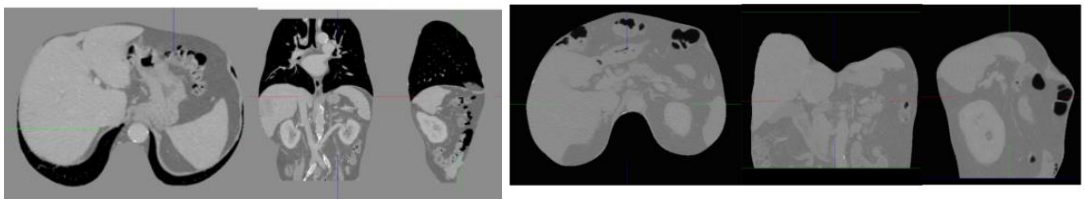

(a) (b)

FIGURE.A. 6: (a) Nouvelles images sans paroi abdominale (b) Nouvelles images sans paroi abdominale ni viscère thoracique.

A.3.2 Méthodologie

A.3.2.1 Description des deux algorithmes de recalage non-rigide

La première méthode de recalage combine un modèle de déformation de type Bspline avec une transformation composée d'une transformation rigide, puis affine puis déformable localement (free form deformation (FFD)):

$$T(x,y,z) = T_{localDeformable}\left(T_{globalAffine}\left(T_{globalRigid}(x,y,z)\right)\right)$$

A cause de la variation d'intensité possible entre la phase artérielle et veineuse, nous choisissons d'utiliser une métrique de type information mutuelle (Mattes MI) (Schroeder et al., 2003).

L'algorithme Super Baloo est basé sur de l'appariement de bloc pyramidal. La dimension des blocs dans nos expériences est de $5 \times 5 \times 5$ voxels. La mesure de similarité choisie est le coefficient de corrélation au carré (SCC). Nous avons utilisé l'implémentation disponible sur la plateforme MedINRIA (Ourselin et al., 2000).

A.3.2.2 Métriques d'évaluation

Nous proposons trois métriques usuelles pour évaluer la précision de notre approche. La première est une inspection qualitative après superposition 2D des coupes des images recalées. La seconde métrique est la mesure quantitative de la distance entre les maillages de surface de différents organes après recalage (ici le foie, les reins et la rate). La troisième métrique consiste à mesure l'erreur de recalage au niveau des bifurcations de certains vaisseaux des viscères situés à l'extérieur des organes.

A.3.3 Résultats

A.3.3.1 Comparaison qualitative des images

La FIGURE.A. 7 montre sur un patient la fusion des images source (en rouge) et cible (en vert) après recalage avec la méthode B-spline+MMI. L'opacité n'est pas complète pour permettre une évaluation visuelle. Les 3 lignes représentent les résultats fusionnés avant recalage, après recalage avec les images originales et après recalage avec les images desquelles la paroi abdominale et les viscères thoraciques ont été enlevés. On voit bien que le recalage avec les images d'origine n'est pas performant (seconde ligne) alors qu'avec notre approche (troisième ligne), les frontières des organes sont très bien recalées.

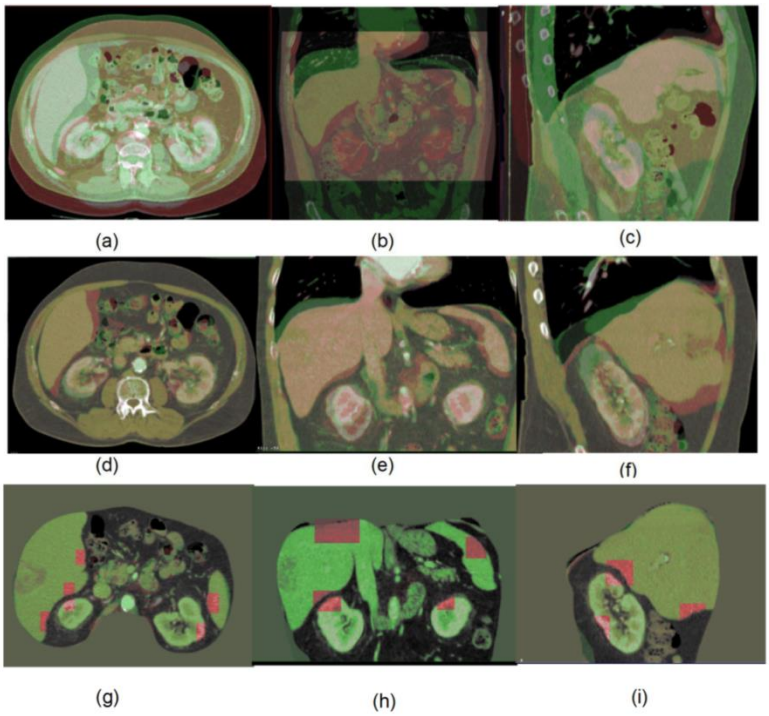

FIGURE.A. 7: Résultat de recalage sur un patient avec la méthode B-spline+MMI. Les 3 lignes représentent les images fusionnées avant recalage, après recalage avec les images originales et après recalage avec les images desquelles la paroi abdominale et les viscères thoraciques ont été enlevés

A.3.3.2 Analyse quantitative du recalage sur quatre organes

Le temps de recalage moyen avec la méthode B-spline+MMI est de 300±20 secondes, et 500±25 secondes avec Super Baloo. Les erreurs de recalage avec la méthode Bspline+MMI sont respectivement avant recalage pour le foie, le rein gauche, le rein droit et la rate de 6.7 (±4.8), 3.1 (±1.8), 2.9 (±1.8) and 4.8 (±3.8) mm. Ces erreurs sont réduites à 3.6 (±3.6), 1.5 (±1.1), 1.2 (±0.9) and 3.5 (±4.4) mm respectivement après recalage avec les images originales, et finalement réduite à 1.1 (±0.3), 0.3 (±0.1) ,0.3 (±0.1) and 0.5 (0.3) mm avec notre approche. L'erreur moyenne de recalage de bifurcations sélectionnées par l'utilisateur avant recalage est de 11 mm, réduit à 8 mm après recalage avec les images originales, et finalement encore réduite à environ 1 mm avec notre approche. Des résultats similaires ont été obtenus en utilisant l'algorithme Super Baloo (cf. FIGURE.A. 8).

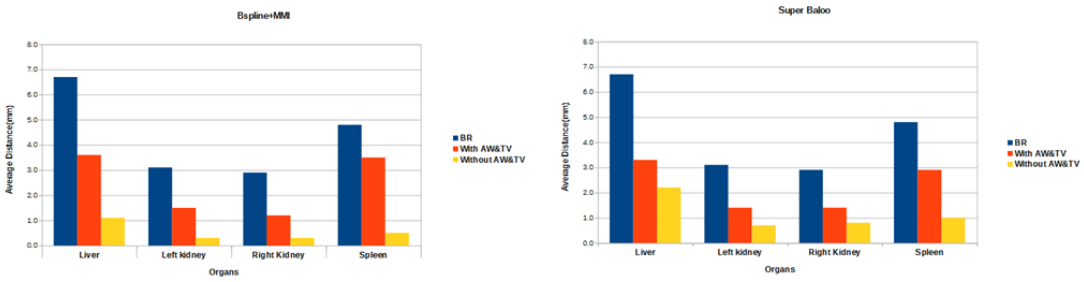

(a) (b)

FIGURE.A. 8: Comparaison de la précision du recalage sur 4 organes avec la méthode B-spline+MMI (a) et Super Baloo(b). La barre bleue indique l'erreur de recalage moyenne avant recalage; la barre orange correspond à l'erreur de recalage avec les images originales, et la barre jaune avec les images desquelles la paroi abdominale et les viscères thoraciques ont été enlevés.

A.4. Segmentation automatique de la paroi abdominale

Nous proposons une approche partielle basée sur la connaissance a priori des muscles abdominaux et des côtes pour segmenter automatiquement la paroi abdominale dans les coupes frontales. La segmentation est effectuée indépendamment sur le côté droit et gauche. Notre stratégie est résumée dans la FIGURE.A. 9 & FIGURE 6.3. En premier lieu, nous générons les masques des structures suivantes: poumons (cf. FIGURE.A. 10 (a)), frontière des muscles de la paroi abdominale sans les tissus adipeux et la peau dans une image de gradient (cf. FIGURE.A. 10 (b)) et les côtes sans la colonne vertébrale et le pelvis (cf. FIGURE.A. 10 **错误!未找到引用源。**(c)).

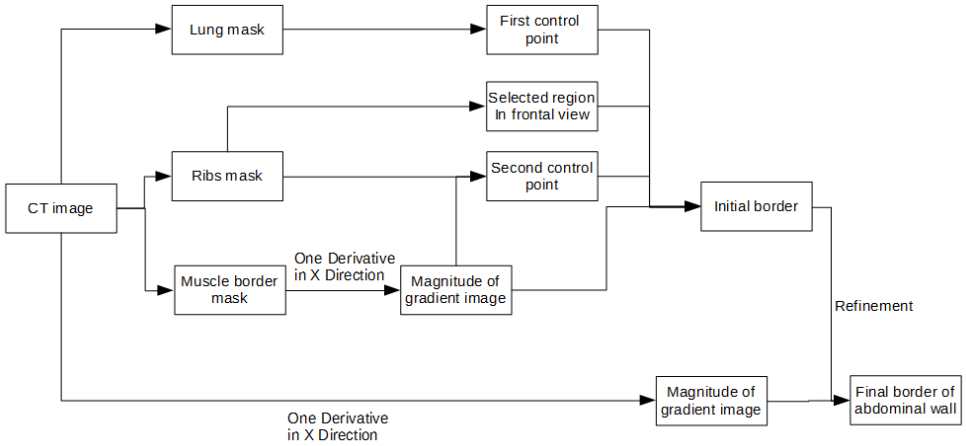

FIGURE.A. 9: Schéma de notre stratégie pour extraire la paroi abdominale dans les coupes frontales.

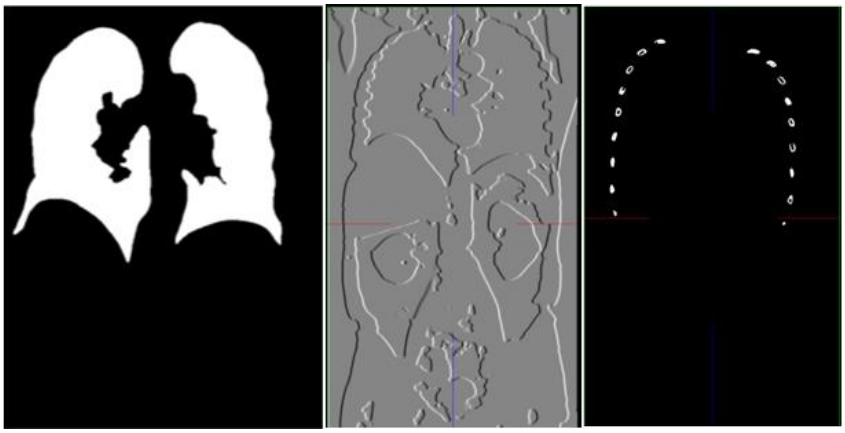

(a) (b) (c)

FIGURE.A. 10: (a) Masque des poumons (b) Image de gradient mettant en évidence la frontière des muscles de la paroi abdominale dans la direction des x (MGX) (c) Masque des côtes.

Ensuite, deux points de contrôle sont extraits de chaque côté du patient à partir des images générées précédemment. La frontière initiale de la paroi abdominale avant raffinement est calculée à partir de la distance entre les 2 points de contrôle et la frontière des muscles (cf. FIGURE.A. 11 错误!未找到引用源。).

FIGURE.A. 11: Generated initial border of right AW.

Finalement, le raffinement est réalisé grâce à l'image de gradient MGX en cherchant dans la direction des x vers le centre de l'image le plus fort gradient autour du contour initial. La zone de recherche est bien évidemment limité (pratiquement 5 mm). Finalement, cette approche a été appliquée sur 3 images TDM parmi les données patient disponibles (illustré dans la 错误!未找到引用源。) FIGURE 6.17.

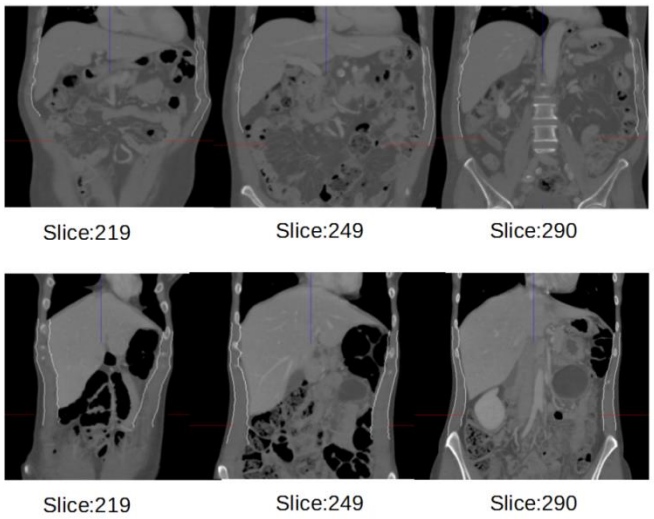

FIGURE.A. 12: Segmentation automatique de la paroi abdominale dans les coupes frontales. Les deux lignes représentent les images frontales de deux patients à des hauteurs différentes : les index des coupes ont été relevés.

A.5 Conclusion et perspectives

A.5.1 Conclusion

Nous avons identifié les principales zones de glissement pendant la respiration : tout d'abord entre les poumons et la paroi abdominale, puis entre les organes viscéraux et les poumons, en particulier le foie et la rate qui glissent et effectuent une rotation antéro-postérieure tandis que les poumons s'étirent dans la direction caudale. Ces deux glissements créent un champ de déplacement discontinu au niveau des interfaces et contredisent l'hypothèse standard des algorithmes de recalage classiques, à savoir que le champ de déformation doit être globalement homogène.

Nous avons proposé une approche simple mais efficace pour fournir un recalage précis et réaliste des viscères dans des images TDM multi-phases, en prenant en compte les glissements principaux présents pendant la respiration. Notre stratégie est de retirer des images source et cible la paroi abdominale et les viscères thoraciques, et de les remplacer par une valeur de gris constante. Afin de montrer que cette approche ne dépend pas de l'algorithme de recalage, nous avons testé deux algorithmes de l'état de l'art : MMI + B-splines et Super Baloo. Des expérimentations sur 10 patients ont montré que les résultats de recalage sont bien meilleurs avec les deux algorithmes, puisque l'erreur est réduite de 2-4 mm à 1 mm en moyenne, que ce soit au niveau des organes ou des vaisseaux situés entre les organes.

Pour que cette approche soit réaliste et utilisée en routine clinique, il est indispensable de pouvoir segmenter suffisamment rapidement la paroi abdominale et le diaphragme. Pour cela, deux logiciels de segmentation interactive rapide ont été mis au point, reposant sur la faible courbure des interfaces de glissement, et donc la possibilité de recourir à des techniques interpolations. Nos expériences sur 20 images de patient ont montré qu'en moyenne une

segmentation des interfaces sur une quinzaine de coupes était suffisante pour obtenir une très bonne précision en moins de 10 minutes.

Finalement, nous avons exploré la possibilité de fournir un algorithme de segmentation automatique de la paroi abdominale. Notre analyse est réalisée sur les coupes frontales en se servant des informations anatomiques suivantes extraites préalablement: poumons, côtes et muscles abdominaux. Bien que la validation ne soit pas suffisante, les premiers résultats sont encourageants et montrent qu'il est possible de résoudre le problème du contour vague entre le foie et la paroi abdominale.

A.5.2 Perspective

A l'avenir, nous prévoyons tout d'abord d'étendre notre approche à plus de modalités qui sont aussi utilisées pour le planning chirurgical ou les évaluations post-opératives. En second lieu, nous pensons qu'une sélection automatique des coupes à segmenter manuellement est possible en prenant en compte la courbure des muscles abdominaux dans le sens cranio-caudal. En troisième lieu, nous souhaitons améliorer le raffinement effectué pour trouver la position de la paroi abdominale à partir des muscles abdominaux. Nous pensons que si un modèle de distribution des niveaux de gris de l'abdomen pouvait être construit, il serait plus facile de reconnaître les faux positifs.

Une limitation de notre approche automatique est liée au fait que les côtes ne sont pas toujours présentes en particulier en limite de volume dans les coupes frontales. Nous prévoyons d'intégrer les informations utiles provenant des coupes axiales et sagittales afin de surmonter cette limitation. De manière générale, il nous semble important d'essayer de trouver les avantages de chaque vue orthogonale et de fournir une extraction par morceau de la paroi abdominale.

Finalement, au vu de la précision de recalage atteinte, qui atteint les objectifs cliniques, il faudra intégrer notre approche dans une solution de recalage utilisée en routine afin d'évaluer le bénéfice médical.

Bibliography

1. Abraham, R., Marsden, J. E., & Rațiu, T. S. (1988). *Manifolds, tensor analysis, and applications* (Vol. 75): Springer.
2. Adams, R., & Bischof, L. (1994). Seeded region growing. *Pattern Analysis and Machine Intelligence, IEEE Transactions on, 16*(6), 641-647.
3. Andronache, A., von Siebenthal, M., Székely, G., & Cattin, P. (2008). Non-rigid registration of multi-modal images using both mutual information and cross-correlation. *Medical image analysis, 12*(1), 3-15.
4. Arun, K. S., Huang, T. S., & Blostein, S. D. (1987). Least-squares fitting of two 3-D point sets. *Pattern Analysis and Machine Intelligence, IEEE Transactions on*(5), 698-700.
5. Ashburner, J. (2007). A fast diffeomorphic image registration algorithm. *Neuroimage, 38*(1), 95-113.
6. Avants, B. B., Tustison, N. J., Song, G., Cook, P. A., Klein, A., & Gee, J. C. (2011). A reproducible evaluation of ANTs similarity metric performance in brain image registration. *Neuroimage, 54*(3), 2033-2044.
7. Axila, y. M. (2006). Anatomy of the thoracic wall, axilla and breast. *Int. J. Morphol, 24*(4), 691-704.
8. Bajcsy, R., Lieberson, R., & Reivich, M. (1983). A computerized system for the elastic matching of deformed radiographic images to idealized atlas images. *Journal of computer assisted tomography, 7*(4), 618-625.
9. Banik, S., Rangayyan, R. M., & Boag, G. S. (2010). Automatic segmentation of the ribs, the vertebral column, and the spinal canal in pediatric computed tomographic images. *Journal of digital imaging, 23*(3), 301-322.
10. Bano, J., Hostettler, A., Nicolau, S., Cotin, S., Doignon, C., Wu, H., . . . Marescaux, J. (2012a). Simulation of pneumoperitoneum for laparoscopic surgery planning *Medical Image Computing and Computer-Assisted Intervention–MICCAI 2012* (pp. 91-98): Springer.
11. Bano, J., Hostettler, A., Nicolau, S., Doignon, C., Wu, H., Huang, M., . . . Marescaux, J. (2012b). Simulation of the abdominal wall and its arteries after pneumoperitoneum for guidance of port positioning in laparoscopic surgery *Advances in Visual Computing* (pp. 1-11): Springer.
12. Bano, J., Nicolau, S. A., Hostettler, A., Doignon, C., Marescaux, J., & Soler, L. (2013). Multiphase Liver Registration from Geodesic Distance Maps and Biomechanical Modelling *Abdominal Imaging. Computation and Clinical Applications* (pp. 165-174): Springer.
13. Befeler, A. S., & Di Bisceglie, A. M. (2002). Hepatocellular carcinoma: diagnosis and treatment. *Gastroenterology, 122*(6), 1609-1619.
14. Besl, P. J., & McKay, N. D. (1992). *Method for registration of 3-D shapes.* Paper presented at the Robotics-DL tentative.
15. Bialecki, E. S., & Di Bisceglie, A. M. (2005). Diagnosis of hepatocellular carcinoma. *Hpb, 7*(1), 26-34.
16. Bidaut, L. M., & Vallée, J. P. (2001). Automated registration of dynamic MR images for the quantification of myocardial perfusion. *Journal of magnetic resonance imaging, 13*(4), 648-655.

17. Bolondi, L., Sofia, S., Siringo, S., Gaiani, S., Casali, A., Zironi, G., . . . Sherman, M. (2001). Surveillance programme of cirrhotic patients for early diagnosis and treatment of hepatocellular carcinoma: a cost effectiveness analysis. *Gut, 48*(2), 251-259.
18. Borzio, M., Borzio, F., Macchi, R., Croce, A. M., Bruno, S., Ferrari, A., & Servida, E. (1994). The evaluation of fine-needle procedures for the diagnosis of focal liver lesions in cirrhosis. *J Hepatol, 20*(1), 117-121.
19. Brancatelli, G., Baron, R. L., Peterson, M. S., & Marsh, W. (2003). Helical CT screening for hepatocellular carcinoma in patients with cirrhosis: frequency and causes of false-positive interpretation. *American Journal of Roentgenology, 180*(4), 1007-1014.
20. Brandner, E. D., Wu, A., Chen, H., Heron, D., Kalnicki, S., Komanduri, K., . . . Shou, Z. (2006). Abdominal organ motion measured using 4D CT. *Int J Radiat Oncol Biol Phys, 65*(2), 554-560. doi: 10.1016/j.ijrobp.2005.12.042
21. Bravo, A. A., Sheth, S. G., & Chopra, S. (2001). Liver biopsy. *New England Journal of Medicine, 344*(7), 495-500.
22. Brock, K., Balter, J., Dawson, L., Kessler, M., & Meyer, C. (2003). Automated generation of a four-dimensional model of the liver using warping and mutual information. *Med Phys, 30*(6), 1128-1133.
23. Brock, K., Sharpe, M., Dawson, L., Kim, S., & Jaffray, D. (2005). Accuracy of finite element model-based multi-organ deformable image registration. *Med Phys, 32*(6), 1647-1659.
24. Brock, K. K., Dawson, L. A., Sharpe, M. B., Moseley, D. J., & Jaffray, D. A. (2006). Feasibility of a novel deformable image registration technique to facilitate classification, targeting, and monitoring of tumor and normal tissue. *International Journal of Radiation Oncology* Biology* Physics, 64*(4), 1245-1254.
25. Broit, C. (1981). Optimal registration of deformed images.
26. Brown, M. S., Mcnitt-Gray, M. F., Mankovich, N. J., Goldin, J. G., Hiller, J., Wilson, L. S., & Aberie, D. (1997). Method for segmenting chest CT image data using an anatomical model: preliminary results. *Medical Imaging, IEEE Transactions on, 16*(6), 828-839.
27. Brox, T., & Weickert, J. (2004). Level set based image segmentation with multiple regions *Pattern recognition* (pp. 415-423): Springer.
28. Bruix, J., Boix, L., Sala, M., & Llovet, J. M. (2004). Focus on hepatocellular carcinoma. *Cancer Cell, 5*(3), 215-219.
29. Bruix, J., Sherman, M., Llovet, J. M., Beaugrand, M., Lencioni, R., Burroughs, A. K., . . . Rodes, J. (2001). Clinical management of hepatocellular carcinoma. Conclusions of the Barcelona-2000 EASL conference. European Association for the Study of the Liver. *J Hepatol, 35*(3), 421-430.
30. Carrillo, A., Duerk, J. L., Lewin, J. S., & Wilson, D. L. (2000). Semiautomatic 3-D image registration as applied to interventional MRI liver cancer treatment. *Medical Imaging, IEEE Transactions on, 19*(3), 175-185.
31. Cash, D. M., Miga, M. I., Glasgow, S. C., Dawant, B. M., Clements, L. W., Cao, Z., . . . Chapman, W. C. (2007). Concepts and preliminary data toward the realization of image-guided liver surgery. *Journal of Gastrointestinal Surgery, 11*(7), 844-859.
32. Caturelli, E., Ghittoni, G., Roselli, P., De Palo, M., & Anti, M. (2004). Fine needle biopsy of focal liver lesions: the hepatologist's point of view. *Liver transplantation, 10*(S2), S26-S29.
33. Chalasani, N., Horlander, J. C., Said, A., Hoen, H., Kopecky, K. K., Stockberger, S. M., . . . Lumeng, L. (1999a). Screening for hepatocellular carcinoma in patients with advanced cirrhosis. *The American journal of gastroenterology, 94*(10), 2988-2993.

34. Chalasani, N., Said, A., Ness, R., Hoen, H., & Lumeng, L. (1999b). Screening for hepatocellular carcinoma in patients with cirrhosis in the United States: results of a national survey. *The American journal of gastroenterology, 94*(8), 2224-2229.
35. Chen, H.-m., & Varshney, P. K. (2003). Mutual information-based CT-MR brain image registration using generalized partial volume joint histogram estimation. *Medical Imaging, IEEE Transactions on, 22*(9), 1111-1119.
36. Choi, B. I. (2004). The current status of imaging diagnosis of hepatocellular carcinoma. *Liver transplantation, 10*(S2), S20-S25.
37. Choi, D., Kim, S. H., Lim, J. H., Cho, J. M., Lee, W. J., Lee, S. J., & Lim, H. K. (2001). Detection of hepatocellular carcinoma: combined T2-weighted and dynamic gadolinium-enhanced MRI versus combined CT during arterial portography and CT hepatic arteriography. *Journal of computer assisted tomography, 25*(5), 777-785.
38. Christensen, G. E., Joshi, S. C., & Miller, M. I. (1997). Volumetric transformation of brain anatomy. *Medical Imaging, IEEE Transactions on, 16*(6), 864-877.
39. Christensen, G. E., Rabbitt, R. D., & Miller, M. I. (1994). 3D brain mapping using a deformable neuroanatomy. *Physics in medicine and biology, 39*(3), 609.
40. Christensen, G. E., Rabbitt, R. D., & Miller, M. I. (1996). Deformable templates using large deformation kinematics. *Image Processing, IEEE Transactions on, 5*(10), 1435-1447.
41. Clifford, M. A., Banovac, F., Levy, E., & Cleary, K. (2002). Assessment of hepatic motion secondary to respiration for computer assisted interventions. *Comput Aided Surg, 7*(5), 291-299. doi: 10.1002/igs.10049
42. Collignon, A., Maes, F., Delaere, D., Vandermeulen, D., Suetens, P., & Marchal, G. (1995). *Automated multi-modality image registration based on information theory.* Paper presented at the Information processing in medical imaging.
43. Cross-section-abdominal-wall-image. Retrieved 2 March, 2015, from http://www.dreamstime.com/royalty-free-stock-photos-cross-section-abdominal-wall-image18825688
44. Crum, W. R., Hartkens, T., & Hill, D. (2014). Non-rigid image registration: theory and practice.
45. Cummings, B. (2001). Available from anatomybodygallery Retrieved 2015, from Addison-Wesley Longman, Inc http://anatomybodygallery.com/anatomy-liver-artery/2161/hepatic-portal-vein-and-artery
46. Curley, S. A. (2003). Radiofrequency ablation of malignant liver tumors. *Annals of Surgical Oncology, 10*(4), 338-347.
47. Davies, S. C., Hill, A. L., Holmes, R. B., Halliwell, M., & Jackson, P. C. (1994). Ultrasound quantitation of respiratory organ motion in the upper abdomen. *Br J Radiol, 67*(803), 1096-1102.
48. Declerck, J., Feldmar, J., Betting, F., & Goris, M. L. (1996). *Automatic registration and alignment on a template of cardiac stress and rest SPECT images.* Paper presented at the Mathematical Methods in Biomedical Image Analysis, 1996., Proceedings of the Workshop on.
49. Delmon, V., Rit, S., Pinho, R., & Sarrut, D. (2013). Registration of sliding objects using direction dependent B-splines decomposition. *Phys Med Biol, 58*(5), 1303-1314. doi: 10.1088/0031-9155/58/5/1303
50. Di Bisceglie, A. M., Rustgi, V. K., HOOFNAGLE, J. H., DUSHEIKO, G. M., & LOTZE, M. T. (1988). Hepatocellular carcinoma. *Annals of internal medicine, 108*(3), 390-401.

51. Ding, F., Leow, W. K., & Venkatesh, S. (2009). *Removal of abdominal wall for 3D visualization and segmentation of organs in CT volume.* Paper presented at the Image Processing (ICIP), 2009 16th IEEE International Conference on.
52. Dogra, A., & Patterh, M. (2014). CT and MRI Brain Images Registration for Clinical Applications. *J Cancer Sci Ther, 6*, 018-026.
53. Donati, O., Reiner, C., Hany, T., Fornaro, J., von Schulthess, G., Marincek, B., & Weishaupt, D. (2010). 18F-FDG-PET and MRI in patients with malignancies of the liver and pancreas. *Nuklearmedizin, 49*(3), 106-114.
54. El-Serag, H. B., Marrero, J. A., Rudolph, L., & Reddy, K. R. (2008). Diagnosis and treatment of hepatocellular carcinoma. *Gastroenterology, 134*(6), 1752-1763.
55. El-Serag, H. B., & Mason, A. C. (1999). Rising incidence of hepatocellular carcinoma in the United States. *New England Journal of Medicine, 340*(10), 745-750.
56. Fedkiw, S. O. R. (2003). Level set methods and dynamic implicit surfaces.
57. Ferrant, M., Nabavi, A., Macq, B., Black, P. M., Jolesz, F. A., Kikinis, R., & Warfield, S. K. (2002). Serial registration of intraoperative MR images of the brain. *Medical image analysis, 6*(4), 337-359.
58. Fox, N. C., & Freeborough, P. A. (1997). Brain atrophy progression measured from registered serial MRI: validation and application to Alzheimer's disease. *Journal of magnetic resonance imaging, 7*(6), 1069-1075.
59. Frangi, A. F., Rueckert, D., Schnabel, J. A., & Niessen, W. J. (2002). Automatic construction of multiple-object three-dimensional statistical shape models: Application to cardiac modeling. *Medical Imaging, IEEE Transactions on, 21*(9), 1151-1166.
60. Freeborough, P. A., & Fox, N. C. (1998). Modeling brain deformations in Alzheimer disease by fluid registration of serial 3D MR images. *Journal of computer assisted tomography, 22*(5), 838-843.
61. Garcia, V., Commowick, O., & Malandain, G. (2010). *A robust and efficient block matching framework for non linear registration of thoracic CT images.* Paper presented at the Grand Challenges in Medical Image Analysis (MICCAI workshop).
62. Gargouri, M., Tierny, J., Jolivet, E., Petit, P., & Angelini, E. D. (2013). *Accurate and robust shape descriptors for the identification of RIB cage structures in CT-images with Random Forests.* Paper presented at the Biomedical Imaging (ISBI), 2013 IEEE 10th International Symposium on.
63. Gering, D. T., Nabavi, A., Kikinis, R., Hata, N., O'Donnell, L. J., Grimson, W. E. L., . . . Wells, W. M. (2001). An integrated visualization system for surgical planning and guidance using image fusion and an open MR. *Journal of magnetic resonance imaging, 13*(6), 967-975.
64. Gervais, D. A., McGovern, F. J., Arellano, R. S., McDougal, W. S., & Mueller, P. R. (2005). Radiofrequency ablation of renal cell carcinoma: part 1, Indications, results, and role in patient management over a 6-year period and ablation of 100 tumors. *American Journal of Roentgenology, 185*(1), 64-71.
65. Gillams, A. (2005). The use of radiofrequency in cancer. *British journal of cancer, 92*(10), 1825-1829.
66. Glocker, B., Komodakis, N., Tziritas, G., Navab, N., & Paragios, N. (2008). Dense image registration through MRFs and efficient linear programming. *Medical image analysis, 12*(6), 731-741.
67. Glombitza, G., Lamadé, W., Demiris, A. M., Göpfert, M.-R., Mayer, A., Bahner, M. L., . . . Herfarth, C. (1999). Virtual planning of liver resections: image processing, visualization and volumetric evaluation. *International Journal of Medical Informatics, 53*(2), 225-237.

68. Grimson, W. E. L., Ettinger, G., White, S. J., Lozano-Perez, T., Wells Iii, W., & Kikinis, R. (1996). An automatic registration method for frameless stereotaxy, image guided surgery, and enhanced reality visualization. *Medical Imaging, IEEE Transactions on, 15*(2), 129-140.
69. Hajnal, J. V., Saeed, N., Soar, E. J., Oatridge, A., Young, I. R., & Bydder, G. M. (1995). A registration and interpolation procedure for subvoxel matching of serially acquired MR images. *Journal of computer assisted tomography, 19*(2), 289-296.
70. Heimann, T., Van Ginneken, B., Styner, M. A., Arzhaeva, Y., Aurich, V., Bauer, C., . . . Bekes, G. (2009). Comparison and evaluation of methods for liver segmentation from CT datasets. *Medical Imaging, IEEE Transactions on, 28*(8), 1251-1265.
71. Helman, J., & Hesselink, L. (1989). Representation and display of vector field topology in fluid flow data sets. *Computer, 22*(8), 27-36.
72. Helman, J. L., & Hesselink, L. (1991). Visualizing vector field topology in fluid flows. *IEEE Computer Graphics and Applications, 11*(3), 36-46.
73. Herline, A. J., Herring, J. L., Stefansic, J. D., Chapman, W. C., Galloway, R. L., & Dawant, B. M. (2000). Surface registration for use in interactive, image-guided liver surgery. *Computer Aided Surgery, 5*(1), 11-17.
74. Herring, J. L., Dawant, B. M., Maurer Jr, C. R., Muratore, D. M., Galloway, R. L., & Fitzpatrick, J. M. (1998). Surface-based registration of CT images to physical space for image-guided surgery of the spine: a sensitivity study. *Medical Imaging, IEEE Transactions on, 17*(5), 743-752.
75. Hill, D. L., Batchelor, P. G., Holden, M., & Hawkes, D. J. (2001). Medical image registration. *Physics in medicine and biology, 46*(3), R1.
76. Holden, M. (2008). A review of geometric transformations for nonrigid body registration. *Medical Imaging, IEEE Transactions on, 27*(1), 111-128.
77. Holden, M., Hill, D. L., Denton, E. R., Jarosz, J. M., Cox, T. C., Rohlfing, T., . . . Hawkes, D. J. (2000). Voxel similarity measures for 3-D serial MR brain image registration. *Medical Imaging, IEEE Transactions on, 19*(2), 94-102.
78. Holden, M., Schnabel, J. A., & Hill, D. L. (2002). Quantification of small cerebral ventricular volume changes in treated growth hormone patients using nonrigid registration. *Medical Imaging, IEEE Transactions on, 21*(10), 1292-1301.
79. Horn, B. K., & Schunck, B. G. (1981). *Determining optical flow*. Paper presented at the 1981 Technical Symposium East.
80. Hostettler, A., Nicolau, S., Rémond, Y., Marescaux, J., & Soler, L. (2010). A real-time predictive simulation of abdominal viscera positions during quiet free breathing. *Progress in biophysics and molecular biology, 103*(2), 169-184.
81. Hu, K.-Q., Kyulo, N. L., Lim, N., Elhazin, B., Hillebrand, D. J., & Bock, T. (2004). Clinical significance of elevated alpha-fetoprotein (AFP) in patients with chronic hepatitis C, but not hepatocellular carcinoma. *The American journal of gastroenterology, 99*(5), 860-865.
82. Hu, S., Hoffman, E. A., & Reinhardt, J. M. (2001). Automatic lung segmentation for accurate quantitation of volumetric X-ray CT images. *Medical Imaging, IEEE Transactions on, 20*(6), 490-498.
83. Huang, G.-T., Sheu, J.-C., Yang, P.-M., Lee, H.-S., Wang, T.-H., & Chen, D.-S. (1996). Ultrasound-guided cutting biopsy for the diagnosis of hepatocellular carcinoma—a study based on 420 patients. *J Hepatol, 25*(3), 334-338.
84. Huang, W., Quan, L., Lin, Z., Duan, Y., Zhou, J., Yang, Y., & Xiong, W. (2014). *Abdominal wall extraction using constrained deformable model and abdominal context.* Paper presented at the Engineering in Medicine and Biology Society (EMBC), 2014 36th Annual International Conference of the IEEE.

85. Hugo, G., Vargas, C., Liang, J., Kestin, L., Wong, J. W., & Yan, D. (2006). Changes in the respiratory pattern during radiotherapy for cancer in the lung. *Radiother Oncol, 78*(3), 326-331. doi: 10.1016/j.radonc.2006.02.015
86. Hutton, B. F., & Braun, M. (2003). *Software for image registration: algorithms, accuracy, efficacy.* Paper presented at the Seminars in nuclear medicine.
87. Interventional Radiology Services. Retrieved 10 March, 2015, from http://www.midtownimaging.in/Interventional-radiology.html
88. IQQA®-Liver. (2009).
89. ITK. (2003). Retrieved 10 March, 2015, from http://www.itk.org/ITK/help/documentation.html
90. Jenkinson, M., Bannister, P., Brady, M., & Smith, S. (2002). Improved optimization for the robust and accurate linear registration and motion correction of brain images. *Neuroimage, 17*(2), 825-841.
91. Joseph, W. (2010). Proper breathing. from http://waynejoseph.files.wordpress.com/2010/07/proper-breathing-photo.jpg
92. Kabus, S., Klinder, T., Murphy, K., van Ginneken, B., Lorenz, C., & Pluim, J. P. (2009). Evaluation of 4D-CT lung registration *Medical Image Computing and Computer-Assisted Intervention–MICCAI 2009* (pp. 747-754): Springer.
93. Kalender, W. A., Fichte, H., Bautz, W., & Skalej, M. (1991). Semiautomatic evaluation procedures for quantitative CT of the lung. *Journal of computer assisted tomography, 15*(2), 248-255.
94. Kandel, S., Kloeters, C., Meyer, H., Hein, P., Hilbig, A., & Rogalla, P. (2009). Whole-organ perfusion of the pancreas using dynamic volume CT in patients with primary pancreas carcinoma: acquisition technique, post-processing and initial results. *European radiology, 19*(11), 2641-2646.
95. Kang, Y., Engelke, K., & Kalender, W. A. (2003). A new accurate and precise 3-D segmentation method for skeletal structures in volumetric CT data. *Medical Imaging, IEEE Transactions on, 22*(5), 586-598.
96. Kass, M., Witkin, A., & Terzopoulos, D. (1988). Snakes: Active contour models. *International journal of computer vision, 1*(4), 321-331.
97. Kaus, M. R., Brock, K. K., Pekar, V., Dawson, L. A., Nichol, A. M., & Jaffray, D. A. (2007). Assessment of a model-based deformable image registration approach for radiation therapy planning. *International Journal of Radiation Oncology* Biology* Physics, 68*(2), 572-580.
98. Keall, P. J., Mageras, G. S., Balter, J. M., Emery, R. S., Forster, K. M., Jiang, S. B., . . . Yorke, E. (2006). The management of respiratory motion in radiation oncology report of AAPM Task Group 76. *Med Phys, 33*(10), 3874-3900.
99. Kim, D., Kim, H., & Kang, H. S. (2002). *Object-tracking segmentation method: vertebra and rib segmentation in CT images.* Paper presented at the Medical Imaging 2002.
100. Kim, J., & Fessler, J. A. (2004). Intensity-based image registration using robust correlation coefficients. *Medical Imaging, IEEE Transactions on, 23*(11), 1430-1444.
101. Kiraly, A. P., Higgins, W. E., Hoffman, E. A., McLennan, G., & Reinhardt, J. M. (2002). *3D human airway segmentation for virtual bronchoscopy.* Paper presented at the Medical Imaging 2002.
102. Klein, A., Ghosh, S. S., Avants, B., Yeo, B. T., Fischl, B., Ardekani, B., . . . Parsey, R. V. (2010). Evaluation of volume-based and surface-based brain image registration methods. *Neuroimage, 51*(1), 214-220.
103. Klinder, T., Lorenz, C., Von Berg, J., Dries, S. P., Bülow, T., & Ostermann, J. (2007). Automated model-based rib cage segmentation and labeling in CT images *Medical*

Image Computing and Computer-Assisted Intervention–MICCAI 2007 (pp. 195-202): Springer.
104. Korin, H. W., Ehman, R. L., Riederer, S. J., Felmlee, J. P., & Grimm, R. C. (1992). Respiratory kinematics of the upper abdominal organs: a quantitative study. *Magn Reson Med, 23*(1), 172-178.
105. Lange, T., Papenberg, N., Heldmann, S., Modersitzki, J., Fischer, B., Lamecker, H., & Schlag, P. M. (2009). 3D ultrasound-CT registration of the liver using combined landmark-intensity information. *International Journal of Computer Assisted Radiology and Surgery, 4*(1), 79-88.
106. Lange, T., Wenckebach, T., Lamecker, H., Seebaß, M., Hünerbein, M., Eulenstein, S., & Schlag, P.-M. (2005). *Registration of portal and hepatic venous phase of MR/CT data for computer-assisted liver surgery planning.* Paper presented at the International Congress Series.
107. Lee, S., Wolberg, G., Chwa, K.-Y., & Shin, S. Y. (1996). Image metamorphosis with scattered feature constraints. *Visualization and Computer Graphics, IEEE Transactions on, 2*(4), 337-354.
108. Lee, S., Wolberg, G., & Shin, S. Y. (1997). Scattered data interpolation with multilevel B-splines. *Visualization and Computer Graphics, IEEE Transactions on, 3*(3), 228-244.
109. Lee, W.-C. C., Tublin, M. E., & Chapman, B. E. (2005). Registration of MR and CT images of the liver: comparison of voxel similarity and surface based registration algorithms. *Computer methods and programs in biomedicine, 78*(2), 101-114.
110. Lemieux, L., & Barker, G. J. (1998). Measurement of small inter-scan fluctuations in voxel dimensions in magnetic resonance images using registration. *Med Phys, 25*(6), 1049-1054.
111. Lencioni, R., & Crocetti, L. (2008). Image-guided thermal ablation of hepatocellular carcinoma. *Critical reviews in oncology/hematology, 66*(3), 200-207.
112. Leroy, A., Mozer, P., Payan, Y., & Troccaz, J. (2004). Rigid registration of freehand 3D ultrasound and CT-scan kidney images *Medical Image Computing and Computer-Assisted Intervention–MICCAI 2004* (pp. 837-844): Springer.
113. Lester, H., & Arridge, S. R. (1999). A survey of hierarchical non-linear medical image registration. *Pattern recognition, 32*(1), 129-149.
114. Li, B., Christensen, G. E., Hoffman, E. A., McLennan, G., & Reinhardt, J. M. (2003). Establishing a normative atlas of the human lung: intersubject warping and registration of volumetric CT images. *Academic Radiology, 10*(3), 255-265.
115. Li, B., Christensen, G. E., Hoffman, E. A., McLennan, G., & Reinhardt, J. M. (2012). Establishing a Normative Atlas of the Human Lung: Computing the Average Transformation and Atlas Construction. *Academic Radiology, 19*(11), 1368-1381. doi: http://dx.doi.org/10.1016/j.acra.2012.04.025
116. Li, C., Huang, R., Ding, Z., Gatenby, J., Metaxas, D. N., & Gore, J. C. (2011). A level set method for image segmentation in the presence of intensity inhomogeneities with application to MRI. *Image Processing, IEEE Transactions on, 20*(7), 2007-2016.
117. Lie, J., Lysaker, M., & Tai, X.-C. (2006). A binary level set model and some applications to Mumford-Shah image segmentation. *Image Processing, IEEE Transactions on, 15*(5), 1171-1181.
118. Livraghi, T., Solbiati, L., Meloni, M. F., Gazelle, G. S., Halpern, E. F., & Goldberg, S. N. (2003). Treatment of Focal Liver Tumors with Percutaneous Radio-frequency Ablation: Complications Encountered in a Multicenter Study 1. *Radiology, 226*(2), 441-451.

119. Llibre, J., da Silva, P. R., & Teixeira, M. A. (2007). Regularization of Discontinuous Vector Fields on via Singular Perturbation. *Journal of Dynamics and Differential Equations, 19*(2), 309-331.
120. Llovet, J. M., Brú, C., & Bruix, J. (1998). *Prognosis of hepatocellular carcinoma: the BCLC staging classification.* Paper presented at the Semin Liver Dis.
121. Llovet, J. M., Burroughs, A., & Bruix, J. (2003). Hepatocellular carcinoma. *Lancet, 362*(9399), 1907-1917. doi: 10.1016/s0140-6736(03)14964-1
122. Llovet, J. M., Schwartz, M., & Mazzaferro, V. (2005). *Resection and liver transplantation for hepatocellular carcinoma.* Paper presented at the Seminars in Liver Diseases.
123. Low, K.-L. (2004). Linear least-squares optimization for point-to-plane icp surface registration. *Chapel Hill, University of North Carolina*.
124. Maes, F., Collignon, A., Vandermeulen, D., Marchal, G., & Suetens, P. (1997). Multimodality image registration by maximization of mutual information. *Medical Imaging, IEEE Transactions on, 16*(2), 187-198.
125. Maes, F., Vandermeulen, D., & Suetens, P. (1999). Comparative evaluation of multiresolution optimization strategies for multimodality image registration by maximization of mutual information. *Medical image analysis, 3*(4), 373-386.
126. Marieb, E. N., & Hoehn, K. (2007). *Human anatomy & physiology*: Pearson Education.
127. Mattes, D., Haynor, D. R., Vesselle, H., Lewellen, T. K., & Eubank, W. (2003). PET-CT image registration in the chest using free-form deformations. *Medical Imaging, IEEE Transactions on, 22*(1), 120-128.
128. Mattes, D., Haynor, D. R., Vesselle, H., Lewellyn, T. K., & Eubank, W. (2001). *Nonrigid multimodality image registration.* Paper presented at the Medical Imaging 2001.
129. Maurer Jr, C. R., Fitzpatrick, J. M., Wang, M. Y., Galloway, R. L., Maciunas, R. J., & Allen, G. S. (1997). Registration of head volume images using implantable fiducial markers. *Medical Imaging, IEEE Transactions on, 16*(4), 447-462.
130. Maurer Jr, C. R., Maciunas, R. J., & Fitzpatrick, J. M. (1998). Registration of head CT images to physical space using a weighted combination of points and surfaces [image-guided surgery]. *Medical Imaging, IEEE Transactions on, 17*(5), 753-761.
131. Mauri, G., De Beni, S., Forzoni, L., D'Onofrio, S., Kolev, V., Lagana, M., & Solbiati, L. (2014). *Virtual navigator automatic registration technology in abdominal application.* Paper presented at the Engineering in Medicine and Biology Society (EMBC), 2014 36th Annual International Conference of the IEEE.
132. McClelland, J., Hughes, S., Modat, M., Qureshi, A., Ahmad, S., Landau, D., . . . Hawkes, D. (2011). Inter-fraction variations in respiratory motion models. *Physics in medicine and biology, 56*(1), 251.
133. McLeish, K., Hill, D. L., Atkinson, D., Blackall, J. M., & Razavi, R. (2002). A study of the motion and deformation of the heart due to respiration. *Medical Imaging, IEEE Transactions on, 21*(9), 1142-1150.
134. Meijering, E. (2002). A chronology of interpolation: from ancient astronomy to modern signal and image processing. *Proceedings of the IEEE, 90*(3), 319-342.
135. Miller, M., Banerjee, A., Christensen, G., Joshi, S., Khaneja, N., Grenander, U., & Matejic, L. (1997). Statistical methods in computational anatomy. *Statistical methods in medical research, 6*(3), 267-299.
136. Miller, M. I., Beg, M. F., Ceritoglu, C., & Stark, C. (2005). Increasing the power of functional maps of the medial temporal lobe by using large deformation diffeomorphic

metric mapping. *Proceedings of the National Academy of Sciences of the United States of America, 102*(27), 9685-9690.
137. Mortensen, E., Morse, B., Barrett, W., & Udupa, J. (1992, 11-14 Oct 1992). *Adaptive boundary detection using `live-wire' two-dimensional dynamic programming.* Paper presented at the Computers in Cardiology 1992, Proceedings of.
138. Murphy, K., Van Ginneken, B., Reinhardt, J. M., Kabus, S., Ding, K., Deng, X., . . . Garcia, V. (2011). Evaluation of registration methods on thoracic CT: the EMPIRE10 challenge. *Medical Imaging, IEEE Transactions on, 30*(11), 1901-1920.
139. Murphy, M. J., Adler, J. R., Bodduluri, M., Dooley, J., Forster, K., Hai, J., . . . Poen, J. (2000). Image-guided radiosurgery for the spine and pancreas. *Computer Aided Surgery, 5*(4), 278-288.
140. Myrian®. (2006).
141. NEXAVAR. (2008). Barcelona Clinic Liver Cancer (BCLC) Staging and Treatment Strategy includes Nexavar for advanced HCC. from http://www.nexavar-us.com/scripts/pages/en/health-care-provider/hcc/treatment-plan/how-nexavar-fits-in/bclc-guidelines/
142. Nicolau, S., Garcia, A., Pennec, X., Soler, L., & Ayache, N. (2005). An augmented reality system to guide radio-frequency tumour ablation. *Computer animation and virtual worlds, 16*(1), 1-10.
143. Nicolau, S., Pennec, X., Soler, L., Buy, X., Gangi, A., Ayache, N., & Marescaux, J. (2009). An augmented reality system for liver thermal ablation: Design and evaluation on clinical cases. *Medical image analysis, 13*(3), 494-506.
144. Nishiyama, K. K., Pauchard, Y., Nikkel, L. E., Iyer, S., Zhang, C., McMahon, D. J., . . . Nickolas, T. L. (2014). Longitudinal HR-pQCT and Image Registration Detects Endocortical Bone Loss in Kidney Transplantation Patients. *Journal of Bone and Mineral Research*.
145. Oguro, S., Tuncali, K., Elhawary, H., Morrison, P. R., Hata, N., & Silverman, S. G. (2011). Image registration of pre-procedural MRI and intra-procedural CT images to aid CT-guided percutaneous cryoablation of renal tumors. *International Journal of Computer Assisted Radiology and Surgery, 6*(1), 111-117.
146. Okumura, T., Yamamoto, S., Matsumoto, M., Takeno, Y., Iinuma, T., & Matsumoto, T. (1998). The lung region extraction in the chest CT images by the active cylinder model.
147. Oliver 3rd, J., Baron, R., Federle, M., & Rockette Jr, H. (1996). Detecting hepatocellular carcinoma: value of unenhanced or arterial phase CT imaging or both used in conjunction with conventional portal venous phase contrast-enhanced CT imaging. *AJR. American journal of roentgenology, 167*(1), 71-77.
148. Ourselin, S., Roche, A., Prima, S., & Ayache, N. (2000). *Block matching: A general framework to improve robustness of rigid registration of medical images.* Paper presented at the Medical Image Computing and Computer-Assisted Intervention–MICCAI 2000.
149. Pace, D., Aylward, S., & Niethammer, M. (2013). A locally adaptive regularization based on anisotropic diffusion for deformable image registration of sliding organs.
150. Pace, D. F., Enquobahrie, A., Yang, H., Aylward, S. R., & Niethammer, M. (2011). *Deformable image registration of sliding organs using anisotropic diffusive regularization.* Paper presented at the Biomedical Imaging: From Nano to Macro, 2011 IEEE International Symposium on.
151. Pace, D. F., Niethammer, M., & Aylward, S. R. (2012). Sliding geometries in deformable image registration *Abdominal Imaging. Computational and Clinical Applications* (pp. 141-148): Springer.

152. Paragios, N., & Deriche, R. (2000). Coupled geodesic active regions for image segmentation: A level set approach *Computer Vision—ECCV 2000* (pp. 224-240): Springer.
153. Park, J. W. (2005). [Hepatocellular carcinoma in Korea: introduction and overview]. *The Korean journal of gastroenterology= Taehan Sohwagi Hakhoe chi, 45*(4), 217-226.
154. Pavlovich, C. P., Walther, M. M., Choyke, P. L., Pautler, S. E., Chang, R., Linehan, W. M., & Wood, B. J. (2002). Percutaneous radio frequency ablation of small renal tumors: initial results. *The Journal of urology, 167*(1), 10-15.
155. Pelizzari, C. A., Chen, G. T., Spelbring, D. R., Weichselbaum, R. R., & Chen, C.-T. (1989). Accurate three-dimensional registration of CT, PET, and/or MR images of the brain. *Journal of computer assisted tomography, 13*(1), 20-26.
156. Pennec, X., Cachier, P., & Ayache, N. (1999). *Understanding the "demon's algorithm": 3D non-rigid registration by gradient descent.* Paper presented at the Medical Image Computing and Computer-Assisted Intervention–MICCAI'99.
157. Peterhans, M., vom Berg, A., Dagon, B., Inderbitzin, D., Baur, C., Candinas, D., & Weber, S. (2011). A navigation system for open liver surgery: design, workflow and first clinical applications. *The International Journal of Medical Robotics and Computer Assisted Surgery, 7*(1), 7-16.
158. Picture of the Kidneys. (2014). Retrieved March 2015, 2015, from http://www.webmd.com/urinary-incontinence-oab/picture-of-the-kidneys
159. Pietrzyk, U., Herholz, K., Schuster, A., Stockhausen, H.-M. v., Lucht, H., & Heiss, W.-D. (1996). Clinical applications of registration and fusion of multimodality brain images from PET, SPECT, CT, and MRI. *European journal of radiology, 21*(3), 174-182.
160. Pluim, J. P., Maintz, J. A., & Viergever, M. A. (2003). Mutual-information-based registration of medical images: a survey. *Medical Imaging, IEEE Transactions on, 22*(8), 986-1004.
161. Pomerleau, F., Colas, F., Siegwart, R., & Magnenat, S. (2013). Comparing ICP variants on real-world data sets. *Autonomous Robots, 34*(3), 133-148.
162. Powell, M. J. D. (1981). *Approximation theory and methods*: Cambridge university press.
163. Radiofrequency Ablation (RFA). (2010). from http://www.hopkinsmedicine.org/liver_tumor_center/treatments/ablative_techniques/radio_frequency_ablation.html
164. Ramakrishnan, S., Alvino, C., Grady, L., & Kiraly, A. (2011). *Automatic three-dimensional rib centerline extraction from CT scans for enhanced visualization and anatomical context.* Paper presented at the SPIE Medical Imaging.
165. Raya, S. P., & Udupa, J. K. (1990). Shape-based interpolation of multidimensional objects. *Medical Imaging, IEEE Transactions on, 9*(1), 32-42.
166. REAL HUMAN PANCREAS. Retrieved 10 March, 2015, from http://www.patient.co.uk/health/Cancer-of-the-Pancreas.htm
167. Reitinger, B., Bornik, A., Beichel, R., & Schmalstieg, D. (2006). Liver surgery planning using virtual reality. *IEEE Computer Graphics and Applications*(6), 36-47.
168. Respiratory System. Retrieved 5 March, 2015, from http://www.austincc.edu/apreview/PhysText/Respiratory.html
169. Rietzel, E., & Chen, G. T. (2006). Deformable registration of 4D computed tomography data. *Med Phys, 33*(11), 4423-4430.
170. Rogers, D. F. (2000). *An introduction to NURBS: with historical perspective*: Elsevier.

171. Rohlfing, T., Maurer, C. R., Jr., O'Dell, W. G., & Zhong, J. (2004). Modeling liver motion and deformation during the respiratory cycle using intensity-based nonrigid registration of gated MR images. *Med Phys, 31*(3), 427-432.
172. Rohlfing, T., Maurer Jr, C. R., O'Dell, W. G., & Zhong, J. (2004). Modeling liver motion and deformation during the respiratory cycle using intensity-based nonrigid registration of gated MR images. *Med Phys, 31*(3), 427-432.
173. Ruan, D., Esedoglu, S., & Fessler, J. A. (2009). *Discriminative sliding preserving regularization in medical image registration.* Paper presented at the Biomedical Imaging: From Nano to Macro, 2009. ISBI'09. IEEE International Symposium on.
174. Ruan, D., Fessler, J. A., & Esedoglu, S. (2008). *Discontinuity preserving regularization for modeling sliding in medical image registration.* Paper presented at the Nuclear Science Symposium Conference Record, 2008. NSS'08. IEEE.
175. Rueckert, D., Aljabar, P., Heckemann, R. A., Hajnal, J. V., & Hammers, A. (2006). Diffeomorphic registration using B-splines *Medical Image Computing and Computer-Assisted Intervention–MICCAI 2006* (pp. 702-709): Springer.
176. Rueckert, D., Frangi, A. F., & Schnabel, J. A. (2003). Automatic construction of 3-D statistical deformation models of the brain using nonrigid registration. *Medical Imaging, IEEE Transactions on, 22*(8), 1014-1025.
177. Rueckert, D., Sonoda, L. I., Hayes, C., Hill, D. L., Leach, M. O., & Hawkes, D. J. (1999). Nonrigid registration using free-form deformations: application to breast MR images. *Medical Imaging, IEEE Transactions on, 18*(8), 712-721.
178. Rusinkiewicz, S., & Levoy, M. (2001). *Efficient variants of the ICP algorithm.* Paper presented at the 3-D Digital Imaging and Modeling, 2001. Proceedings. Third International Conference on.
179. Sadek, A. G., Mitchell, D. G., Siegelman, E. S., Outwater, E. K., Matteucci, T., & Hann, H. (1995). Early hepatocellular carcinoma that develops within macroregenerative nodules: growth rate depicted at serial MR imaging. *Radiology, 195*(3), 753-756.
180. Sakai, T., Sugiyama, M., Kitagawa, K., & Suzuki, K. (2015). Registration of infrared transmission images using squared-loss mutual information. *Precision Engineering, 39*, 187-193.
181. Salvi, J., Matabosch, C., Fofi, D., & Forest, J. (2007). A review of recent range image registration methods with accuracy evaluation. *Image and Vision Computing, 25*(5), 578-596.
182. Schad, L. R., Boesecke, R., Schlegel, W., Hartmann, G. H., Sturm, V., Strauss, L. G., & Lorenz, W. J. (1987). Three dimensional image correlation of CT, MR, and PET studies in radiotherapy treatment planning of brain tumors. *Journal of computer assisted tomography, 11*(6), 948-954.
183. Schenk, A., Prause, G., & Peitgen, H.-O. (2000). *Efficient semiautomatic segmentation of 3D objects in medical images.* Paper presented at the Medical Image Computing and Computer-Assisted Intervention–MICCAI 2000.
184. Schmidt-Richberg, A., Ehrhardt, J., Werner, R., & Handels, H. (2009). Slipping objects in image registration: improved motion field estimation with direction-dependent regularization. *Med Image Comput Comput Assist Interv, 12*(Pt 1), 755-762.
185. Schmidt-Richberg, A., Ehrhardt, J., Werner, R., & Handels, H. (2012a). Fast explicit diffusion for registration with direction-dependent regularization *Biomedical Image Registration* (pp. 220-228): Springer.

186. Schmidt-Richberg, A., Werner, R., Handels, H., & Ehrhardt, J. (2012b). Estimation of slipping organ motion by registration with direction-dependent regularization. *Medical image analysis, 16*(1), 150-159.
187. Schnabel, J. A., Tanner, C., Smith, A. D. C., Hill, D. L., Hawkes, D. J., Leach, M. O., . . . Hose, R. (2001). *Validation of non-rigid registration using finite element methods.* Paper presented at the Information Processing in Medical Imaging.
188. Schroeder, W., Ng, L., & Cates, J. (2003). The itk software guide.
189. Schumaker, L. L. (1981). *Spline functions: basic theory*: Cambridge University Press.
190. Segars, W. P., Lalush, D. S., & Tsui, B. M. W. (2001). Modeling respiratory mechanics in the MCAT and spline-based MCAT phantoms. *IEEE Transactions on Nuclear Science, 48*(1), 89-97. doi: 10.1109/23.910837
191. Segars, W. P., Sturgeon, G., Mendonca, S., Grimes, J., & Tsui, B. M. W. (2010). 4D XCAT phantom for multimodality imaging research. *Med Phys, 37*(9). doi: 10.1118/1.3480985
192. Seppenwoolde, Y., Shirato, H., Kitamura, K., Shimizu, S., van Herk, M., Lebesque, J. V., & Miyasaka, K. (2002). Precise and real-time measurement of 3D tumor motion in lung due to breathing and heartbeat, measured during radiotherapy. *Int J Radiat Oncol Biol Phys, 53*(4), 822-834.
193. Sethian, J. A. (1999). *Level set methods and fast marching methods: evolving interfaces in computational geometry, fluid mechanics, computer vision, and materials science* (Vol. 3): Cambridge university press.
194. Shannon, C. E. (2001). A mathematical theory of communication. *ACM SIGMOBILE Mobile Computing and Communications Review, 5*(1), 3-55.
195. Shen, H., Liang, L., Shao, M., & Qing, S. (2004). Tracing based segmentation for the labeling of individual rib structures in chest CT volume data *Medical Image Computing and Computer-Assisted Intervention–MICCAI 2004* (pp. 967-974): Springer.
196. Sherman, M. (2005). Hepatocellular carcinoma: epidemiology, risk factors, and screening. *Semin Liver Dis, 25*(2), 143-154. doi: 10.1055/s-2005-871194
197. Sherman, M., Peltekian, K. M., & Lee, C. (1995). Screening for hepatocellular carcinoma in chronic carriers of hepatitis B virus: incidence and prevalence of hepatocellular carcinoma in a North American urban population. *Hepatology, 22*(2), 432-438.
198. Shimizu, A., Ohno, R., Ikegami, T., Kobatake, H., Nawano, S., & Smutek, D. (2007). Segmentation of multiple organs in non-contrast 3D abdominal CT images. *International Journal of Computer Assisted Radiology and Surgery, 2*(3-4), 135-142.
199. Shimizu, S., Shirato, H., Xo, B., Kagei, K., Nishioka, T., Hashimoto, S., . . . Miyasaka, K. (1999). Three-dimensional movement of a liver tumor detected by high-speed magnetic resonance imaging. *Radiother Oncol, 50*(3), 367-370.
200. Sotiras, A., Davatzikos, C., & Paragios, N. (2013). Deformable medical image registration: A survey. *Medical Imaging, IEEE Transactions on, 32*(7), 1153-1190.
201. Spiegel, M., Hahn, D. A., Daum, V., Wasza, J., & Hornegger, J. (2009). Segmentation of kidneys using a new active shape model generation technique based on non-rigid image registration. *Computerized Medical Imaging and Graphics, 33*(1), 29-39.
202. Staal, J., van Ginneken, B., & Viergever, M. A. (2007). Automatic rib segmentation and labeling in computed tomography scans using a general framework for detection, recognition and segmentation of objects in volumetric data. *Medical image analysis, 11*(1), 35-46.
203. Strother, S. C., Anderson, J. R., Xu, X.-L., Liow, J.-S., Bonar, D. C., & Rottenberg, D. A. (1994). Quantitative comparisons of image registration techniques based on high-

resolution MRI of the brain. *Journal of computer assisted tomography, 18*(6), 954-962.
204. Subsol, G., Thirion, J.-P., & Ayache, N. (1998). A scheme for automatically building three-dimensional morphometric anatomical atlases: application to a skull atlas. *Medical image analysis, 2*(1), 37-60.
205. Sundarakumar, D. K., Wilson, G. J., Osman, S. F., Zaidi, S. F., & Maki, J. H. (2015). Evaluation of Image Registration in Subtracted 3D Dynamic Contrast-Enhanced MRI of Treated Hepatocellular Carcinoma. *American Journal of Roentgenology, 204*(2), 287-296.
206. Suramo, I., Paivansalo, M., & Myllyla, V. (1984). Cranio-caudal movements of the liver, pancreas and kidneys in respiration. *Acta Radiol Diagn (Stockh), 25*(2), 129-131.
207. Tangkijvanich, P., Anukulkarnkusol, N., Suwangool, P., Lertmaharit, S., Hanvivatvong, O., Kullavanijaya, P., & Poovorawan, Y. (2000). Clinical characteristics and prognosis of hepatocellular carcinoma: analysis based on serum alpha-fetoprotein levels. *Journal of clinical gastroenterology, 31*(4), 302-308.
208. Tanner, C., Schnabel, J. A., Degenhard, A., Castellano-Smith, A. D., Hayes, C., Leach, M. O., . . . Hawkes, D. J. (2002). Validation of volume-preserving non-rigid registration: Application to contrast-enhanced MR-mammography *Medical Image Computing and Computer-Assisted Intervention—MICCAI 2002* (pp. 307-314): Springer.
209. Thirion, J.-P. (1998). Image matching as a diffusion process: an analogy with Maxwell's demons. *Medical image analysis, 2*(3), 243-260.
210. Tittgemeyer, M., Wollny, G., & Kruggel, F. (2002). Visualising deformation fields computed by non-linear image registration. *Computing and Visualization in Science, 5*(1), 45-51.
211. Udupa, J. K., Samarasekera, S., & Barrett, W. A. (1992). *Boundary detection via dynamic programming.* Paper presented at the Visualization in Biomedical Computing.
212. Vandemeulebroucke, J., Bernard, O., Rit, S., Kybic, J., Clarysse, P., & Sarrut, D. (2012). Automated segmentation of a motion mask to preserve sliding motion in deformable registration of thoracic CT. *Med Phys, 39*(2), 1006-1015. doi: 10.1118/1.3679009
213. Vauthey, J.-N., Lauwers, G. Y., Esnaola, N. F., Do, K.-A., Belghiti, J., Mirza, N., . . . Rashid, A. (2002). Simplified staging for hepatocellular carcinoma. *Journal of clinical oncology, 20*(6), 1527-1536.
214. Vese, L. A., & Chan, T. F. (2002). A multiphase level set framework for image segmentation using the Mumford and Shah model. *International journal of computer vision, 50*(3), 271-293.
215. Vijayan, S., Klein, S., Hofstad, E. F., Lindseth, F., Ystgaard, B., & Langø, T. (2014). Motion tracking in the liver: Validation of a method based on 4D ultrasound using a nonrigid registration technique. *Med Phys, 41*(8), 082903.
216. Viola, P., & Wells III, W. M. (1997). Alignment by maximization of mutual information. *International journal of computer vision, 24*(2), 137-154.
217. Von Siebenthal, M., Székely, G., Gamper, U., Boesiger, P., Lomax, A., & Cattin, P. (2007). 4D MR imaging of respiratory organ motion and its variability. *Physics in medicine and biology, 52*(6), 1547.
218. VRMED. (2005). 2014, from http://www.ircad.fr/research/computer/
219. Wang, Y., & Staib, L. H. (1998). Elastic model based non-rigid registration incorporating statistical shape information *Medical Image Computing and Computer-Assisted Interventation—MICCAI'98* (pp. 1162-1173): Springer.

220. Warfield, S. K., Talos, F., Tei, A., Bharatha, A., Nabavi, A., Ferrant, M., . . . Kikinis, R. (2002). Real-time registration of volumetric brain MRI by biomechanical simulation of deformation during image guided neurosurgery. *Computing and Visualization in Science, 5*(1), 3-11.
221. Wein, W., Brunke, S., Khamene, A., Callstrom, M. R., & Navab, N. (2008). Automatic CT-ultrasound registration for diagnostic imaging and image-guided intervention. *Medical image analysis, 12*(5), 577-585.
222. West, J., Fitzpatrick, J. M., Wang, M. Y., Dawant, B. M., Maurer, C. R., Jr., Kessler, R. M., . . . et al. (1997). Comparison and evaluation of retrospective intermodality brain image registration techniques. *J Comput Assist Tomogr, 21*(4), 554-566.
223. West, J., Fitzpatrick, J. M., Wang, M. Y., Dawant, B. M., Maurer Jr, C. R., Kessler, R. M., . . . Collignon, A. (1997). Comparison and evaluation of retrospective intermodality brain image registration techniques. *Journal of computer assisted tomography, 21*(4), 554-568.
224. WIKI. Abdominal cavity. Retrieved 1 March, 2015, from http://en.wikipedia.org/wiki/Abdominal_cavity
225. Williams, D. J., & Shah, M. (1992). A fast algorithm for active contours and curvature estimation. *CVGIP: Image understanding, 55*(1), 14-26.
226. Wimmer, A., Soza, G., & Hornegger, J. (2007). Two-stage semi-automatic organ segmentation framework using radial basis functions and level sets. *3D Segmentation in The Clinic: A Grand Challenge*, 179-188.
227. Wolthaus, J. W., Sonke, J. J., van Herk, M., & Damen, E. M. (2008). Reconstruction of a time-averaged midposition CT scan for radiotherapy planning of lung cancer patients using deformable registration. *Med Phys, 35*(9), 3998-4011.
228. Wong, L. L., Limm, W. M., Severino, R., & Wong, L. M. (2000). Improved survival with screening for hepatocellular carcinoma. *Liver transplantation, 6*(3), 320-325.
229. Wu, M.-T., Chang, J.-M., Chiang, A. A., Lu, J.-Y., Hsu, H.-K., Hsu, W.-H., & Yang, C.-F. (1994). Use of quantitative CT to predict postoperative lung function in patients with lung cancer. *Radiology, 191*(1), 257-262.
230. Wu, Z., Rietzel, E., Boldea, V., Sarrut, D., & Sharp, G. C. (2008). Evaluation of deformable registration of patient lung 4DCT with subanatomical region segmentations. *Med Phys, 35*(2), 775-781.
231. Xie, Y., Chao, M., & Xing, L. (2009). Tissue feature-based and segmented deformable image registration for improved modeling of shear movement of lungs. *International Journal of Radiation Oncology* Biology* Physics, 74*(4), 1256-1265.
232. Xie, Y., Chao, M., & Xiong, G. (2011). Deformable image registration of liver with consideration of lung sliding motion. *Med Phys, 38*(10), 5351-5361. doi: 10.1118/1.3633902
233. Xu, Z., Allen, W. M., Baucom, R. B., Poulose, B. K., & Landman, B. A. (2013). Texture analysis improves level set segmentation of the anterior abdominal wall. *Med Phys, 40*(12), 121901. doi: 10.1118/1.4828791
234. Yang, G., Gu, J., Chen, Y., Liu, W., Tang, L., Shu, H., & Toumoulin, C. (2014). *Automatic kidney segmentation in CT images based on multi-atlas image registration.* Paper presented at the Engineering in Medicine and Biology Society (EMBC), 2014 36th Annual International Conference of the IEEE.
235. Yao, J., Burns, J. E., & Summers, R. M. (2012). *Sclerotic rib metastases detection on routine CT images.* Paper presented at the Biomedical Imaging (ISBI), 2012 9th IEEE International Symposium on.

236. Yao, J., O'Connor, S. D., & Summers, R. M. (2006). *Automated spinal column extraction and partitioning.* Paper presented at the Biomedical Imaging: Nano to Macro, 2006. 3rd IEEE International Symposium on.
237. Yu, H. (2005). *Automatic rigid and deformable medical image registration.* Worcester Polytechnic Institute.
238. Yushkevich, P. A., Piven, J., Hazlett, H. C., Smith, R. G., Ho, S., Gee, J. C., & Gerig, G. (2006). User-guided 3D active contour segmentation of anatomical structures: significantly improved efficiency and reliability. *Neuroimage, 31*(3), 1116-1128.
239. Zhang, L., Li, X., & Hu, Q. (2012). *Automatic rib segmentation in chest ct volume data.* Paper presented at the Biomedical Engineering and Biotechnology (iCBEB), 2012 International Conference on.
240. Zhang, Z. (1994). Iterative point matching for registration of free-form curves and surfaces. *International journal of computer vision, 13*(2), 119-152.
241. Zhao, W., Young, T. Y., & Ginsberg, M. (1993). Registration and three-dimensional reconstruction of autoradiographic images by the disparity analysis method. *Medical Imaging, IEEE Transactions on, 12*(4), 782-791.
242. Zhu, W., Nicolau, S., Soler, L., Hostettler, A., Marescaux, J., & Rémond, Y. (2012). Fast segmentation of abdominal wall: Application to sliding effect removal for non-rigid registration *Abdominal Imaging. Computational and Clinical Applications* (pp. 198-207): Springer.
243. Zöllner, F. G., Sance, R., Rogelj, P., Ledesma-Carbayo, M. J., Rørvik, J., Santos, A., & Lundervold, A. (2009). Assessment of 3D DCE-MRI of the kidneys using non-rigid image registration and segmentation of voxel time courses. *Computerized Medical Imaging and Graphics, 33*(3), 171-181.

Publications

Evaluation of abdominal wall & diaphragm removal for accurate non-rigid registration of multi-phase clinical image.Wenwu Zhu, Stephane Nicolau, Alexandre Hostettler, Jacques Marescaux, Yves Rémond, Luc Soler.2015 .Submitted to Medical Physics (under review)

Methodology for Fast Interactive Segmentation of Peritoneum and Diaphragm in Multi-Modal 3D Medical Image, Journal of computer surgery. A. Hostettler, W. Zhu, S.A. Nicolau, L. Soler, J. Marescaux. 2015. Submitted to the Journal of Computational Surgery (under review)

A new approach for sliding effect removal in abdominal image registration . W.Zhu, S. Nicolau, L.Soler, A.Hostettler, J.Marescaux, Y.Rémond. Int.J CARS (2013) Volume 8: 169-170

Fast Segmentation of Abdominal Wall: Application to Sliding Effect Removal for Non-rigid Registration. Zhu, W., Nicolau, S., Soler, L., Hostettler, A., Marescaux, J., & Rémond, Y. (2012). Workshop on Computational and Clinical Applications in Abdominal Imaging. Lecture Notes in Computer Science Volume 7601, pp 198-207, 2012.

Oral presentation in International conference

1. Fast Segmentation of Abdominal Wall: Application to Sliding Effect Removal for Non Rigid Registration. The 15th International Conference on Medical Image Computing and Computer Assisted Intervention (MICCAI 2012) workshop on Computational and Clinical Applications in Abdominal Imaging. Nice, France; October1-5, 2012.
2. A new approach for sliding effect removal in the multi-modal non-rigid abdominal image registration. Computer Assisted Radiology and Surgery 27th International Congress and Exhibition (CARS 2013). Heidelberg, Germany; June 26-29, 2013.
3. Fast Interactive Segmentation of Peritoneum and Diaphragm for Better Data Visualization and Registration. The 5th Annual International Conference in Computational Surgery and Dual Training; National Institute of Health (NIH) campus, Washington DC, USA; January19-21, 2015

Wenwu ZHU

Segmentation et recalage d'images TDM multi-phases de l'abdomen pour la planification chirurgicale

Résumé

La fusion d'images TDM de phase artérielles et veineuses est cruciale afin d'assurer une meilleure planification chirurgicale. Cependant, le recalage non-rigide d'images abdominales est encore un challenge à cause de la respiration qui fait glisser les viscères abdominaux le long de la paroi abdominale, créant ainsi un champ de déformation discontinu. L'objectif de cette thèse est de fournir un outil de recalage précis pour les images TDM multi-phases de l'abdomen.

Comme la zone de glissement dans l'abdomen est difficile à segmenter, nous avons d'abord implémenté deux outils de segmentation interactifs permettant une délinéation en 10 minutes de la paroi abdominale et du diaphragme. Pour intégrer ces zones de glissement comme a priori, nous réalisons le recalage sur de nouvelles images dans lesquelles la paroi abdominale et les viscères thoraciques ont été enlevés. Les évaluations sur des données de patient ont montré que notre approche fournit une précision d'environ 1 mm.

Mots-clés: recalage non-rigide, organes abdominaux, paroi abdominale, respiration, segmentation rapide, glissement inter-organe.

Résumé en anglais

The fusion of arterial and venous phase CT images of the entire abdominal viscera is critical for a better diagnosis, surgical planning and treatment, since these two phase images contain complementary information. However, non-rigid registration of abdominal images is still a big challenge due to the breathing motion, which causes sliding motion between the abdominal viscera and the abdo-thoracic wall. The purpose of this thesis is to provide an accurate registration method for abdominal viscera between venous and arterial phase CT images.

In order to remove the sliding motion effect, we decide to separate the image into big motion and less motion regions, and perform the registration on new images where abdo-thoracic wall and thoracic viscera are removed. The segmentation of these sliding interfaces is completed with our fast interactive tools within 10 minitues. Two state-of-the-art non-rigid registration algorithms are then applied on these new images and compared to registration obtained with original images. The evaluation using four abdominal organs (liver, kidney, spleen) and several vessel bifurcations shows that our approach provides a much higher accuracy within 1 mm.

Keywords: sliding motion, abdominal organs, abdominal thoracic wall, non-rigid image registration, fast segmentation.